$Li_{15}Si_4$ Formation in Thin Film Si Negative Electrodes for Li-ion Batteries

by

Douglas Iaboni

Submitted in partial fulfilment of the requirements
for the degree of Master of Science

at

Dalhousie University
Halifax, Nova Scotia
August 2015

Table of Contents

List of Tables

List of Figures

viii

Abstract

In this work, a better understanding behind, and the implications of $Li_{15}Si_4$ formation in Si containing negative electrodes for rechargeable Li-ion batteries during electrochemical cycling was sought. Si in the form of thin films, powder, nanoparticles, recovered film flakes, and films deposited onto compliant layers were fabricated and studied as negative electrodes in Li half-cells. Through a study of the electrochemical behaviour of Si thin films, a model for $Li_{15}Si_4$ formation was proposed. The model hypothesizes that Si under high stress loadings does not form $Li_{15}Si_4$ due to shifting in the voltage curve caused by stress-potential coupling. Later in the study, the formation of $Li_{15}Si_4$ was confirmed to have harmful effects on electrochemical cycling. Overall, the formation of $Li_{15}Si_4$ in Si-based negative electrodes during electrochemical cycling was shown to have potential as an indicator for poorly attached silicon in an alloy or composite coating.

A second study in this work investigated the effect of the binder in electrode coatings on electrochemical performance for rechargeable Li-ion batteries. In this work, coatings using polyimide binder were found to exhibit the most $Li_{15}Si_4$ suppression and least capacity fade during electrochemical cycling. Additionally, composite coatings incorporating polyimide or lithium polyacrylate binder were found to be capable of maintaining electrical contact to poorly attached silicon during extensive cycling, while coatings using polyvinylidene difluoride binder showed capacity fade and an inability to maintain electrical contact to poorly attached Si.

Lastly, the use of compliant conducting layers between the substrate and sputtered Si film in negative electrodes for Li-ion batteries was investigated. This investigation sought to attain similar electrochemical behaviour in Si films to that shown in Si powder based composite coatings when incorporated into Li half-cells. Ultimately, the use of a compliant layer was shown to allow Si films and a binary Si-Fe thin film to exhibit significantly more similar electrochemical behaviour to Si powder containing composite coatings than films deposited directly onto a metallic substrate.

List of Abbreviations Used

AM   active material

a-Si   amorphous silicon

BSE   backscattered electrons

by wt.   by weight

CL   compliant layer

FeSi(CL)   compliant layer with an $Fe_{26}Si_{74}$ film sputtered onto it

Si(CL)   compliant layer with a Si film sputtered onto it

CR-Cu   cold-rolled copper foil

CR-Cu^R roughened cold-rolled copper foil

c-Si   crystalline silicon

DEC   diethyl carbonate

e   charge of an electron (1.602×10^{-19} coulombs)

E   energy

EC   ethlylene carbonate

E-Cu   electrolytic copper foil

E-Cu^R roughened electrolytic copper foil

EDS   energy dispersive X-ray detector spectrometry

ex-situ XRD   subjecting electrode material to XRD while it is not actively cycling

FEC	fluoroethylene carbonate
FIB	focused ion beam
in-situ XRD	subjecting electrode material to XRD while it is cycling
Irrev.	irreversible
LiPAA	lithium polyacrylate
MW	molecular weight
n	number of electrons
Ni^R	roughened nickel foil
NMP	N-methyl-2-pyrrolidone
n-Si	silicon nanoparticles
PAA	polyacrylic acid
PE	polyethylene
PP	polypropylene
pro.	procedure
Q	charge (in coulombs)
q_R	volumetric capacity (Ah/L)
Rev.	reversible
rpm	revolutions per minute
SA	surface area

SC	Super C (carbon black)
SE	secondary electrons
SEI	solid electrolyte interphase
SEM	scanning electron microscopy
SS	stainless steel
T_B	binder thickness on active material and carbon black
U_R	energy density
XRD	X-ray diffraction
ρ	density
μ	chemical potential

Acknowledgements

First of all, I would like to thank the Dalhousie Department of Chemistry for taking care of me for all these years. It was a wonderful environment to work and learn in. Everyone has been very supportive and helpful.

I would also like to thank all the members of the Obrovac lab (past and previous) for all their help and fun we have had over the years! Best of luck to you all. Specifically, I'd like to thank Tim Hatchard for training me on almost everything multiple times, and for all our discussions about various things. Big thanks to Jeff Dahn for giving me access to his laboratory equipment and time, also for helping me rummage through his huge inventory.

I would like to sincerely thank my committee for providing guidance, and positive feedback to me during my studies. I would also like to thank them for attending my committee meeting, seminar, and reading my thesis. It really works out to take up some time. I would like to specifically thank Mary Anne White for being part of my committee, twice, when my work was a bit outside of her research area.

Thanks to my family for giving me some space over the past year, I know that I don't visit everyone enough these days, but hopefully that will all change soon! I would like to thank NSERC, Dalhousie, and 3M for their gracious funding toward my project.

Last, but certainly not least, I have to give a huge thank you to Mark Obrovac for being a superb supervisor and friend. He really puts the time and effort into his work, and all of his students (including me) know and appreciate that. It has really been my pleasure to be a part of your lab over the past 4 years.

Chapter 1 Introduction

Rechargeable Li-ion batteries have come a long way since discovering that lithium could reversibly intercalate into the transition-metal dichalcogenides.[1] Before researchers realized the substantial safety advantages associated with Li-ion batteries, manufacturers used Li metal as a negative electrode because of its high gravimetric and volumetric energy density.[2,3] The first launch of Li batteries, the Molicel, incorporated this idea with an MoS_2 positive electrode that resulted in a large-scale recall of the technology due to battery fires.[4] This resulted in the eventual introduction of Li-ion battery technology, in which the metallic Li electrode was replaced with graphite. Ever since then, numerous materials have been explored in the hopes of acquiring higher energy density, lower cost, and safer rechargeable Li-ion battery technology.[5–7] Today, because of their high energy density and power output, rechargeable Li-ion batteries monopolize the growing portable electronics industry.

The annual growth rate of Li-ion energy density between 1990 and 2010 has been 5.5 Wh/kg per annum; considering the current energy density of Li-ion batteries is 240 Wh/kg, goals set by the New Energy and Industrial Technology Development Organization (obtaining 500 Wh/kg by 2030) seem unlikely to be realized.[8,9] Therefore, in order to make Li-ion more practical in applications requiring more energy, their material make-up needs to be optimized once more. Alloy negative electrodes offer an opportunity for significant increases in energy density.[7] Specifically, the volumetric capacity of Si is almost 3x that of the currently used negative material graphite.[7] Because of this high energy density, Si-based negative electrodes have been investigated for decades.[10,11] A hurdle researchers

have faced with this material is its transformation into a crystalline $Li_{15}Si_4$ phase during lithiation.[12] Nanostructured Si alloys in negative electrodes, though, do not form $Li_{15}Si_4$.[13] This phase formation has been associated with capacity fade; however, direct proof of this has not been reported.[7] This thesis will first provide some background into the strengths and shortcomings of Si-based negative electrodes in rechargeable Li-ion batteries. Afterwards, an investigation into the unique behaviour of Si as a negative electrode will be presented and new theories proposed to explain this behaviour.

1.1 Lithium-Ion Batteries

Rechargeable Li-ion batteries are comprised of many components, but usually have a positive electrode (cathode), negative electrode (anode), nonaqueous electrolyte, and porous separating membrane.[14] Utilizing this setup allows chemical energy to be converted into useable electrical energy. The positive electrode is usually a layered transition metal oxide that contains lithium in a relatively stable phase, supplying a finite amount of lithium to the system.[15] The negative electrode is usually a layered graphitic carbon that is void of lithium in the discharged state, but saturated with lithium in the charged, or ready-to-use state.[15] In order for lithium ions to flow from one electrode to the other, an ionically conducting but electronically insulating electrolyte is used. Electrolytes for Li-ion batteries are organic, nonaqueous liquids, with a lithium-based salt dissolved within the solvent.[15] The most popular solvents are cyclic and/or linear carbonates such as: ethylene carbonate (EC), propylene carbonate (PC), dimethyl carbonate (DMC), and ethyl methyl carbonate (EMC).[15] These solvents are used because they dissolve salts well, have a wide stable electrochemical voltage window, and are reasonably inexpensive and safe. The most

common salts for Li-ion batteries are $LiPF_6$, $LiBF_4$, $LiB(C_2O_4)_2$, and $LiN(CF_3SO_2)_2$.[15] These salts have high solubility, relatively low cost, are thermally stable, and can be beneficial toward solid electrolyte interphase layer (SEI) formation.[15] This SEI layer is a passivating surface layer of semisolid electrolyte that forms upon reaction with the anode, protecting the anode from future reactions with the electrolyte.[16] Lastly, the porous membrane (or separator) is a material sandwiched between the positive and negative electrode that adsorbs electrolyte within a percolating network of pores, allowing for Li-ion diffusion while being electronically insulating, and thus preventing the two electrodes from coming into electrical contact. Celgard® is one of the more widely used separators, made up of a polypropylene/ polyethylene/polypropylene (PP/PE/PP) trilayer that has been stretched to enlarge its pore size.[15]
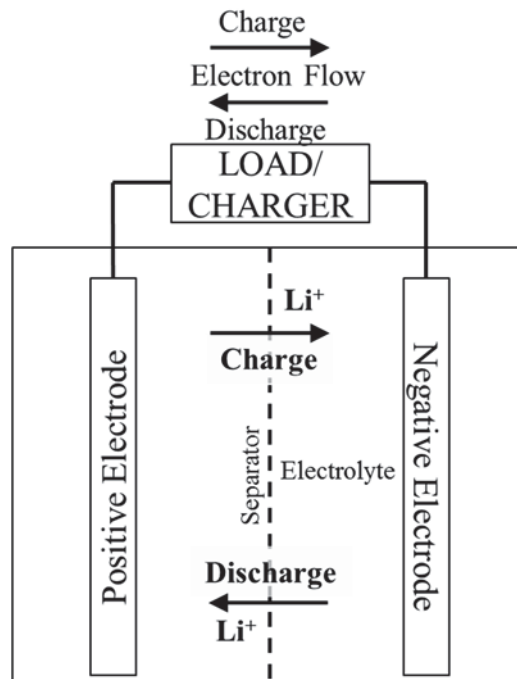
Figure 1.1. Schematic diagram of a Li-ion cell.

A schematic diagram showing the chemistry at work in a Li-ion cell is shown above in Figure 1.1. As illustrated, a Li-ion cell has positive and negative electrodes that are

separated from one another by a porous separator that contains electrolyte. These electrodes are connected to an external circuit. During charge, the cell is connected to an external potential difference, causing Li^+ ions to migrate towards the negative electrode through the electrolyte. Simultaneously, electrons pass from the positive to negative electrode via the external circuit to maintain charge neutrality. This charge migration reduces the negative electrode and oxidizes the positive electrode. During discharge the opposite processes spontaneously occur, oxidizing the negative electrode and reducing the positive electrode and causing electrons to flow spontaneously through the external circuit from the negative electrode to the positive electrode.

These spontaneous reactions are driven by a chemical potential difference between the negative and positive electrodes with respect to lithium. The resulting cell voltage, V, can be expressed as:

$$V = -\frac{\mu_{cathode} - \mu_{anode}}{ne} \tag{1.1}$$

where e is the magnitude of charge of an electron, n is the number of electrons taking part in the reaction, and $\mu_{cathode}$ and μ_{anode} are the chemical potentials of the positive and negative electrode with respect to lithium, respectively, in electron volts.

1.2 Negative Electrodes in Li-ion Batteries

Carbons have dominated the negative electrode market since the commercialization of the Li-ion battery in 1991.[17–19] Figure 1.2 shows the chemical potentials of several negative and positive electrode materials.[20] Here it can be seen that carbonaceous materials have the lowest chemical potential difference versus Li, resulting in the largest potential

difference between the carbonaceous negative electrode and the positive electrode. Furthermore, since cell energy can be expressed by:

$$E = QV \qquad (1.2)$$

where E is the energy in Joules, Q is the charge in coulombs, and V is the cell potential (V), the low chemical potential of carbonaceous materials is therefore very advantageous for rechargeable Li-ion batteries.
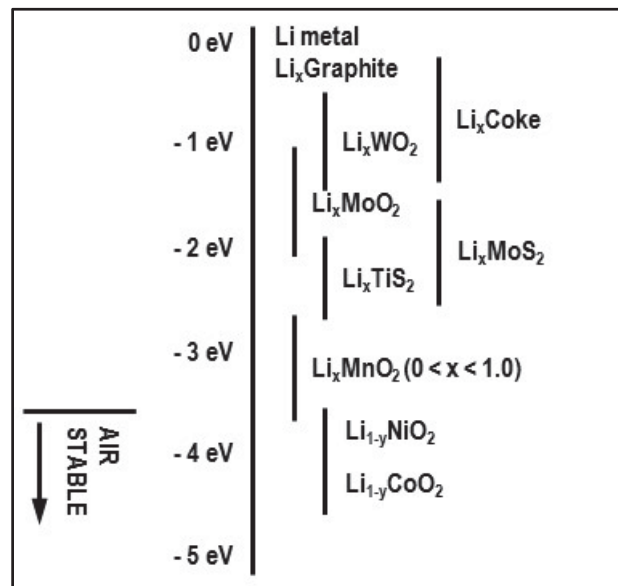
Figure 1.2. Showing the chemical potential ranges of intercalated Li in a variety of compounds. Chemical potentials are measured relative to Li metal. Styled after Reference 20.

The use of graphite as a negative electrode for Li-ion batteries was first documented and patented by Samar Basu of Bell Telephone Laboratories in 1983.[21] Over the years, other carbonaceous materials have been examined,[22] but since graphite has high reversibility, low voltage, and high volumetric capacity it has been implemented into conventional lithium-ion batteries as the active material in negative electrodes. Graphite stores charge via the reversible intercalation of lithium ions, giving it a theoretical capacity

of 372 mAh/g, or 719 mAh/mL.[22] Its electrochemical reaction with Li can be represented by:

$$Li^+ + 6C + e^- \rightleftharpoons LiC_6 \qquad (1.3)$$

Graphite has long cycle life, is abundant in nature, easily processed, and packs well, resulting in dense electrode coatings. Furthermore, graphite has low voltage hysteresis, average voltage, and irreversible capacity, making it an exceptional negative electrode material that is difficult to surpass.[7]

1.3 Alloy-based Negative Electrodes for Li-ion Batteries

The remarkable performance of graphite in Li-ion batteries is well known; however, to further improve on the energy density of modern batteries, much research has been placed toward alloy-based negative electrodes.[23–26] Unlike graphite or other carbons that reversibly insert Li^+ via intercalation processes, Li insertion into alloy negative electrodes involves the breaking and reformation of bonds in the host structure.[19] This process alters the host structure and results in volume expansion (~9 mL/mol Li), but also allows alloys to exhibit very high volumetric and gravimetric capacities, as shown in Figure 1.3.[7,19] Figure 1.3 shows that a pure Si negative electrode has almost 10× the gravimetric capacity as graphite and 3× the volumetric capacity. It should be noted, that in the majority of battery applications, volumetric capacity is the more important metric (e.g. in electric vehicles and cellphones), and these are the values that have attracted the scientific community to alloy-based negative electrodes.[7,19] Average voltage, however, also has to be taken into account in order to gauge cell energy density.
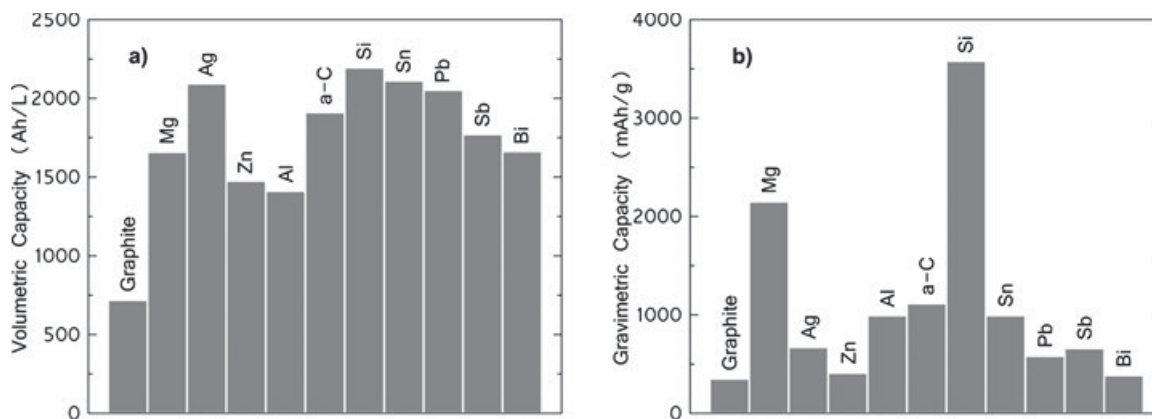
Figure 1.3. The bar graphs, (a) and (b), represent the volumetric and gravimetric capacities of various fully lithiated negative electrode materials, respectively. Reprinted with permission from Reference 7. Copyright 2014 American Chemican Society.

A more accurate method toward quantifying the promise of alloy negative electrodes involves using a realistic cell system that includes average electrochemical cycling voltage into energy density calculations and compares the resulting capacities to that of a graphite-based negative electrode system. Obrovac and Chevrier modeled different negative electrodes in their recent alloy negative electrode review using the cell stack shown schematically in Figure 1.4.[7] In this figure, the thicknesses and composition of each component is fixed, except for the negative electrode thickness, which is allowed to vary since higher energy density negative electrode coatings can be expected to be thinner while matching the capacity of the positive electrode. This is an appropriate approximation since it acts as a reasonable unit cell for modern Li-ion batteries.
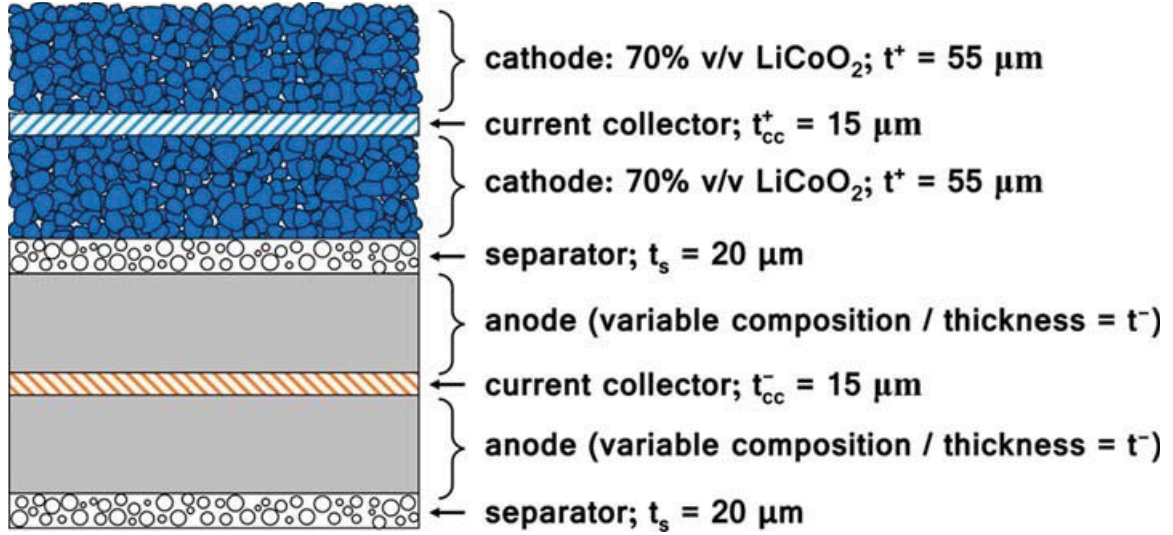
Figure 1.4. Cell stack used by Obrovac and Chevrier to model the impact of different anodes on cell energy density. t^+, t^+_{cc}, t_s, t^-, and t^-_{cc} represent the thicknesses of the cathode material, the aluminium current collector for the cathode, the separator, the anode material, and the copper current collector for the anode, in microns, respectively. Reprinted with permission from Reference 7. Copyright 2014 American Chemican Society.

Cell stack energy density in Wh/L using the cell stack modeled in Figure 1.4, as shown by Obrovac and Chevrier in their review,[7] can be expressed as:

$$\breve{U}_R = \frac{(58\,327.5\ Ah/L)}{70 + (110)\left[1 + \dfrac{\left(583.275\frac{Ah}{L}\right)}{\tilde{q}_R^-}\right]}[(3.10\ V) - V_{avg}^-] \tag{1.4}$$

where $\breve{U}_R$ is the resulting cell stack energy density (in Wh/L), and $\tilde{q}_R^-$ and V_{avg}^- are the volumetric capacity (in Ah/L) and average voltage (V) of the negative electrode, respectively. Although volumetric capacity plays a significant role in cell stack energy density, equation 1.4 shows that $\breve{U}_R$ is more dependent on V_{avg}^-. Using this equation, the resulting cell stack energy densities for different alloy anode materials are shown in Figure 1.5.
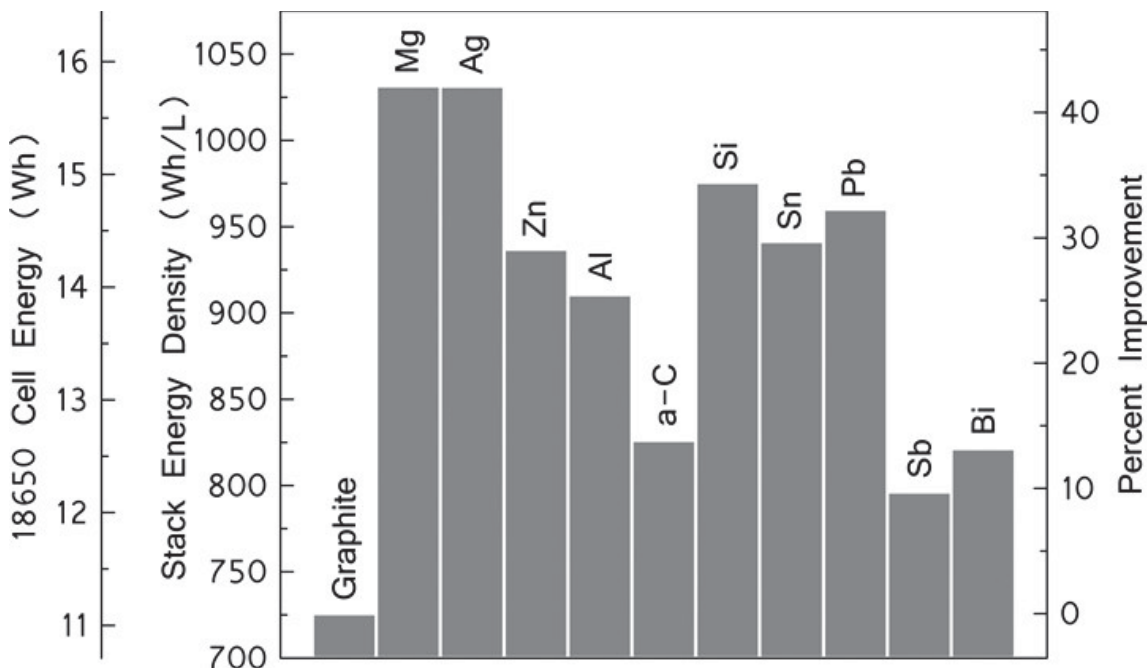
Figure 1.5. Calculated stack energies for different negative electrode active materials. The right-hand side axis indicates the percent improvement in energy over a graphite electrode. A scale was also provided with 18650 cell energies based on the model. Reprinted with permission from Reference 7. Copyright 2014 American Chemican Society.

Figure 1.5 graphs the calculated (from equation 1.4) stack energy density, percent improvement (relative to a stack containing a graphite negative electrode), and the resulting 18650 cell energy (in Wh) for the 10 Li-ion alloy negative electrode materials shown in Figure 1.3. In calculating the stack energy density of these alloy negative electrodes, coating porosity was assumed to be zero, and the irreversible capacity was assumed to match the cathode (70 % by volume $LiCoO_2$). Because of these assumptions, Figure 1.5 represents the maximum possible increase from implementing alloys into a cell stack.

The top five alloy negative electrode materials in order of decreasing energy density are therefore Mg, Ag, Si, Pb then Sn. Table 1.1 shows the characteristics of each of these elements and compares them to graphite. It can be seen here that, as expected, the stack energy is largely dependent on average voltage. Ag is far too expensive to act as a major component in Li-ion batteries, and lead is undesirable due to toxicity. Additionally, Mg has

9

low rate capability, and with its average electrochemical cycling voltage of 0.0325 V, has a high risk of Li-plating.[27,28] This leaves Si and Sn as the major candidates for active materials in negative electrodes for Li-ion batteries.

Table 1.1. Characteristics of Li-ion negative electrodes for five of the most energy dense alloying elements. Data for columns 3, 4, 5, and 6 were obtained from Reference 7.

Element	Highest Lithiated Phase	Expansion / %	Average Voltage / V	Stack Energy / Wh/L	Energy Increase / %
Graphite$_{Baseline}$	LiC$_6$[22]	10	0.125	726	0
Ag	γ_3-Li$_{2.7}$Ag[24]	236	0.175	1031	42
Mg	Li$_{1.95}$Mg[27]	125	0.0325	1032	42
Pb	Li$_{4.5}$Pb[7]	222	0.423	960	32
Si	Li$_{15}$Si$_4$[12]	280	0.400	976	34
Sn	Li$_{4.4}$Sn[29]	244	0.504	941	30

Si and Sn are the two most studied alloy negative electrode materials and both have made their way, to a small degree, into the battery market.[30–32] Table 1.2 shows a cost analysis of the use of Si and Sn negative electrodes compared to graphite. From this table it can be seen that Si is by far the most economical material for Li-ion negative electrodes on a cents/Ah basis. For this reason, the work in this thesis was focused on gaining a deeper understanding into the electrochemical behaviour of Si with the hope that this knowledge can be a stepping-stone for the scientific community to improve its cycling performance and ultimately the energy density of Li-ion batteries.

Table 1.2. Raw material cost analysis of graphite, Si, and Sn.

Material	Cost / $/kg	Theoretical Capacity / Ah/kg	Cost per unit Energy / ¢/Ah
Natural Graphite	3.00[33]	370	0.81
Silicon	2.85[34]	3579[12]	0.08
Tin	15.00[35]	993[7]	1.51

1.4 Si-based Negative Electrodes for Li-ion Batteries

The high energy density of Si, combined with its natural abundance has made it one of the most highly studied Li-alloy negative electrode materials.[7,10,36] Prior to 2004, though,

very little was known about its electrochemical behaviour.[12] Due to the use of coating formulations that were unable to deal with the 280 % volume expansion experienced by Si during lithiation, large capacity fade would occur in just a few cycles, as shown in Figure 1.6.[10] It can also be seen here that ground Si nearly reaches its theoretical capacity of 3579 mAh/g during its first lithiation, has a low average voltage, large hysteresis, and low delithiation capacity.
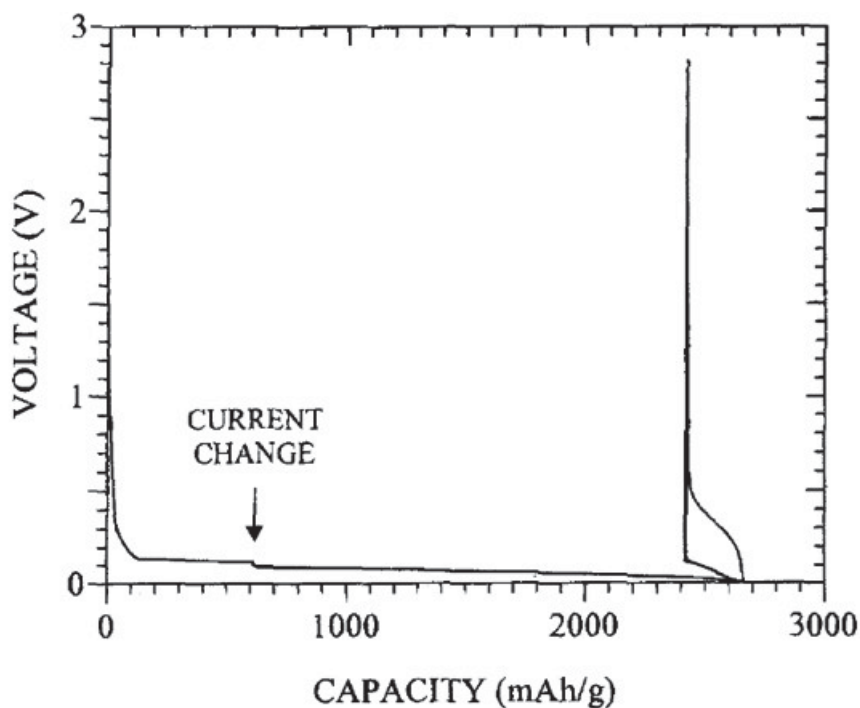
Figure 1.6. First discharge, charge, and second discharge of a cell made from ground pure silicon. Reprinted with permission from Reference 10. Copyright 1995 Electrochemical Society.

In 2004 Obrovac and Christensen performed a detailed *ex-situ* X-ray diffraction (XRD) study on the electrochemical reaction of lithium with silicon.[12] In this study, they confirmed the transition from a crystalline to an amorphous structure upon lithiation and discovered the formation of crystalline $Li_{15}Si_4$ below 70 mV. This was a significant finding, since $Li_{15}Si_4$ is a metastable phase not present in the Li-Si phase diagram and only appears during electrochemical cycling.[12] In a later study, Li and Dahn performed an *in-situ* XRD

11

study on crystalline Si (*c*-Si) negative electrodes, in order to elucidate the complicated electrochemical alloying mechanism of crystalline and amorphous Si with lithium.[37] A major finding of the investigation was a description of the detailed phase behaviour that occurs during the electrochemical insertion of Li into Si, shown in Figure 1.7.
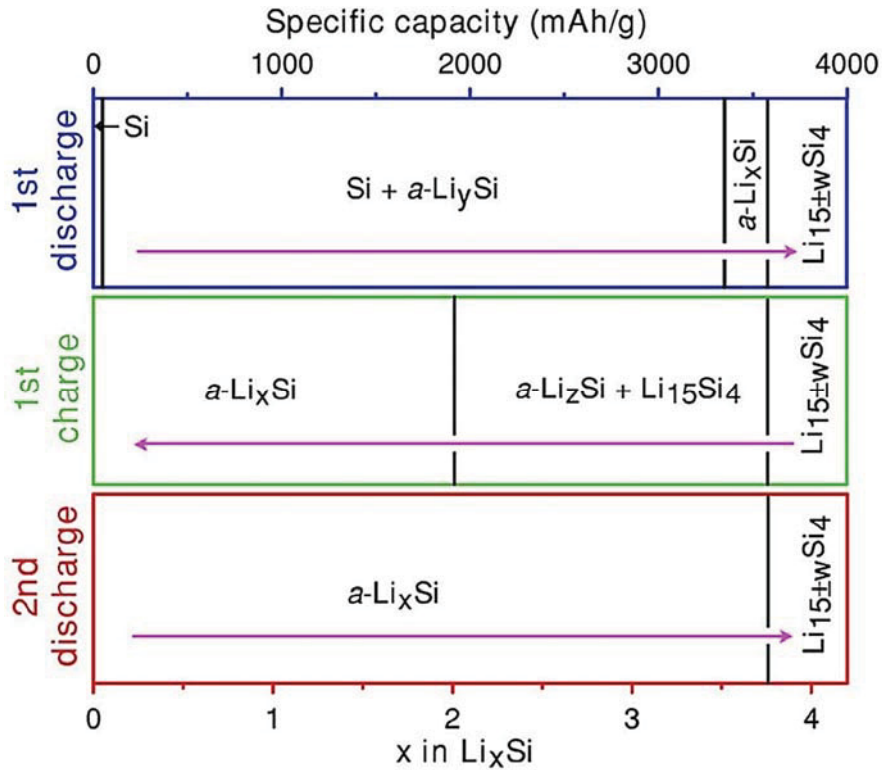
Figure 1.7. Phase diagram describing the phases that form during the charge-discharge cycling of a Li/Si electrochemical cell between 0.005 and 0.9 V at room temperature. Reprinted with permission from Reference 37. Copyright 2007 Electrochemical Society.

As *c*-Si is lithiated, it becomes increasingly reduced into amorphous Li_ySi (*a*-Li_ySi) until reaching a capacity of 3350 mAh/g ($y = 3.5$). When all of the *c*-Si is consumed, a variable lithium composition phase forms (*a*-Li_xSi), then *a*-Li_xSi entirely crystallizes to form $Li_{15}Si_4$ at about 60 mV. During charge, $Li_{15}Si_4$ is delithiated and coexists with the, less lithiated, amorphous *a*-Li_zSi phase, where *z* was determined to be about 2.0. For the remainder of the charge and during subsequent discharges, the stoichiometrically variable *a*-Li_xSi phase is the only phase present above 60 mV.[37]

To understand the electrochemistry taking place during the charge and discharge of a-Si, Li *et al*. performed an *in-situ* Mössbauer (MS) study on tin-doped amorphous Si prepared using magnetron sputtering.[38] a-Si exhibits two plateaus during lithiation in the voltage curve, as shown in Figure 1.8. Additionally, these two plateaus are replaced by one prominent plateau in the delithiation profile when $Li_{15}Si_4$ is formed (lithiate to below 60 mV) during discharge. The phases during delithiation will be those shown in the first charge section of Figure 1.7.
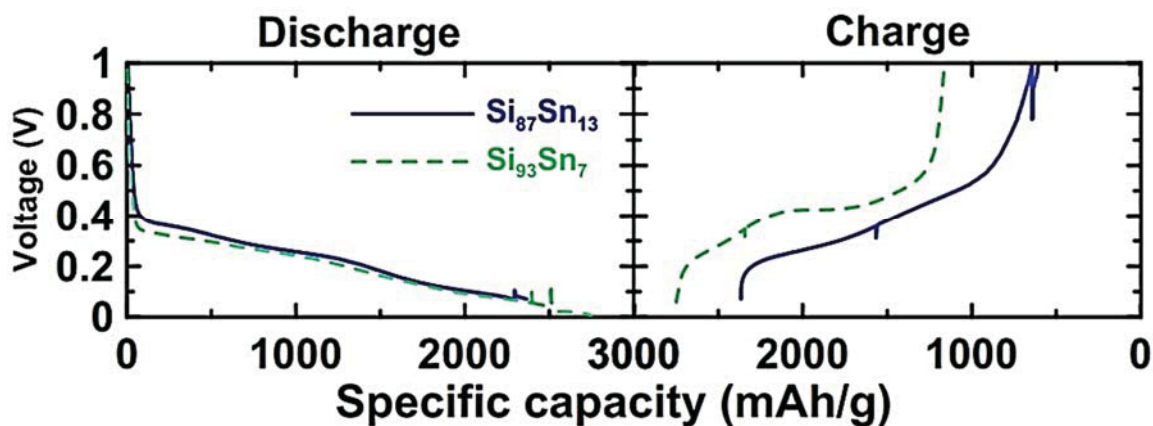
Figure 1.8. Potential versus specific capacity profile for the Li / a-Si$_{87}$Sn$_{13}$ (solid line) and Li / a-Si$_{93}$Sn$_7$ (dashed line) *in-situ* MS cells. The Li / a-Si$_{87}$Sn$_{13}$ and Li / a-Si$_{93}$Sn$_7$ cells were discharged to 0.070 and 0.005 V, respectively and charged to 1 V using a current corresponding to a C/200 and C/140 rate, respectively. Reprinted with permission from Reference 38. Copyright 2009 Electrochemical Society.

Ultimately, this *in-situ* MS study allowed Li *et al*. to determine that the two gently sloping plateaus in the discharge profile correspond to two arrangements of Li atoms in the host structure. The higher voltage plateau is a result of Li-ions being inserted into environments where each Li has primarily Si neighbors, whereas, at lower voltages the Li atoms have primarily Li neighbours, meaning that their insertion voltage will be closer to that of Li-plating (occurring at 0 V vs Li).[38]

Overall, Si undergoes a complex electrochemical reaction with Li. As shown in this section, a significant amount of research has gone into understanding this mechanism in order to harness the high energy density of Si. Similar to previous studies, the work in this thesis aims toward acquiring a deeper understanding into the electrochemical behavior of Si. Particularly, work in this thesis focused on clarifying the conditions for and implications of $Li_{15}Si_4$ formation during the lithiation of Si, via electrochemical testing of Si thin films as negative electrodes in Li half-cells, and investigating the role of compliant layers on the electrochemical behavior of Si thin films.

1.5 Organization of Thesis

Chapter 2 outlines the experimental techniques used in this work. Electrode preparation, cell assembly, electrochemical measurements, and materials characterization techniques are discussed.

Chapter 3 presents a study motivating and showing implications of $Li_{15}Si_4$ formation. Films of different thicknesses deposited onto various substrates and cycled at multiple rates are examined electrochemically and imaged at points during cycling. An electrochemical characterization method where peaks are fit in the differential capacity profile is employed, leading to a deeper understanding into the conditions for $Li_{15}Si_4$ formation. Ultimately, a model is proposed for $Li_{15}Si_4$ formation in Si thin films that can be extended to other systems, and the effect of $Li_{15}Si_4$ formation on cycling performance is briefly investigated.

In Chapter 4, the knowledge presented in Chapter 3 is applied to test the performance of various binders. First, a coating formulation is optimized for bulk Si,

14

utilizing polyimide as a binder, then this formulation is tested with other binders to examine differences in performance using $Li_{15}Si_4$ formation as a probe. Afterwards, this optimized formulation is applied to *n*-Si coatings to be able to have a clearer view of the effect of binder on $Li_{15}Si_4$ formation in composite coatings.

In Chapter 5, a compliant layer is introduced between the film and substrate in order to eliminate film/substrate interactions and obtain electrochemical behaviour more similar to powdered negative electrode materials in composite coatings. In this section, multiple compliant layer compositions are investigated, and their performance is compared to the Si thin films in Chapter 3 and composite electrode coatings shown in Chapter 3. Lastly, a binary film is sputtered onto a compliant layer and the electrochemical behaviour is examined and compared to a ball-milled alloy of the same composition in a composite coating.

Chapter 2 Experimental Techniques

2.1 Magnetron Sputtering

Magnetron sputtering was the main technique used to acquire amorphous Si in this work. Magnetron sputtering is a type of sputter deposition that is capable of producing a thin film of a desired composition onto a substrate.[39,40] These film-covered substrates can then be implemented into electrochemical cells as electrodes. Unlike electrode coatings, thin films deposited onto a current collector lack binders and conductive diluents, making them useful for studying the electrochemical behaviour of pure materials. In magnetron sputtering, targets of a desired composition are chosen so that their material make-up can be subsequently deposited onto a substrate. In this project, only Si targets were used except for one experiment, in which an Fe target was also used.

During the sputtering process, electrons collide with Ar ions, creating an Ar^+ plasma. This plasma is then directed and accelerated toward prepared negatively biased targets. As Ar^+ collides with the target, the target material is ejected and deposited onto the substrate-covered sputtering table. Additionally, when Ar ions collide with the target, secondary electrons from the target material are ejected.[40] These secondary electrons ionize Ar atoms that are supplied to the chamber, continuing the plasma. In magnetron sputtering, magnets are placed behind the targets. These magnets create magnetic fields that cause secondary electrons to travel in a spiral close to the targets, increasing their travel time and the number of Ar ions they can ionize.[40] When using multiple targets, homogeneous mixing of the sputtered materials is accomplished through rotation of the sputtering table. The table

used in this work rotated at 15 rpm. Film composition can be modified by covering targets with appropriately designed masks.[41]

A modified Corona Vacuum Coaters V-3T deposition system equipped with a 500 L/s turbo pump and Polycold system was used (located in the Sir James Dunn Physics Building of Dalhousie) for all sputtering experiments. In most sputtering runs, the table was first covered with Al foil (Alcan), then that foil was entirely covered with electrolytic Cu foil (Furukawa Electric, Japan). The table was first covered with Al foil so that the adhesive coated onto the sputtering table would not come into contact with the electrolytic Cu foil used as the current collector in negative electrodes. Additionally, 6 to 15 electrolytic 1.26 cm^2 Cu foil discs were weighed using a Sartorius SE-2 microbalance (± 0.1 µg resolution) and arranged linearly (into lines of 7) onto the 7.62 cm sputtering track. This sputtering track began 8.4 cm from the table's center. Additionally, a silicon wafer partially covered with Scotch tape (3M Company) was sputtered upon in each cycling run. The tape was subsequently removed and the sputtered wafer was then used to determine film thickness for each run using a Sloan DekTak profilometer. Figure 2.1 is an image of the prepared sputtering table following film deposition. After film deposition, the back of each disc was cleaned of adhesive using a cotton-tipped swab soaked in methanol, then weighed once again on a Sartorius SE-2 microbalance to determine the mass loading of Si film. Either the exact mass loadings (determined by difference) were used when calculating a theoretical capacity, or these exact masses were used to determine Si film mass as a function of position on the substrate.
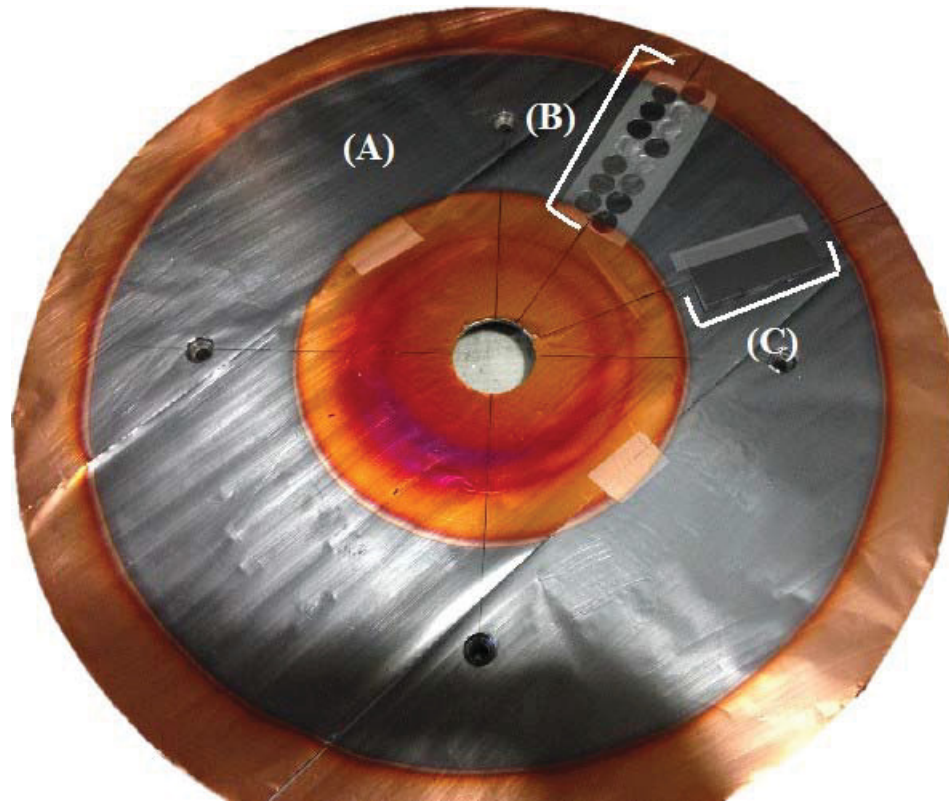
Figure 2.1. Image of the film-covered sputtering table. (A) indicates the film of Si sputtered directly onto the electrolytic Cu foil, (B) indicates Cu discs used to determine film mass, and (C) the partially taped Si wafer.

Four different sputtering procedures were used in this thesis; all are detailed in Table 2.1. In each sputtering run, only constant masks were used so that there would be a nearly constant composition and film thickness over the entire sputtering table. A "(×2)" in the "Si / W" column of Table 2.1 means that two Si targets were used in sputtering runs following that procedure. All sputtering procedures utilize a Cr plasma clean procedure in order to sputter away surface impurities on the substrate. In this process, a large volume of oxygen, and a small amount of Ar is passed into the sputtering chamber and ionized into O^{2-} and Ar^+, respectively. The O^{2-} ions are projected towards the sputtering table partially etching the the sputtering table, while the small amount of Ar^+ is directed towards the Cr target, causing a very small amount of CrO to deposit onto the substrate surface. Additionally, column four in table 2.1 provides the total W/min of Si and Fe for each

18

sputtering procedure. As long as the power (in columns 1 and 2) is constant, this measurement is a viable means to compare the amount Si deposited from one procedure to another when varying the sputtering time. The film mass, however, is not perfectly linear with total W/min since target thickness (from use) and/or sputtering chamber conditions can vary and affect deposition rate.

Table 2.1. Summary of the various sputtering conditions used and their details in this thesis.

	Power Supplied to Targets				
Procedure #	Si / W	Fe / W	Total W/ min Si / Fe	Measured Film Thickness / nm	Mass Loading / mg/cm^2
1	150	0	42 750 / 0	400	0.119
2	150 (×2)	0	40 000 / 0	400	0.119
3	150	0	26 500 / 0	275	0.060
4	150	20	31 320 / 4 180	300	0.130

2.2 Leaching Cu Substrate and Recovery of Si Flakes

In one instance (using a film prepared from procedure #2, Table 2.1), the Cu foil substrate was removed so that the Si film could be recovered as flakes. In order to remove the Cu foil, an apparatus was prepared consisting of a 100 mL 3-necked round-bottomed flask mounted onto a heating mantle equipped with a condenser and thermometer. Argon was then passed through the apparatus. First 50 mL of 3 M HNO$_3$ was made by appropriately diluting concentrated HNO$_3$ (Caledon, 68.0 % by weight) with distilled water. The resulting HNO$_3$ solution functioned as the Cu leachant. This solution was then transferred to the 3-necked flask and heated to boiling under argon to deoxygenate the liquid. After allowing this solution to cool, the Si film covered Cu foil was cut into strips and fed into the solution. The solution was stirred with a stir bar at 500 rpm and left to stir for 2 hours. The resulting amorphous Si flakes were recovered through suction filtration and washed with distilled water.

2.3 Imaging Techniques

2.3.1 Scanning electron microscopy

Scanning electron microscopy (SEM) measurements were performed using either a Phenom G2-pro tabletop SEM (located in the Sir James Dunn Physics Building of Dalhousie), or a Hitachi Coldfield Emission SEM S4700 (located in the A.E. Cameron Building of Dalhousie) with an Oxford Analytical INCA energy dispersive X-ray detector spectrometer (EDS) attachment. SEM samples were mounted onto an SEM stub with carbon tape, and then transferred into the SEM chamber. Scanning electron microscopes bombard a sample with electrons and their detector collects secondary electrons (SE) or backscattered electrons (BSE) that are ejected from the sample.[42] Measurements taken with the Phenom G2-pro and the Hitachi Coldfield Emission SEM S4700 detect BSE or SE and SE, respectively. Secondary electrons originate from within a few nanometers of the sample surface, therefore by detecting these it is possible to create a well-resolved image of the sample.[42] BSEs originate from the electron beam incident on the sample.[42] These electrons then interact with the sample and are scattered, among which some reach the detector. Because heavier atoms deflect more electrons, BSE images tend to have brighter regions where there are heavier atoms and darker regions at lighter atoms.

2.3.2 Energy dispersive detector X-ray spectrometry measurements

Energy-dispersive X-ray spectroscopy was used to map the composition of a region following focused ion beam (FIB) ablation. When the electron beam (used in SEM) interacts with atoms in the sample, it causes atomic inner shell electrons to be ejected, creating a hole. An electron from the outer shell subsequently fills this hole, and the energy

20

associated with this relaxation is emitted as a characteristic X-ray. EDS utilizes a detector that counts these characteristic X-rays, and matches their energy to a specific element. Overall, the counts of these characteristic X-rays allow EDS to quantify the elemental composition of a sample.[43]

2.3.3 Focused ion beam ablation

FIB is a well-known fine ablation technique that is usually coupled with SEM. In this project, FIB was used to create micron-deep holes into a Si film covered compliant layer (see Section 5.3.2) in order to measurement the penetration depth of Si into the layer. An FB-2000A, 30 kV Ga-ion FIB was used (located in the A.E. Cameron Building of Dalhousie) to precisely ablate away sample surfaces. In FIB an ion beam composed of a heavy element ion, in this case Ga, is shot toward the sample and used to remove a fine layer of the material under investigation.[44] The current can be modified depending on the goals of the researcher. If a low current is used, a high-resolution image of the sample can be obtained via a secondary electron signal (seen in Section 2.3.1). This causes minimal ablation to the sample surface. If a high current is used, a controlled amount of the sample surface, in a specific region, can be removed by the high-energy Ga ions. In this project, the FIB was set to ablate certain regions in a stepwise manner. Using this method, it is possible to gather information about the existing composition at a variety of depths and it also allows for thorough cross-sectional analysis of samples. FIB ablation was coupled with SE detection, SEM and EDS measurements.

2.4 Electron Microprobe

Electron microprobe measurements were performed to determine the composition of a sputtered Si-Fe film. Electron microprobe samples are bombarded with an electron beam, causing the sample to emit X-rays characteristic of certain elements toward a detector.[45] The detector is first calibrated against a standard of known composition, in this case FeSi$_2$, allowing it to quantify the elemental composition of the sample based on the counts of emitted X-rays. Following calibrations, accurate sample compositions can be determined. Measurements were taken using a JEOL 8200 Superprobe, equipped with an xy-translation stage (located in the Life Sciences Centre of Dalhousie). The sample was irradiated with a 50 μm diameter electron beam at 50 nA and 5 keV.

2.5 Electrode Coating Fabrication

Generally, coatings were composed of an active material (optional), a conductive diluent, and a polymeric binder. These were combined with a solvent in which the binder is soluble and mixed in a 40 mL hardened stainless steel planetary mill vial, containing 2-4 1.27 cm tungsten carbide balls, using a Retsch PM 200 planetary mill. The active materials used were bulk Si (Aldrich, -325 mesh, ≥ 99 % purity), Si nanoparticles (*n*-Si, Nanostructured and Amorphous Materials, 30-50 nm, ≥ 98 % purity), recovered amorphous Si flakes (see Section 2.2), and MAG-E graphite (Hitachi). Polyacrylic acid (PAA, Aldrich, 35 % by wt. in H$_2$O, MW ~ 250,000 g/mole), lithium polyacrylate (LiPAA, made by neutralizing PAA with LiOH·H$_2$O (Aldrich, ≥ 98 % purity)), polyimide (PI2555, HD MicroSystems), FC2179 fluoroelastomer (Dyneon), and polyvinylidene fluoride

(PVDF, Aldrich, average MW ~534 000) were used as binders. Distilled water was used as the solvent when LiPAA or PAA binder was used. N-methyl-2-pyrrolidone (NMP, Aldrich, ≥ 99.5 % purity) was used as the solvent for all other binders. Typically, the total amount of solids in the slurry was ~ 2 g, and typically about 5 to 10 g of solvent was used. All slurries were mixed in a planetary mill for one hour at 100 rpm. They were then hand-coated onto electrolytic copper foil (Furukawa Electric, Japan) at a thickness of 0.10 mm, using a stainless steel coating bar.

Coatings incorporating a PVDF binder were dried at 120 °C in air using a solvent oven. Coatings using LiPAA or PAA were allowed to dry for one hour in air, and then heated to 120 °C overnight under vacuum. Coatings using FC2179 were dried at 120 °C for 24 hours under vacuum. Lastly, coatings using PI were dried at 120 °C in air in a solvent oven for one hour, then punched into electrodes and heated in a tube furnace under argon at 120 °C for one hour, followed by three hours at 300 °C. These details for each binder are summarized in Table 2.2, along with the coating formulations for all the inactive compliant layers used in this thesis. LiPAA and PAA coatings are hydroscopic and were therefore stored in an Ar-filled glovebox.

Table 2.2. Composite coating details for the inactive compliant layers.

Binder	Binder/SC Ratio by wt.	Heat Treatment	Air Sensitive Y/N	Total Solids Mass Loading (in milling vial) / g
PVDF	60/40	120 °C, 2 hours Solvent oven	N	~1
LiPAA	60/40	120 °C, Overnight Under vacuum	Y	~1
FC2179	70/30	120 °C, 24 hours Under vacuum	N	~1
PI	60/40	120 °C, 1 hour then 300 °C, 3 hours Tube Furnace, Ar flow	N	~1

Compliant layer coatings were made using the same procedures described above. Details concerning prepared active compliant layers are provided in Table 2.3. Additionally, details concerning Si-based (bulk Si, n-Si, and recovered flakes) composite coatings are provided in Table 2.4.

Table 2.3. Characteristics of the active compliant layers used for Si thin films.

Producer / ID	By Mass AM/SC/Binder	Active Material	Binder Identity	Calendered Y/N
Author / I	93.46/0.5/6.04	Graphite	PVDF	N
Magna / II	89.8/NA/4	Graphite	PVDF	Y
Moli / III	N/A	Graphite	N/A	Y
3M / IV	91/0/9	V6 Alloy	LiPAA	Y

Table 2.4. Characteristics of Si powder based composite coatings.

Active Material	Volume Ratio AM/SC/Binder	Mass Ratio AM/SC/Binder	Binder Identity	Total Solids Mass Loading (in milling vial) / g
Bulk Si	70/20/10	73/21/6	PI	~2
Bulk Si	65/20/15	69/21/10	PI	~2
Bulk Si	60/20/20	65/21/14	PI	~2
Bulk Si	55/20/25	61/22/17	PI	~2
Bulk Si	55/20/25	59/21/20	PVDF	~2
Bulk Si	55/20/25	60/21/19	LiPAA	~2
Bulk Si	50/20/30	57/22/21	PI	~2
n-Si	27/20/53	34/25/41	PI	~1
n-Si	27/20/53	31/22/47	PVDF	~1
n-Si	27/20/53	33/24/43	PAA	~1
Si Flakes	16/27/57	20/32/48	LiPAA	~1

2.6 Electrochemical Characterization

Coin cells were constructed in an argon-filled glovebox. The cells consisted, from bottom to top, of a stainless steel (SS) bottom with a polypropylene (PP) gasket attached, followed by a carbon steel spring, a SS spacer, a counter electrode, two layers of separators, the working electrode, and lastly a SS cell top. An image of the coin cell assembly is shown in Figure 2.2. The working electrode is a circular disk created by punching an electrode coating or film with a circular die. Celgard® 2301 was used as the separator material, and lithium foil (Aldrich, ≥99.5 % purity) was used as the counter electrode.
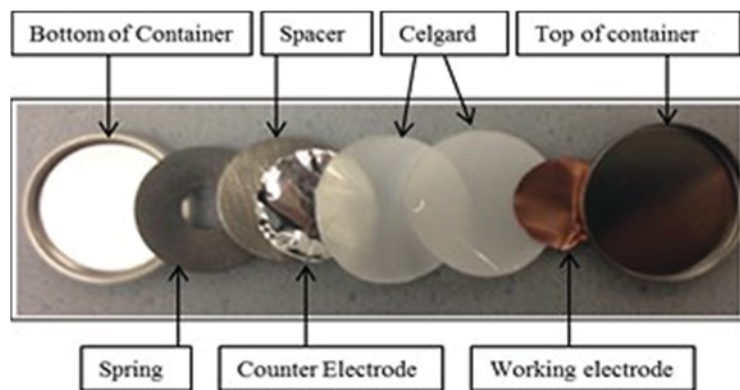
Figure 2.2. Coin cell parts, with representative foils used for the working and counter electrodes. The top and bottom SS can were about the size of a quarter.

Celgard 2301®, as explained in Section 1.1, is a PP/PE/PP trilayer used to separate the electrodes and prevent electrical contact, preventing short-circuiting. A 0.38 mm thick layer of lithium was used as a compliant layer to accommodate rough surfaces in the working electrode. The electrolyte was 1 M $LiPF_6$ (BASF) dissolved in ethylene carbonate (EC) / diethyl carbonate (DEC) / fluoroethylene carbonate (FEC) in a 6/3/1 volume ratio; solvents were battery grade from BASF. After assembly, cells were crimped shut with an argon-powered press using a custom-made crimping die (DPM Solutions). Cells were cycled using a Maccor Series 4,000 Automated Test system at 30 °C between 0.9 and 0.005 V at various C-rates and protocols. These specifications will be explained when presented later in the thesis. A C/2 rate with a C/20 trickle, for instance, means that the cells were run at a current such that it would take 2 hours to obtain full cell capacity (i.e. the calculated theoretical capacity, based on the mass of the active material, multiplied by the specific theoretical capacity of this material), upon reaching 5 mV the voltage is held constant and the current is allowed to equilibrate to C/20 rate before charging.

Chapter 3 $Li_{15}Si_4$ Formation in Si Thin Films

3.1 Introduction and Background

The development of Li-ion batteries that incorporate energy dense silicon-based negative electrodes is challenging, mainly because silicon expands significantly during lithiation. Furthermore, crystalline $Li_{15}Si_4$ has been shown to form during the lithiation of silicon when the voltage becomes less than 50 mV.[12] Acoustic emission studies and imaging techniques have indicated that this phase transition can result in high internal stresses, leading to particle fracture and cell fade.[46] To overcome the issues associated with $Li_{15}Si_4$ phase formation and volume expansion during cycling, researchers have demonstrated high cycle life in Li cells by using Si in the form of nanoparticles,[47,48] nanowires,[49,50] nanopillars,[51,52] thin films,[53,54] and in alloys with inactive or active phases.[13,55] These studies have reported various threshold sizes for nanoparticles (150 nm),[47,48] nanowires (300 nm),[56] and amorphous thin films (2.5 µm),[57] below which $Li_{15}Si_4$ formation does not occur. These results imply that the $Li_{15}Si_4$ phase may be a consequence of particle size; however, the variance in threshold size among Si morphologies raises questions. In particular, the suppression of $Li_{15}Si_4$ formation in thin films that are microns thick is surprising.

Recent studies have shown that the potential of Si electrodes can be significantly modified by applied stress.[58,59] Yang et al. have simulated the effect of a Cu layer bonded to one side of a Si anode on its electrochemistry and predict that it leads to asymmetric diffusion, resulting in stress fields that may limit Li-ion insertion into Si films.[60] Sethuraman et al. have made careful measurements of the effects of applied stress to Si

26

thin films by measuring the substrate curvature changes during electrochemical lithiation and delithiation.[58] They determined the applied stress-potential coupling to be in the range of 100-125 mV/GPa, as shown in Figure 3.1, for Si thin films. As the Si film expands during lithiation compressive stress results from its attachment to a fixed Cu substrate. This compressive stress was found to reach 1.5 GPa before being relieved by plastic flow. During delithiation, the Si film undergoes tensile stress as it contracts. This stress can be relieved by cracking. As a result, the total electrode tensile stress during delithiation was found to be only 0.5 GPa, while the internal film stress during delithiation could not be measured by the methods used by Sethuraman et al., since the crack density was not known. As a result of these studies, it was found that the voltage curve of silicon could be lowered by as much as 200 mV during lithiation. This causes Si electrodes to reach their lower cut off potential at an earlier state of charge, resulting in reduced capacity.

Since $Li_{15}Si_4$ has been shown to form at voltages between 50 - 70 mV, the suppression of $Li_{15}Si_4$ formation in Si thin films observed by Hatchard et al.[57] can easily be accounted for within the magnitude of the lithiation voltage lowering observed from stress due to expansion against the substrate, as reported by Sethuraman et al.[58] The conjecture that $Li_{15}Si_4$ formation in Si thin films can be suppressed by induced stress from a substrate is investigated here and implications for the cycling of Si-alloys in general are discussed.
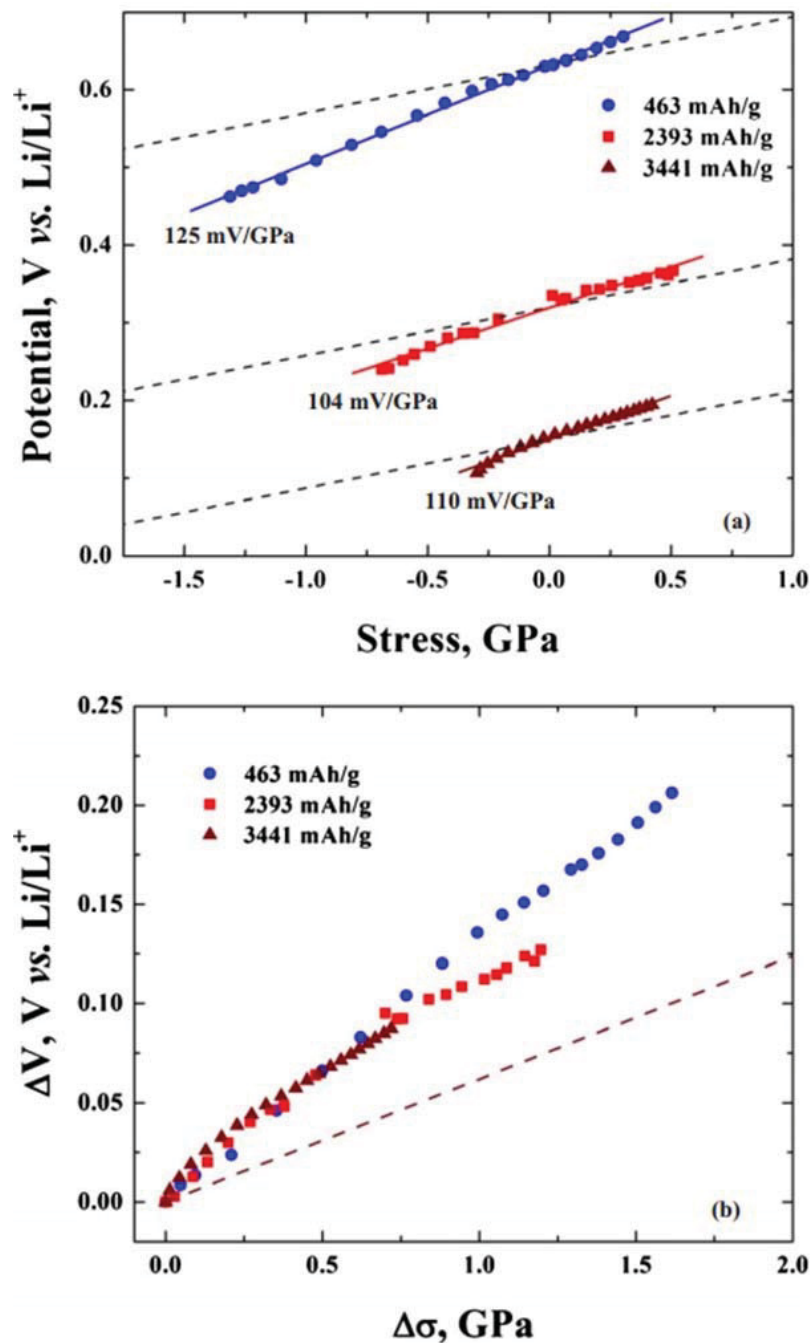
Figure 3.1. (a) Potential and stress values at the end of the open-circuit potential relaxation period in the stress-potential experiments conducted at three different SOCs are shown along with linear fits (solid lines). Potential is corrected for the change in Li concentration due to the incremental delithiation steps in the stress-potential experiments. The dashed line for each SOC represents the Larché–Cahn potential centered around the y-intercept of the linear fit for that SOC. (b) Normalized potential and stress values at the end of the open-circuit potential relaxation period in the stress-potential experiments is shown with the Larché–Cahn potential (dashed line). Reprinted with permission from Reference 58. Copyright 2010 Electrochemical Society.

3.2 Experimental Setup

Samples were prepared by magnetron sputtering using a Corona Vacuum Coater's V3T system. Films were deposited using either one or two Si targets (Pure Tech, 99.9 %) using a DC power supply of 150 W. The films were deposited onto cold-rolled Cu foil (CR-Cu), electrolytic Cu foil (E-Cu) (Furukawa Electric, Japan), and Ni foil (Special Metals Wiggin Ltd.). Some of the foils were roughened using Scotch-Brite (3M Company) prior to sputtering. These foils are designated with a superscript 'R', e.g. as CR-Cu^R (for cold-rolled Cu foil that was roughened). Si film mass was determined via position, using a calibration of the mass as a function of the sputtered film area with reference to pre-weighed Cu foil discs. The sputtering table was prepared as described in Section 2.1, and as shown in Figure 2.1. Scanning electron microscopy (SEM) was performed using a Phenom G2-pro SEM.

Sputtered Si film (400 μm thick) was removed from the copper substrate as described in Section 2.2. The resulting amorphous Si flakes were recovered through suction filtration and washed with water. The washed product was incorporated into an electrode coating comprising the recovered Si flakes, Super C Carbon Black, and lithium polyacrylate in a 20/32/48 weight ratio, prepared as described in Section 2.5. 1.26 cm^2 discs were punched from the sputtered films or from the Si flake coatings and incorporated into 2325 coin cells, as described in Section 2.6. Cells were cycled at a C/2 rate with a C/20 trickle current cutoff at 5 mV during discharge (lithiation), unless specified otherwise.

3.3 Results and Discussion

Figures 3.2 (a) and (b) show the potential versus specific capacity and differential capacity curve, respectively, of a Li half-cell with a negative electrode comprised of a 275 nm Si thin film sputtered onto CR-Cu using one Si target, cycling at C/2 rate with a C/20 trickle.
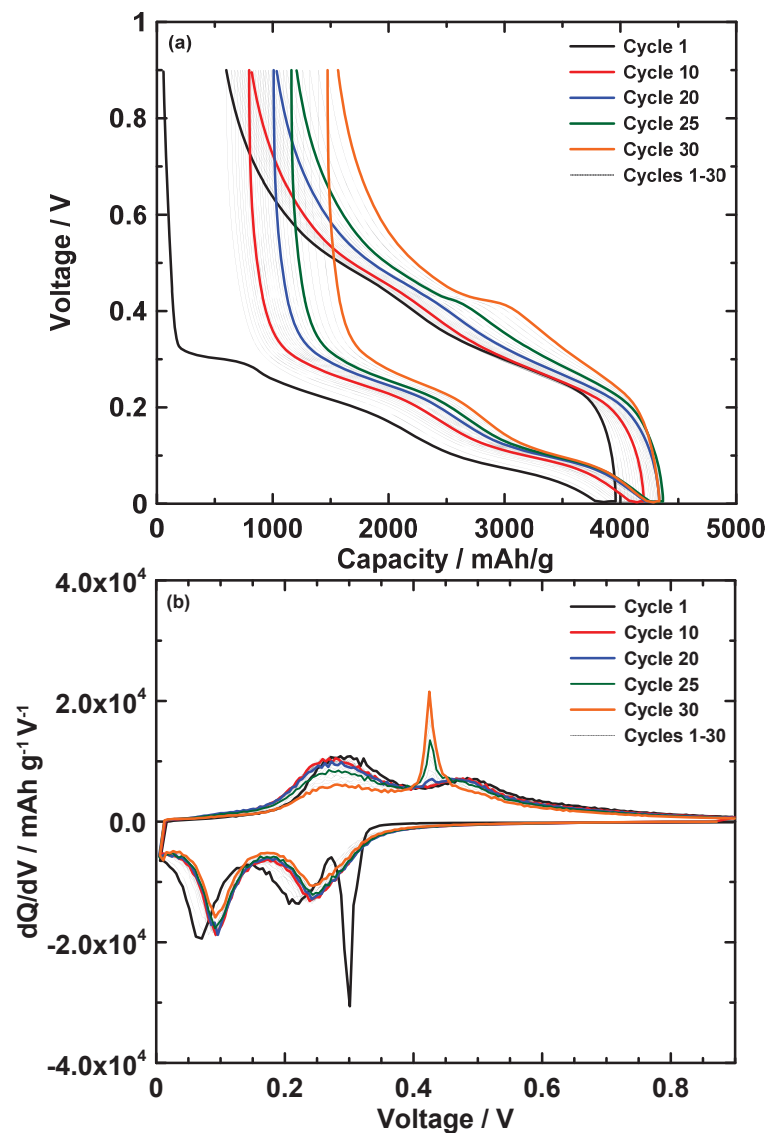
Figure 3.2. (a) Voltage versus capacity and (b) differential capacity curves of a 275 nm thick Si film sputtered onto CR-Cu cycling at a C/2 rate with a C/20 trickle. Cycles 1, 10, 20, 25, and 30 have been highlighted.

This film has a thickness well below the 2.5 µm threshold thickness reported by Hatchard et al.,[57] below which they reported $Li_{15}Si_4$ does not form during 10 cycles. Initially the voltage curve in Figure 3.2 (a) shows a small plateau at about 0.25 V (likely due to nucleation processes during initial lithiation). The voltage and differential capacity curves are then characteristic of amorphous Si for the first 20 cycles; however, there appears to be a significant shift to higher voltage in the lithiation differential capacity profile (about 20 mV) between cycle 1 and cycle 10. To the author's knowledge, this phenomenon has not been previously reported. At cycle 20, a small peak in the delithiation differential capacity appears near 0.42 V, which corresponds to the formation of $Li_{15}Si_4$. As cycling progresses, this peak increases in area during cycling, indicating a substantial increase in the formation of $Li_{15}Si_4$ during cycling. It is likely that Hatchard et al. did not observe the formation of $Li_{15}Si_4$ in their thin films because not enough cycles were measured (Hatchard et al. only reported measuring 10 cycles).[57] As will be shown below, the composition and morphology of the substrate surface can also significantly affect when the $Li_{15}Si_4$ phase is observed.

3.3.1 Process for fitting the peaks of differential capacity curves

Differential capacity delithiation curves were fit using a least squares minimization routine in order to quantify the degree of $Li_{15}Si_4$ formation during cycling, as shown in Figure 3.3. Three pseudo-Voigt peaks and a linear background were found to fit the entire delithiation profiles well. The parameters used to fit peaks in the differential capacity profile were the position, peak area, full-width at half maximum, and shape (mixture of Lorentzian and Gaussian). All parameters of the amorphous delithiation peaks (*a*-Si at 0.3 V, and *a*-Si' at 0.5 V) were allowed to vary until the cycle preceding $Li_{15}Si_4$ formation.

Upon $Li_{15}Si_4$ formation, only the area of the amorphous delithiation peaks was allowed to vary. This was chosen since these peaks were found to shift to lower voltage during early cycling then become fixed in position. The $Li_{15}Si_4$ peak was fit allowing all four parameters to vary during cycling.
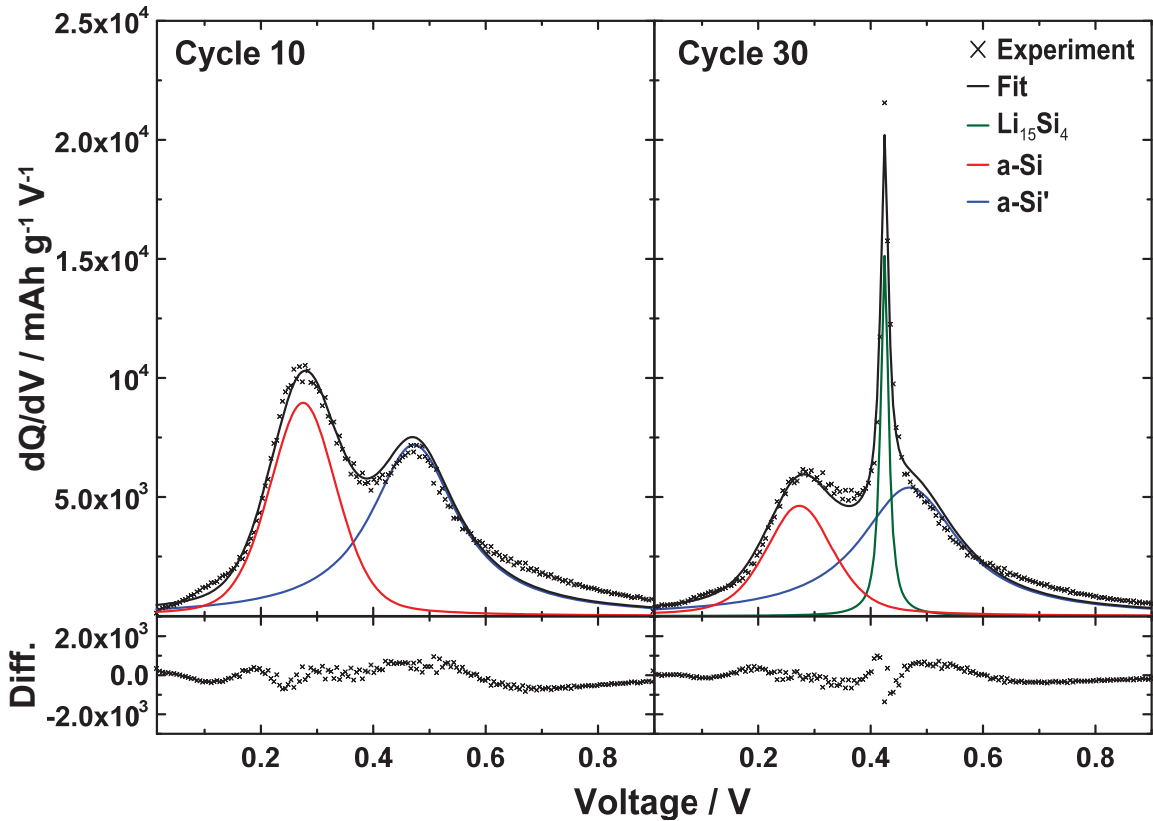
Figure 3.3. Differential capacity curve of (a) the 10th and (b) the 30th charge cycle for the same half-cell used in Figure 3.2. Also shown in these plots are the pseudo-Voight peak profiles used to fit the experimental data, the total calculated fit, and the difference between the fit and experiment.

The peak fitting results are summarized in Figure 3.4, which shows the total delithiation capacity and the relative amount of delithiation capacity from $Li_{15}Si_4$ for the same film shown in Figures 3.2 and 3.3. In this example, no $Li_{15}Si_4$ is present during early cycling; however, after cycle 20 significant amounts of $Li_{15}Si_4$ progressively form. Furthermore, significant capacity fade is coincident with $Li_{15}Si_4$ formation.
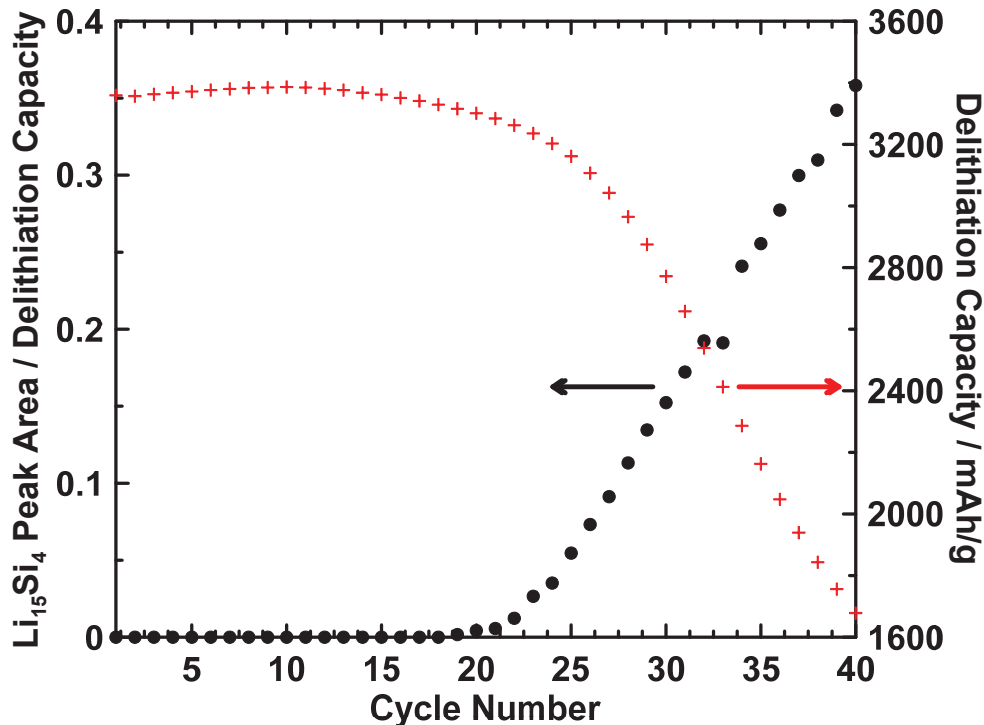
Figure 3.4. Relative $Li_{15}Si_4$ peak area and delithiation capacity vs. cycle number for the same half-cell used in Figures 3.2 and 3.3. Arrows indicate the axis used for each dataset.

3.3.2 SEM investigation of an electrode during the appearance of $Li_{15}Si_4$

In order to understand the physical basis for the observed $Li_{15}Si_4$ formation and coincident fade during cycling, fully delithiated electrodes were examined by SEM as a function of cycle number. Figure 3.5 (a) shows the voltage curve of a 400 nm thick Si film (pro. #2, Table 2.1) sputtered on E-Cu^R. This film forms $Li_{15}Si_4$ early on in cycling. The extent of $Li_{15}Si_4$ can be visualized as the length of the $Li_{15}Si_4$ plateau, which is highlighted in the figure. Figure 3.5 I-IV shows SEM images of this film after cycling 1, 2, 3 and 5 cycles (as indicated by roman numerals in Figure 3.5 (a)). All films were in their fully delithiated state.
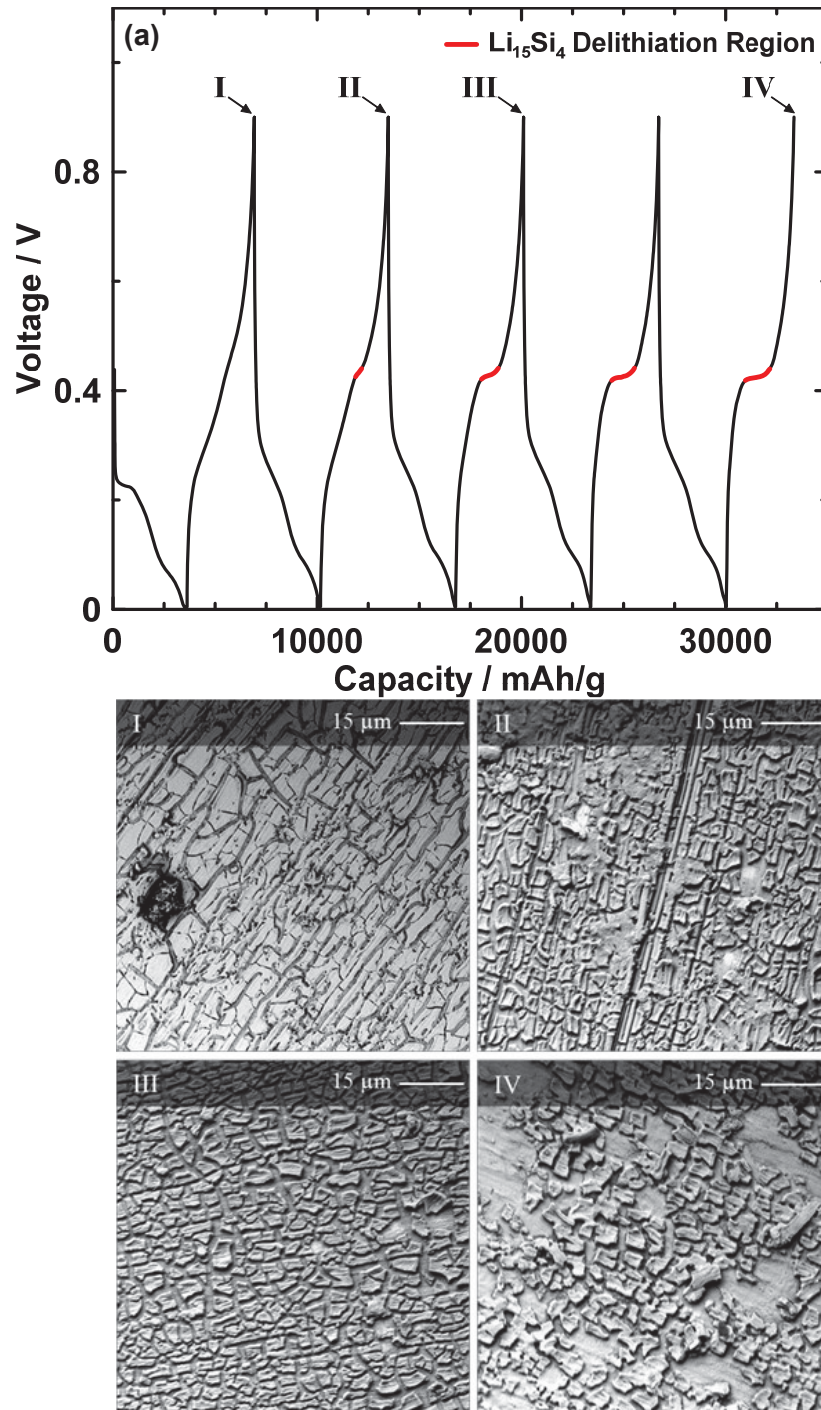
Figure 3.5. (a) Voltage versus capacity curve of a 400 nm thick Si film on E-Cu^R cycling at a C/4 rate with a C/20 trickle. Red lines (in (a)) indicate the growing Li$_{15}$Si$_4$ delithiation region. Roman numerals indicate points where cells were disassembled for SEM imaging. I to IV are the resulting SEM images.

After the first cycle (Figure 3.5 I), there was widespread cracking and trench formation, resulting in the formation of Si islands; however, the film had not disconnected

from the substrate and no $Li_{15}Si_4$ could be detected in the voltage curve. After cycle 2 (Figure 3.5 II), some of the edges of the Si islands had disconnected from the substrate and a small amount of $Li_{15}Si_4$ could be detected in the voltage curve. After cycle 3 (Figure 3.5 III), there was significant delamination of the film from the substrate. This delamination was coincident with significant $Li_{15}Si_4$ capacity in the voltage curve. After cycle 5 (Figure 3.5 IV), Si islands were only attached to the substrate by small point contacts and most of them were so weakly bound that they detach entirely upon cell disassembly. Coincidentally, the $Li_{15}Si_4$ plateau began to account for nearly the entire delithiation capacity for this cycle.

3.3.3 Effect of delamination and polarization on $Li_{15}Si_4$ formation

These results strongly imply a relationship between film delamination and increased $Li_{15}Si_4$ formation. To confirm this relationship, a portion of a 400 nm Si film (pro. #2, Table 2.1) sputtered on E-Cu^R was cycled (C/20 rate with a C/40 trickle) as is, while the Si from another portion of the electrode was removed from its substrate by dissolving the Cu substrate in nitric acid. The recovered Si flakes were then incorporated into a composite coating. Figure 3.6 shows the differential capacity curve of the first cycle of the composite coating and that of the original Si film attached to the E-Cu^R substrate. There is significant $Li_{15}Si_4$ formation in the Si film with no substrate. In contrast, the original Si film attached to the Cu foil shows no sign of $Li_{15}Si_4$ formation. In addition, the peak at about 0.08 V during lithiation is at a much lower potential for the Si film bonded to the E-Cu^R substrate, than the Si film with no substrate. This shift is consistent with voltage depression caused by compressive stress. The results shown in Figures 3.4, 3.5, and 3.6 imply that the suppression of $Li_{15}Si_4$ formation in sputtered films is entirely due to

effects from the substrate and that $Li_{15}Si_4$ formation and fade are direct results of Si film delamination. This explains why 2 µm thick Si films sputtered on substrates were reported not to form $Li_{15}Si_4$ during cycling, while $Li_{15}Si_4$ forms during the cycling of much smaller Si particles (even nanoparticles).
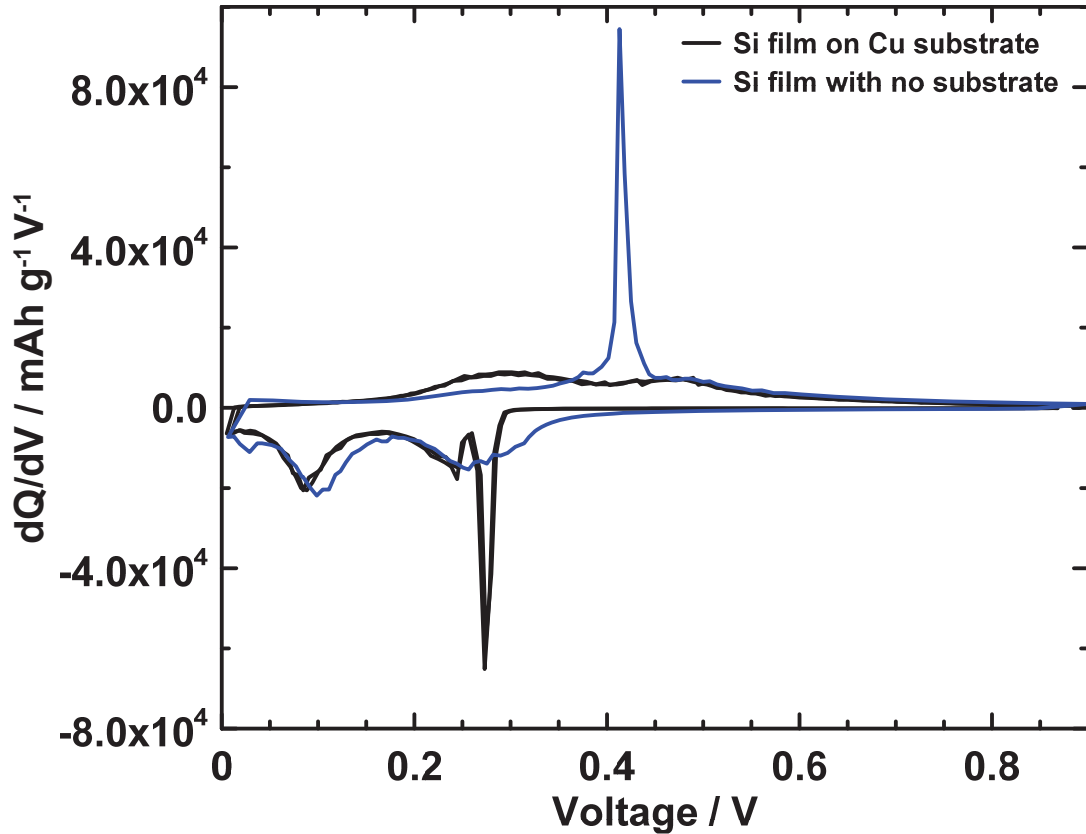
Figure 3.6. Differential capacity curve for the first cycle of a 400 nm Si film sputtered onto E-Cu^R (in black) and one of a Si composite coating where the Si was obtained by dissolving the Cu substrate of a Si thin film in HNO_3 and recovering the Si flakes.

Polarization may provide an alternate explanation of $Li_{15}Si_4$ suppression in thin films. For a pristine film, the surface area is small, diffusion only occurs from one side of the film. This may cause increased polarization, compared to a Si particle or delaminated flake, which might shift the voltage curve, leading to a suppression of $Li_{15}Si_4$. As the film cracks during cycling, surface area increases, leading to improved kinetics, less

polarization, and hence more $Li_{15}Si_4$ formation. To see if this is the case, a 275 nm film (pro. #3, Table 2.1) deposited onto E-Cu was cycled at slow rates (C/50 and C/75).
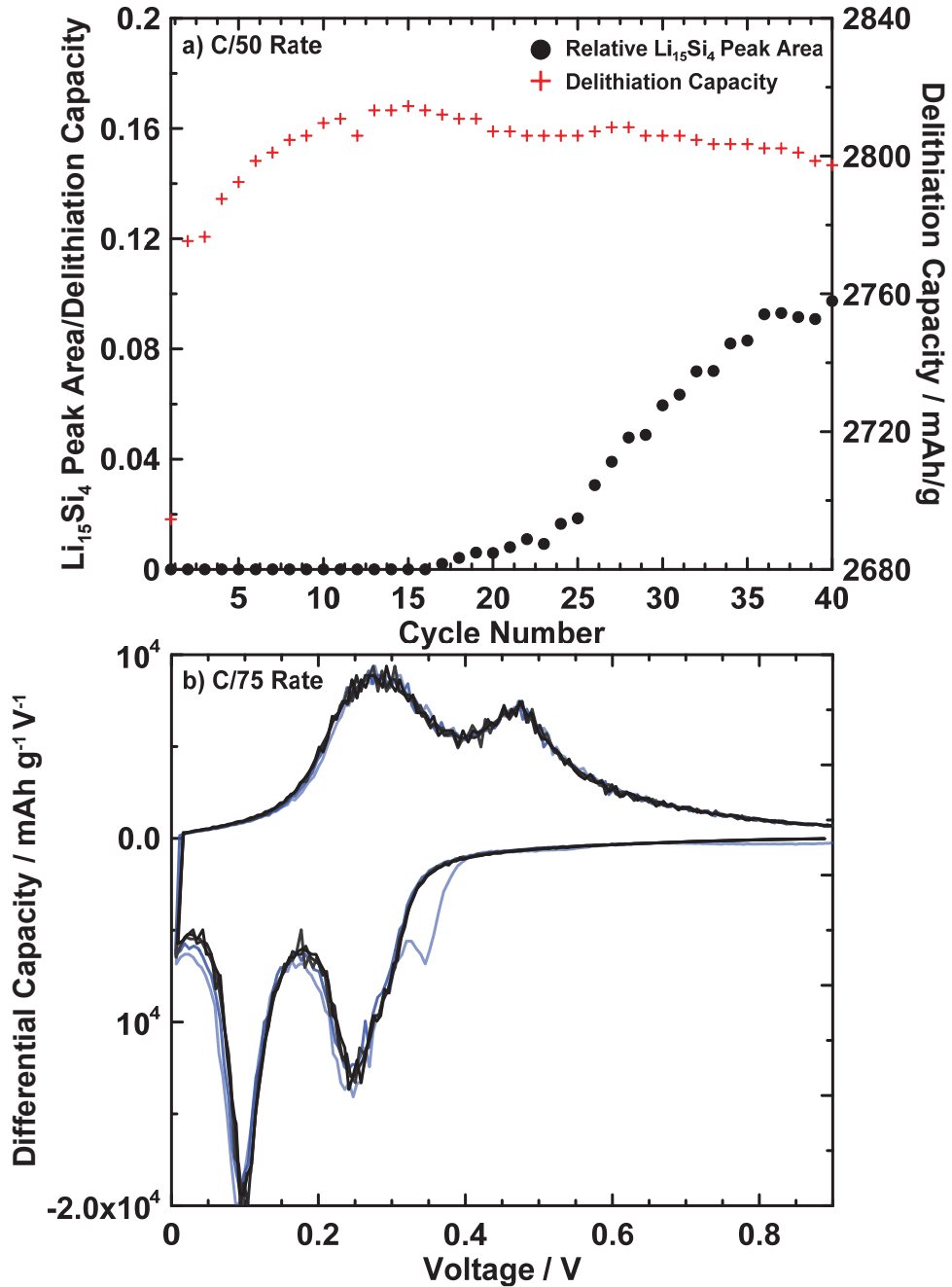
Figure 3.7. Relative $Li_{15}Si_4$ peak area and delithiation capacity versus cycle number for a 275 nm film sputtered onto E-Cu cycling at C/50 rate in (a). Differential capacity curve of the first 5 cycles of the same film at C/75 rate, darker lines indicate later cycles.

Figure 3.7 investigates the role slower rates plays on $Li_{15}Si_4$ formation. In Figure 3.7 (a), the delithiation capacity and $Li_{15}Si_4$ peak area versus cycle number is provided for a 275 nm film sputtered onto E-Cu cycling at C/50. At this slow rate, $Li_{15}Si_4$ formation remains suppressed during early cycling and only emerges by cycle 17. Additionally, $Li_{15}Si_4$ formation is accompanied by capacity fade. Figure 3.7 (b) shows the differential capacity curves for the first five electrochemical cycles of the same film cycling at C/75 rate. No $Li_{15}Si_4$ emerges after the first 5 cycles. Cells at this rate failed after five or less cycles, so no extended cycling performance could be obtained. Overall, even at rates as slow as C/50 or C/75, $Li_{15}Si_4$ formation is suppressed in early cycling. This result implies that polarization may not play a large role in the suppression of $Li_{15}Si_4$.

Even at the low rates examined, cells do not spend much time below 50 mV during cycling. For instance, cells spend about 4 and 6 hours below 50 mV at C/50 and C/75, respectively. Therefore, even low levels of polarization could result in incomplete $Li_{15}Si_4$ formation. To investigate this, a 275 nm film (pro. #3, Table 2.1) deposited onto E-Cu was cycled at C/2 rate with a C/20 trickle for two cycles, then discharged to 5 mV and held at this voltage for 100 hours. Afterwards, the cell continued cycling using the regular cycling conditions (C/2 with a C/20 trickle).

Figure 3.8 compares the electrochemical behaviour of a 275 nm Si film (pro. #3, Table 2.1) cycled using the standard protocol (C/2 with a C/20 trickle) to that of one with a 100 hour hold at 5 mV after the 3rd discharge. Figure 3.8 (a) shows the delithiation capacity and relative $Li_{15}Si_4$ peak area for the film that underwent standard cycling conditions. Figure 3.8 (b) shows the differential capacity of a film that was held at 5 mV for 100 hours after the 3rd discharge. In Figure 3.8 (a), the film sputtered onto E-Cu exhibits

38

no $Li_{15}Si_4$ formation until cycle 18, with coincident capacity fade (similar to Figure 3.4).

Before the 100 hour hold in Figure 3.8 (b), no $Li_{15}Si_4$ is formed, but after the hold, a significant amount of $Li_{15}Si_4$ forms. This result could be due to the elimination of polarization effects during the hold. Alternatively, the film may have undergone plastic flow when held at 5 mV, which could reduce the stress between the film and substrate. Both factors could also be contributing to $Li_{15}Si_4$ formation in the film.

Figure 3.8. Relative $Li_{15}Si_4$ peak area and delithiation capacity vs. cycle number for a 275 nm Si film (pro. #3, Table 2.1) sputtered onto E-Cu in (a). (b) is the differential capacity curve for the same film in (a) when held at 5 mV for 100 hours on the 3rd discharge, and (c) provides the differential capacity curves for the first cycle following the 100 hour hold and cycle 30 of the cell in (a).

Figure 3.8 compares the electrochemical behaviour of a 275 nm Si film (pro. #3, Table 2.1) cycled using the standard protocol (C/2 with a C/20 trickle) to that of one with a 100 hour hold at 5 mV after the 3rd discharge. Figure 3.8 (a) shows the delithiation capacity and relative $Li_{15}Si_4$ peak area for the film that underwent standard cycling conditions. Figure 3.8 (b) shows the differential capacity of a film that was held at 5 mV for 100 hours after the 3rd discharge. In Figure 3.8 (a), the film sputtered onto E-Cu exhibits no $Li_{15}Si_4$ formation until cycle 18, with coincident capacity fade (similar to Figure 3.4). Before the 100 hour hold in Figure 3.8 (b), no $Li_{15}Si_4$ is formed, but after the hold, a significant amount of $Li_{15}Si_4$ forms. This result could be due to the elimination of polarization effects during the hold. Alternatively, the film may have undergone plastic flow when held at 5 mV, which could reduce the stress between the film and substrate. Both factors could also be contributing to $Li_{15}Si_4$ formation in the film.

Electrochemical cycles following the hold, using the standard cycling protocol, (shown in Figure 3.8 (b)) exhibited an incremental increase in $Li_{15}Si_4$ formation, whereas the film cycled without the hold did not form $Li_{15}Si_4$ at these low cycle numbers. Therefore, the formation of $Li_{15}Si_4$ during the hold has induced $Li_{15}Si_4$ formation in subsequent cycling. It is possible that $Li_{15}Si_4$ crystallization has introduced grain boundaries, which, in turn caused crack formation to propagate during delithiation, leading to delamination.

Lastly, Figure 3.8 (c) compares the differential capacity curve of the first electrochemical cycle following a 100 hour hold at 5 mV to that of the 30th cycle of the cell with no holds. The $Li_{15}Si_4$ delithiation capacity was significantly smaller and capacity from amorphous delithiation (between 0.25 and 0.40 V) was significantly larger after the 100 hour hold than that of the film on its 30th cycle. Therefore, there was still incomplete $Li_{15}Si_4$

formation in the film after the 100 hour 5 mV hold. It is difficult to believe that this was due to polarization effects. Ultimately, due to the absence of complete $Li_{15}Si_4$ formation even after the 100 hour hold, the induced formation of $Li_{15}Si_4$ in cycles following the hold, complete $Li_{15}Si_4$ suppression in films cycled at very slow C-rates, and previous studies showing that stress-voltage coupling in Si thin films can result in a shift of up to 200 mV in the voltage profile,[58] film/substrate stress is likely the major cause behind $Li_{15}Si_4$ suppression in Si thin films.

3.3.4 Disconnection model for $Li_{15}Si_4$ formation in Si thin films

Assuming stress is the primary factor causing $Li_{15}Si_4$ suppression during cycling, a model can be made to explain the SEM and electrochemical behaviour observed during the cycling of a Si thin film bonded to a substrate, as illustrated in Figure 3.9. When the pristine Si film (I) is first lithiated it can only expand in a direction perpendicular to the substrate. This causes large compressive stresses to form and the film undergoes plastic flow, increasing its thickness (II). Because of the large stresses that occur during this process, the voltage is depressed, by up to ~200 mV.[58,59] This causes the $Li_{15}Si_4$ formation voltage to be shifted below 0 V, and therefore this phase does not form at full lithiation. During delithiation, the film begins to contract. Large tensile stresses develop, causing the voltage to be elevated above the equilibrium voltage. Some of the tensile stress can be alleviated by crack formation, as shown in (III). Initially, as observed in Figure 3.5, the film remains bonded to the substrate and the cracks are in the form of trenches. During subsequent lithiations, the film expands, undergoing compressive stress and plastic flow. This expansion causes the cracks to close and the film to expand in thickness again (IV). Because the film is under compressive stress, $Li_{15}Si_4$ does not form, as explained above.

41

These observations of Si film expansion and crack propagation have been observed previously.[61] After repetitive cycling, the Si thin film eventually begins to detach from the substrate (V). The detached regions now experience much less stress during lithiation, and, as a result, the voltage curve of Si in these regions is affected less by stress effects. Therefore, in these regions $Li_{15}Si_4$ forms at full lithiation (VI). During repeated cycling, the film becomes increasingly detached and more $Li_{15}Si_4$ forms at full lithiation. Eventually, Si islands detach entirely (VII). These islands likely then become completely surrounded by the solid electrolyte interphase and become electronically isolated (VIII), resulting in capacity fade.
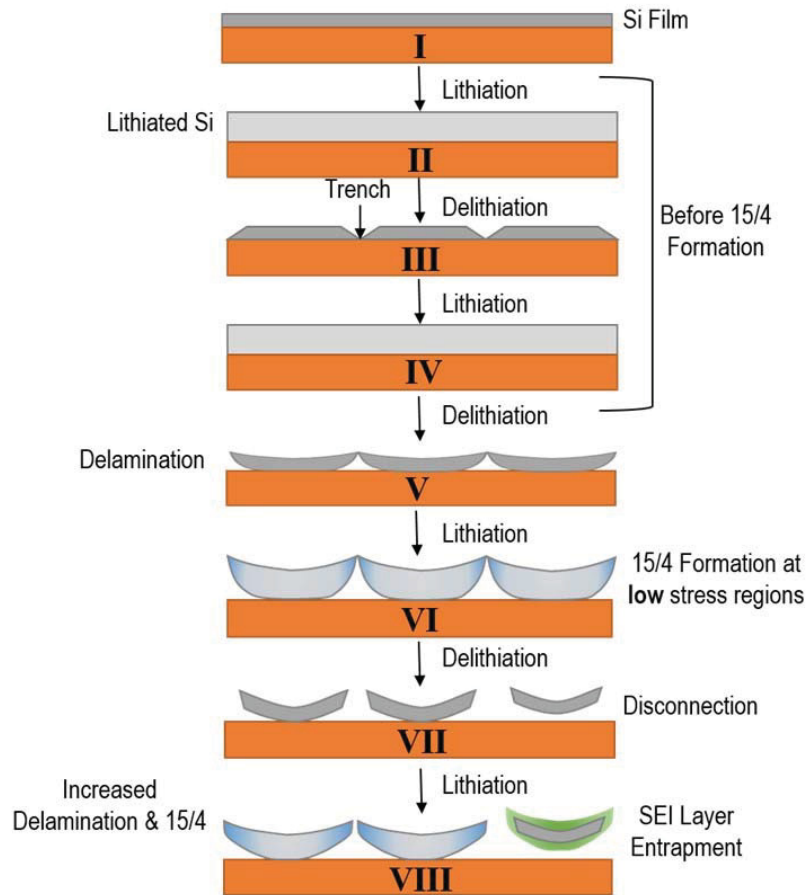
Figure 3.9. Illustration of the processes that occur during the cycling of a Si thin film, resulting in $Li_{15}Si_4$ formation, disconnection, and fade.

42

3.3.5 Effect of substrate identity on cycling performance and $Li_{15}Si_4$

The model proposed in Figure 3.9 implies that using different substrates that have different adhesion to the Si film may significantly affect electrochemical performance. To test this theory, a 275 nm film of Si was simultaneously sputtered onto various substrates, so that the sputtering conditions were identical for each substrate. Figure 3.10 shows the cycling performance of the resulting thin film electrodes.
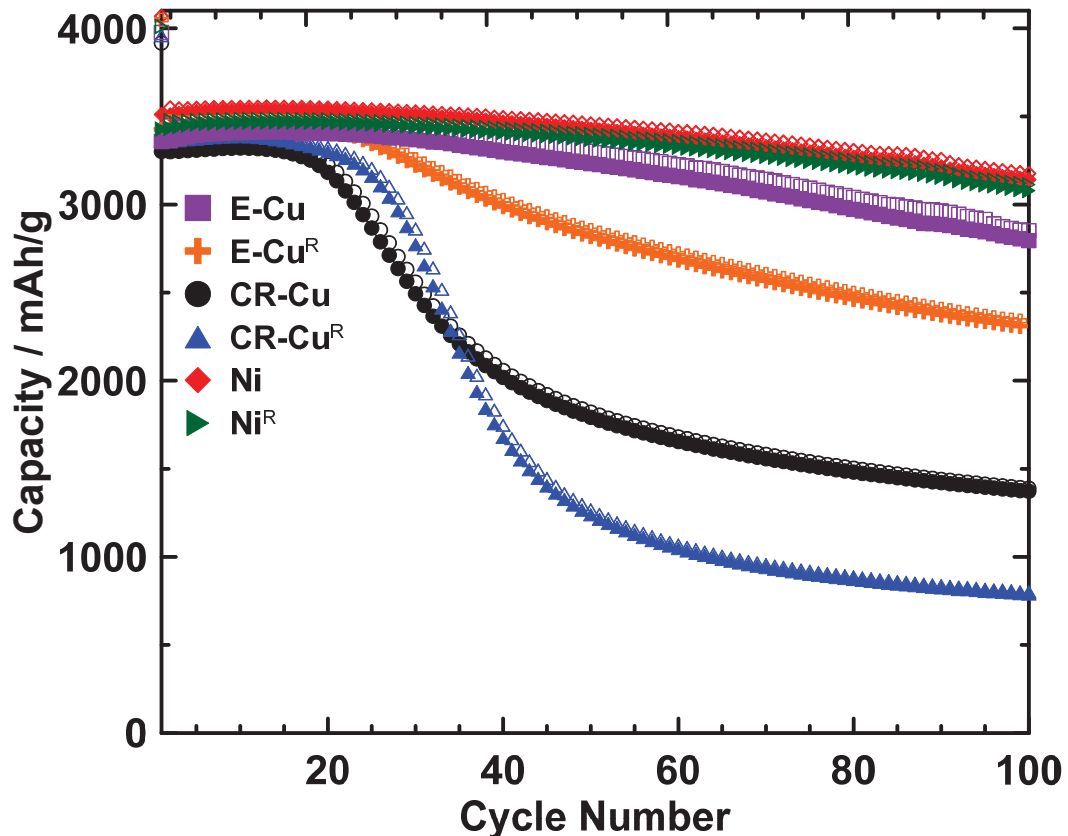
Figure 3.10. Cycling performance of a 275 nm Si thin film on different substrates. Open and closed symbols represent the lithiation and delithiation capacity, respectively.

It can be seen that both substrate composition and surface morphology significantly affected the cycle life of a Si thin film. These effects can be rationalized in terms of the model proposed in Figure 3.9. For instance, Si sputtered onto CR-Cu[R] had the worst cycling performance. Since the cold rolling process utilizes lubricants, one might expect that any

lubricating oil layer on the Cu foil would cause the Si film adhesion to be poor, resulting in capacity fade. Roughening the Cu foil also resulted in fade, likely due to the Si film becoming detached at high radii of curvature apexes. It is well known that Si bonds strongly to Ni,[62] and, as a result, Ni is used as a bonding layer for Si wafer contacts in solar cells.[63,64] Good Si-Ni adhesion likely results in good cycling performance of the Si film on Ni foil, even when it is roughened.

Figure 3.11 shows the delithiation capacity, $Li_{15}Si_4$ peak area, and the change in average half-cycle potential (from the first cycle) plotted against cycle number for all the Si films on the different substrates shown in Figure 3.10. All films exhibited fade commencing after about 15 - 20 cycles, although the fade was more severe for some films than others. $Li_{15}Si_4$ formation was coincidental with fade in all cases. These results are consistent with the model proposed in Figure 3.9. However, cells that experienced larger capacity fade were not found to exhibit greater $Li_{15}Si_4$ formation as a fraction of total delithiation capacity. Instead, the films expected to have the best adhesion to Si (Ni, Ni^R, and E-Cu) cycled with a low fade rate despite the formation of $Li_{15}Si_4$. It is suspected that the Si islands in these films that form after crack formation remain attached to the substrate by means of a small "patch" (as reported in Reference 65), which maintains electrical contact. Most of the area of such islands may be separated from the substrate and subject to low stress; therefore, they formed considerable amounts of $Li_{15}Si_4$ at full delithiation. However, such islands could continue to cycle by virtue of their maintained electrical contact. In films on substrates with less adhesion, the ability to maintain electrical connection to the substrate via a small patch was reduced, and flake detachment and fade were accelerated.

44
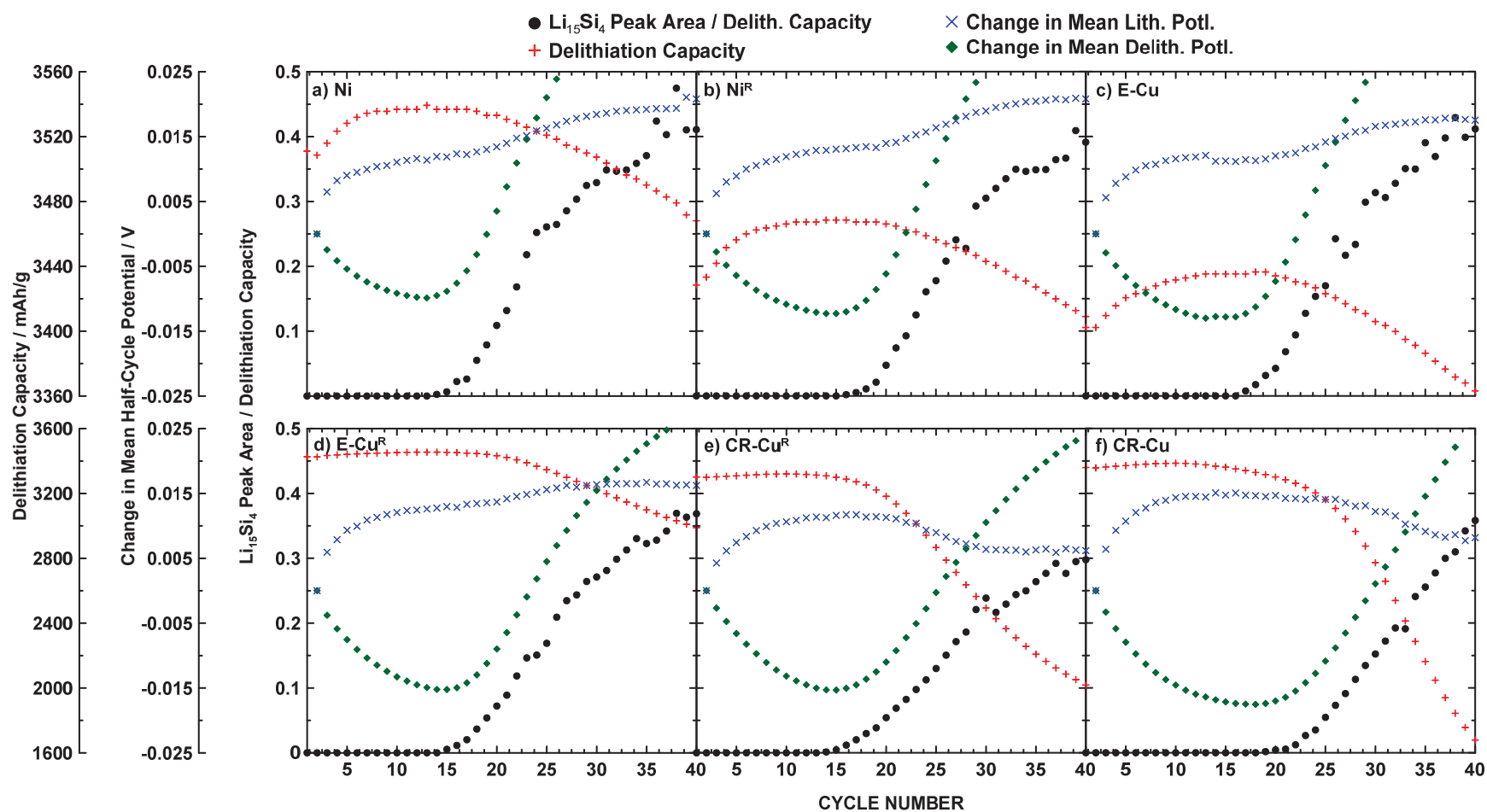
Figure 3.11. Delithiation capacity, relative $Li_{15}Si_4$ peak area, and change in mean half-cycle potential versus cycle number, for a 275 nm Si thin film sputtered onto substrates Ni, Ni^R, E-Cu, $E-Cu^R$, $CR-Cu^R$, and CR-Cu foil.

The average half-cycle potential, also shown in Figure 3.11, provides further insight into the relationship between stress, $Li_{15}Si_4$ formation and capacity fade. For all films, the average delithiation potential decreased during initial cycles. This indicates that the tensile stress in the film becomes reduced every cycle, perhaps due to progressive crack formation. When fade and $Li_{15}Si_4$ formation started to occur the average delithiation voltage increased sharply. This was an artifact of the growth of the $Li_{15}Si_4$ peak at about 440 mV. During lithiation, the average voltage initially increased. This indicates that the compressive stress in the film becomes reduced every cycle, again likely due to progressive crack formation. The average lithiation voltage then reached a plateau, until fade and $Li_{15}Si_4$ formation occurred. This was also where film detachment from the substrate commences, which should further reduce compressive stresses during lithiation. Indeed this was reflected by an increase in average lithiation voltage at the same moment when fade and $Li_{15}Si_4$ formation started, further reinforcing the disconnection model. During fade the average lithiation voltage increased to a plateau, except for the CR-Cu and CR-Cu^R foils. In these foils the average lithiation voltage decreased in later cycles, however this decrease in voltage was due to polarization. In these foils, the fade was so severe that during later cycles the capacity was small, resulting in a significant increase in cycling rate and the resulting polarization caused the lithiation voltage to decrease as observed.

To further understand the mechanism behind stress alleviation in Si thin films, the nature of the voltage shift needs to be clarified. For instance, stress could be reduced uniformly in the film, which would result in a uniform shift in differential capacity peaks. Alternatively, the stress could be relieved in an inhomogeneous manner, in which case one would expect the differential capacity peaks to both shift and become broadened as cycling

progresses. In Figure 3.12, the full width at half maximum (FWHM) of cycles 2, 5, and 25 are plotted for the electrodes used in Figure 3.10. The FWHM did not change appreciably during cycling. This suggests that stress was uniformly relieved in the Si film during cycling.
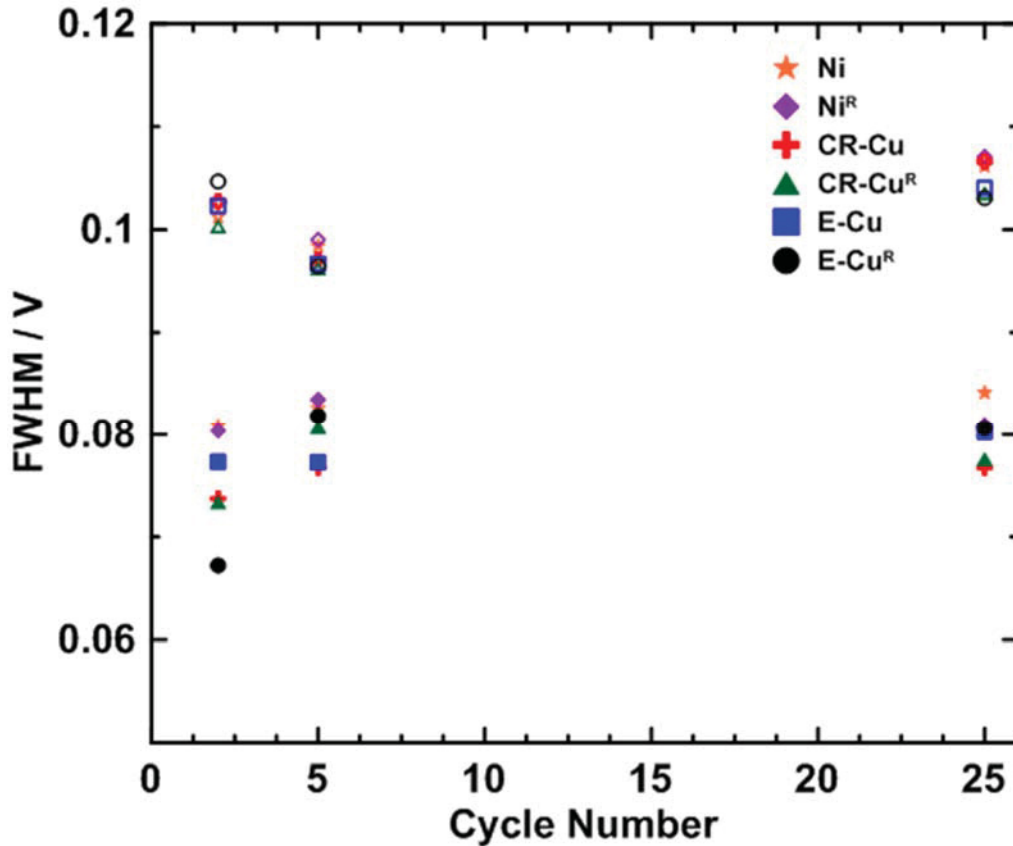
Figure 3.12. Full width at half maximum (FWHM) of the lithiation peaks in the differential capacity curve for cycles 2, 5 and 25 for the cells examined in Figure 3.10. The open and closed points represent the 200 and 90 mV lithiation peak positions, respectively.

3.3.6. The role of Li$_{15}$Si$_4$ on cycling performance

So far in this study, the appearance of Li$_{15}$Si$_4$ has only been shown to be indicative of film disconnection from the substrate. A question remains as to whether the presence of Li$_{15}$Si$_4$ is detrimental to cycling. To determine this, 275 nm Si films sputtered onto CR-Cu and onto E-Cu were cycled to lower cutoff voltages of 5 mV (where Li$_{15}$Si$_4$ formation eventually occurs) and 25 mV (at which it was found Li$_{15}$Si$_4$ formation was avoided for

this film). Cycling performance of these cells and their differential capacity are shown in Figures 3.13 and 3.14 for the CR-Cu and E-Cu foil substrates, respectively. In the case of the Si film on CR-Cu, fade occurred at about cycle 20 when $Li_{15}Si_4$ is formed. In contrast, fade commenced at about cycle 50 when the lower voltage cutoff was raised to avoid $Li_{15}Si_4$ formation. It is difficult to believe that this significant difference in cycling performance is a result of the slightly greater cycled capacity for the film cycled to 5 mV. Instead, this is suggestive that $Li_{15}Si_4$ formation is detrimental to cycling. This has long been suspected to be the case, since 2-phase regions are thought to be detrimental to cycling.[7,66] This distinction was less clear for the film sputtered on E-Cu, shown in Figure 3.14. However, in this film there was a large reduction in capacity when the voltage was limited, which may have affected cycling results by improving cycling (less volume expansion).
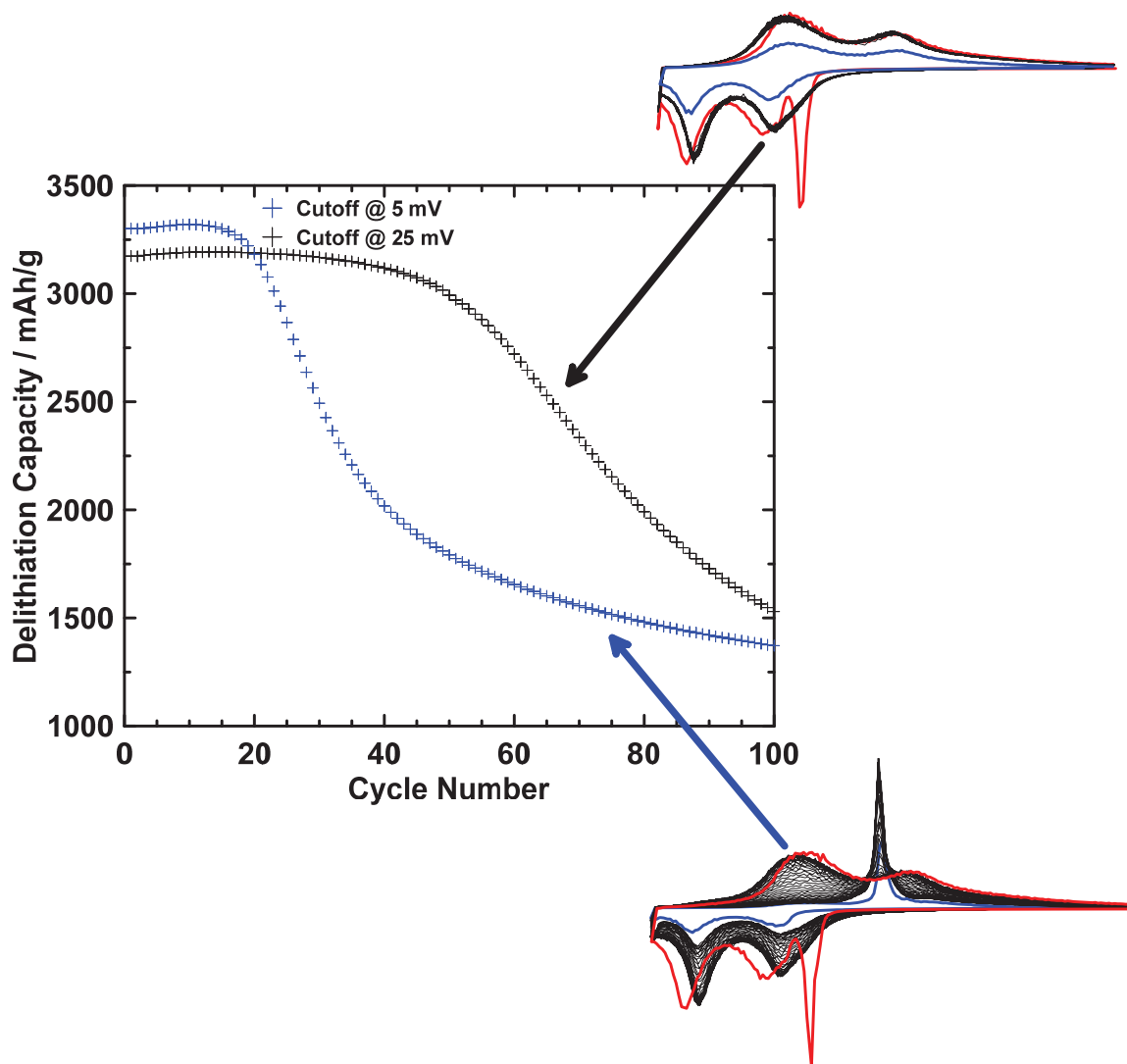
Figure 3.13. Delithiation capacity versus cycle number for a 275 nm thick Si film sputtered onto CR-Cu cells with lower voltage cutoffs of 25 and 5 mV. Insets show the differential capacity curve for each cell where the first cycle is in red, cycles 10-50 are in black, and cycle 100 is in blue.
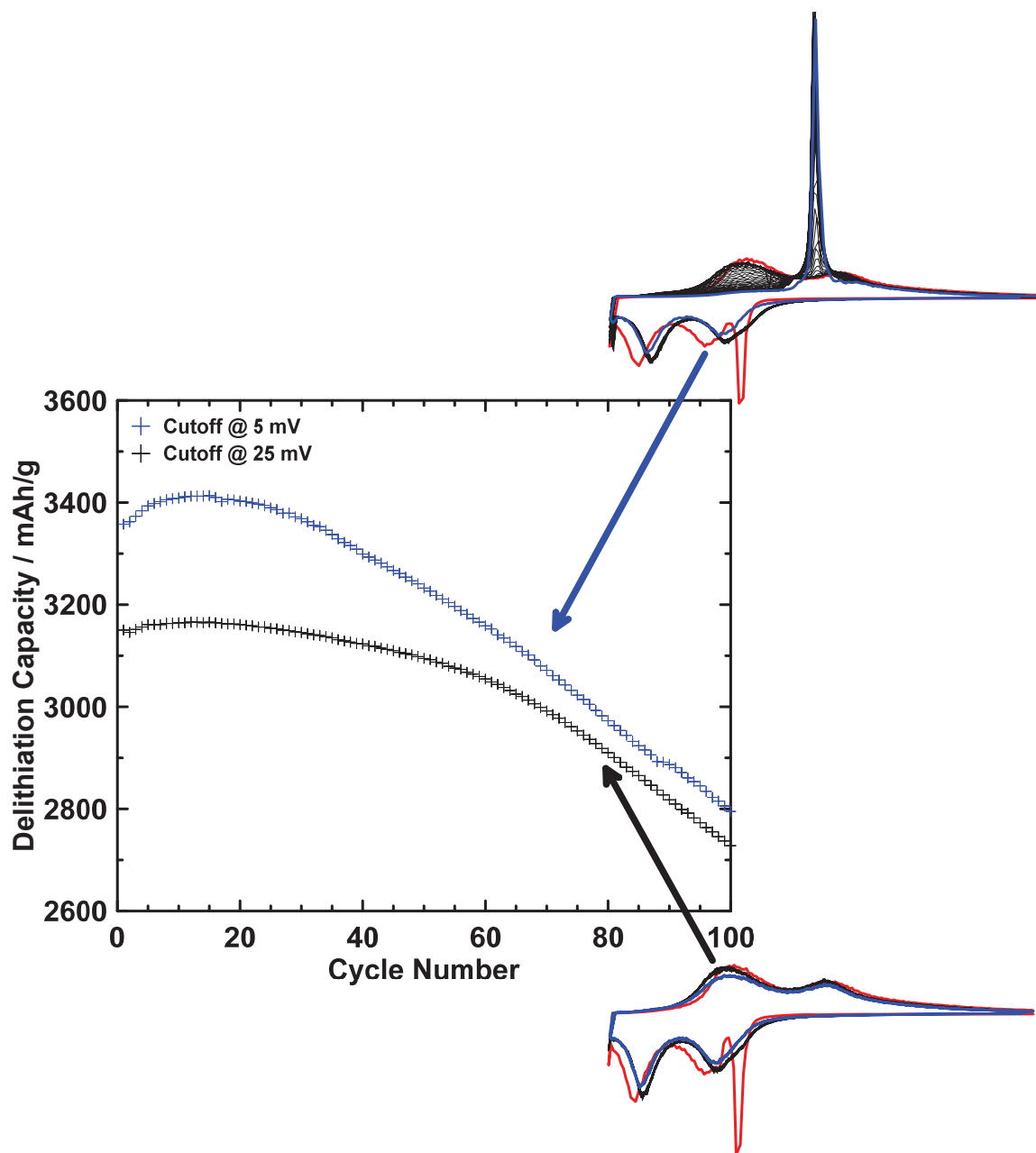
Figure 3.14. Delithiation capacity versus cycle number for a 275 nm thick Si film sputtered onto E-Cu cells with lower voltage cutoffs of 25 and 5 mV. Insets show the differential capacity curve for each cell where the first cycle is in red, cycles 10-50 are in black, and cycle 100 is in blue.

To further test the effect of $Li_{15}Si_4$ formation on electrochemical performance, the cycling performance of the cell held at 5 mV for 100 hours (Figure 3.8) was examined in cycles following the hold, as shown in Figure 3.15. In this cell, $Li_{15}Si_4$ formation was induced after the second cycle through the 100 hour hold, causing it to gradually form in

subsequent cycles. It can be seen that even though the same electrodes were being cycled, the one with induced $Li_{15}Si_4$ formation begins fading immediately, while the electrode without a hold, and therefore without $Li_{15}Si_4$ formation, experienced almost no capacity fade (until about cycle 40). These results strongly suggest that $Li_{15}Si_4$ formation is harmful to electrochemical performance.
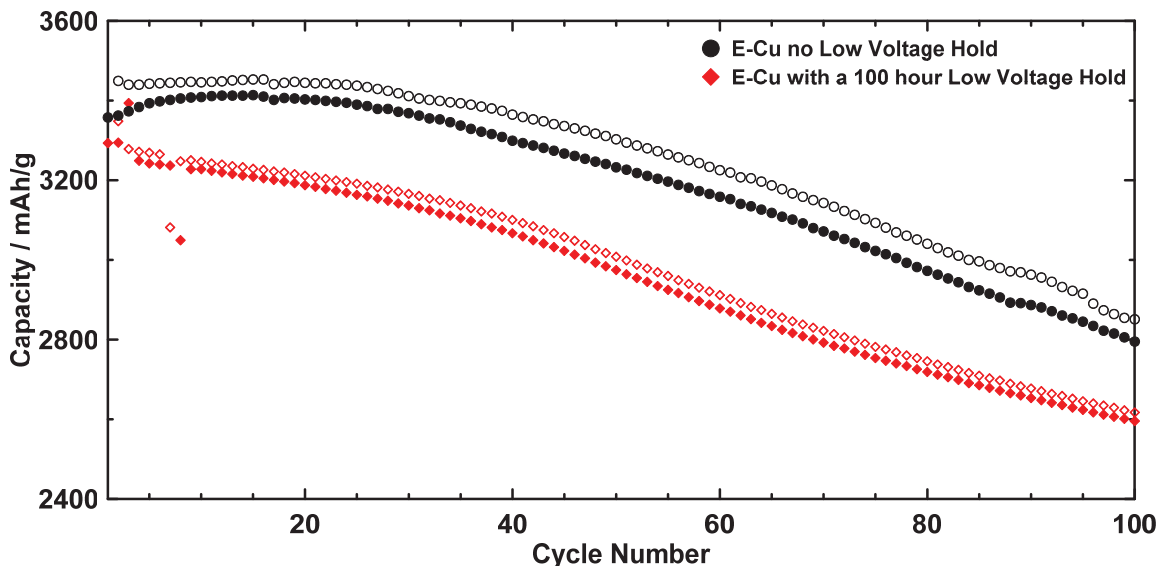
Figure 3.15. Cycling performance of a 275 nm Si film (pro. #3, Table 2.1) sputtered onto E-Cu for one cell with and one without a 100 hour hold at 5 mV following the 3rd discharge. Open and closed symbols represent the lithiation and delithiation capacity, respectively.

3.4 Conclusions

In this work, the mechanism of fade and $Li_{15}Si_4$ formation in Si thin films were examined. In contrast to past studies, $Li_{15}Si_4$ formation occurred in all films during cycling. It is likely that previous studies terminated cycling prematurely, before $Li_{15}Si_4$ formation occurred. In all cases, $Li_{15}Si_4$ formation was found to be closely correlated with capacity fade and film detachment from the substrate. Slow rate electrochemical cycling tests also showed $Li_{15}Si_4$ suppression, indicating that polarization in the film is likely not its major

cause. $Li_{15}Si_4$ also forms immediately when the Si thin film is removed from the substrate and is cycled in a composite coating. These observations strongly suggest that $Li_{15}Si_4$ suppression in thin films is due to stress induced from the presence of the substrate. As cycling progresses, the film progressively detaches from the substrate, resulting in fade and progressive $Li_{15}Si_4$ formation. These results were further confirmed by measurements of average half-cycle voltages, which were consistent with stress release during cycling and film detachment from the substrate. Lastly, results suggested that $Li_{15}Si_4$ formation itself may have a detrimental effect on cycling, as has long been suspected.

These results suggest that the formation of $Li_{15}Si_4$ can be used as a sensitive indicator for Si regions that are weakly bound or disconnected from a substrate. If a peak from $Li_{15}Si_4$ is present in differential capacity during cycling to full lithiation, then the Si must be weakly bound to a substrate. If no $Li_{15}Si_4$ peaks are present in the differential capacity curve, the Si must be strongly connected to a substrate. However, care must be taken when using this property that cells are cycled at a low rate, since high rate cycling can cause cell polarization, resulting in the suppression of $Li_{15}Si_4$ formation.[55]

These results have profound implications, not only for thin films, but also for Si alloys in general (including Si alloy particles). For instance in particles comprising an active Si phase and an inactive matrix phase, the presence of the inactive phase should induce stress during the expansion/contraction of the active Si phase and suppress $Li_{15}Si_4$ formation, just as the substrate does in a Si thin film. This has been found to be exactly the case, as is demonstrated in Reference 67.

Chapter 4 Electrode Cycling and Li$_{15}$Si$_4$ Formation

4.1 Introduction and Background

Alloys expand significantly upon lithiation, and, because of this, keeping them electrically connected in a composite coating during delithiation is a difficult task. Figure 1.6, for instance, plots the poor electrochemical performance of a PVDF containing Si coating. Unlike modern binders for alloys, PVDF, which has not been heat-treated,[68] does not effectively cover the entire electrode surface or form bonds with the active material,[69,70] but instead forms thin threads throughout the sample.[71] The effectiveness of electrode coatings with different binders can be visualized in Figure 4.1. Here, Li et al. used an alloy negative electrode, Sn$_{30}$Co$_{30}$C$_{40}$, to test three well-known binders.[72] As binder identity changes from LiPAA, to CMC, to PVDF cycling performance dramatically worsens.
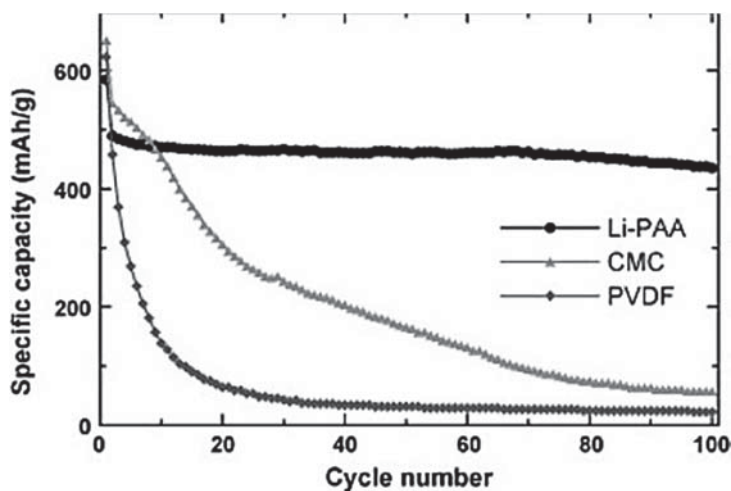
Figure 4.1. Specific capacity versus cycle number for coin cells having Sn$_{30}$Co$_{30}$C$_{40}$ electrodes using LiPAA, CMC and PVDF binders. The electrolyte here was 1 M LiPF$_6$ in a mixed solution of EC and DEC (volume ratio = 1:2) with FEC added at 10 % by wt. to the electrolyte solvent. Cells were charged and discharged between 0.005 and 1.2 V at C/10 rate. Reproduced with permission from Reference 72. Copyright 2010 Elsevier.

Impedance, imaging, and electrochemical cycling studies performed by Komaba et al. allowed the authors to propose an electrode model explaining the improved cyclability resulting from the implementation of certain polymeric binders.[69] Figure 4.2 illustrates the behaviour of PVDF and LiPAA during cycling. The non-uniform binding and swelling of PVDF upon submersion in electrolyte weakens the binder and increases electrolyte decomposition, resulting in early loss of electrical contact. Binders with surface functionality that can bond to Si, like LiPAA, uniformly coat the Si alloy surfaces, lessening electrolyte decomposition, while providing resistance against electrode expansion, effectively enhancing reversibility.[69]
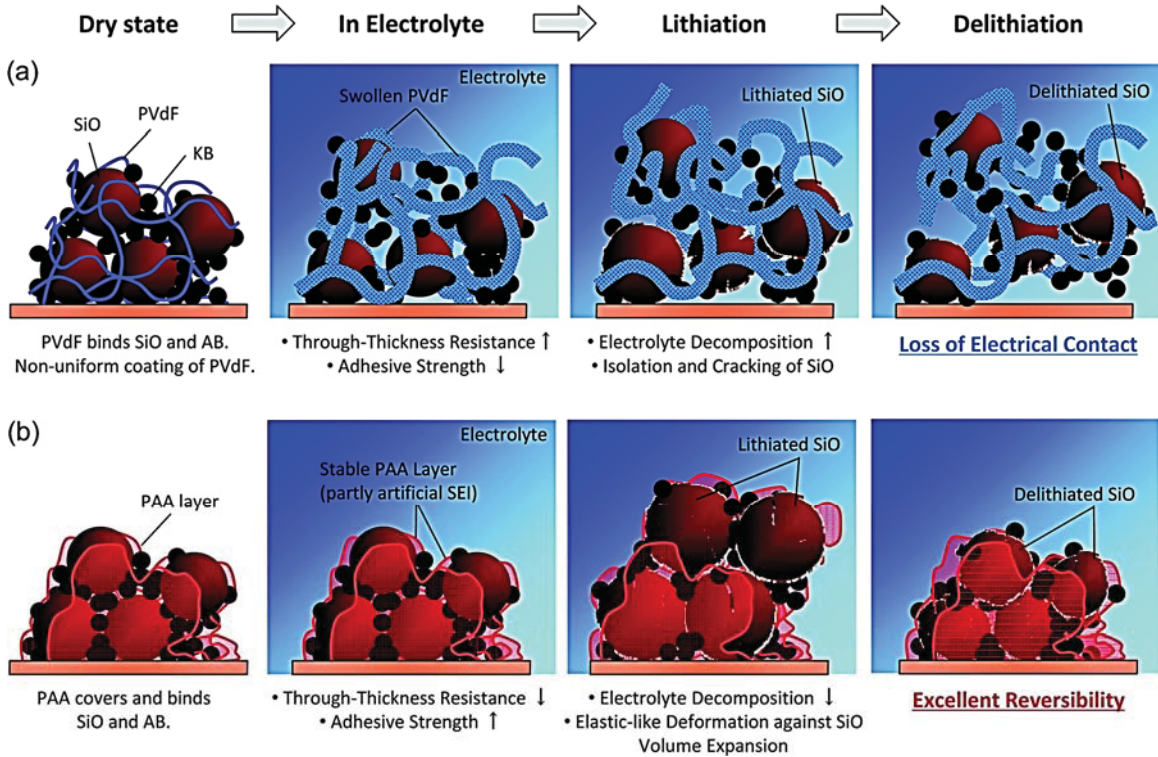
Figure 4.2. Schematic illustrations of the proposed mechanism for the improved cyclability for the SiO powder composite electrodes; (a) PVDF and (b) PAA binders. Reprinted with permission from Reference 69. Copyright 2011 American Chemican Society.

Overall, binders have a significant impact on electrochemical behaviour of electrode coatings and their cycling performance. Combining this importance with the

results concerning $Li_{15}Si_4$ formation in Chapter 3, it is reasonable to hypothesize that binder identity could influence the magnitude and/or rate of $Li_{15}Si_4$ formation. Furthermore, unlike cycling performance data, which is dependent on numerous factors (e.g. electrolyte, coating formulation, amount of conductive additive), $Li_{15}Si_4$ suppression can be directly related to the level of stress Si is under and, by extension, how well connected Si is in the electrode coating.

Work from Sethuraman et al. (shown in Figure 3.1) suggests that a 50 mV voltage shift, i.e. one capable of suppressing $Li_{15}Si_4$ formation, requires ~500 MPa of applied compressive stress.[58] The ultimate tensile strength of the binders PI, PAA, and PVDF are ~230 MPa,[73] ~160 kPa,[74] and ~50 MPa,[75] respectively, therefore stiff binders like PI can potentially induce a voltage shift that is capable of suppressing $Li_{15}Si_4$ formation. Furthermore, $Li_{15}Si_4$ formation can be entirely suppressed by using nanoparticles,[55,76,77] therefore the amount of stress needed to suppress $Li_{15}Si_4$ formation should be reduced as the Si grain size becomes small. Hence, it is plausible that polymer binders might suppress $Li_{15}Si_4$ formation, especially in the case of n-Si.

Additionally, conventional electrode coatings are composed of particles that are in contact with each other. During lithiation, particle-particle contacts could be areas of high stress, especially if the coating is firmly bonded to the substrate. It has been shown that, despite their porosity, alloy coatings are nearly incompressible and can require close to 300 MPa to lower coating porosity by 12 %.[13] Therefore, particle expansion can likely induce significant compressive stress at particle-particle contacts during lithiation. Combining these factors, the stress induced by the polymer binder and particle-particle interactions may suppress $Li_{15}Si_4$ to some extent. This phenomenon is investigated in this chapter.

Ultimately, $Li_{15}Si_4$ has the potential to be an ideal probe when assessing electrode coating quality.

4.2 Coating Optimization with Bulk Silicon

Coating performance was first tested using bulk Si powder (-325 mesh) as the active material. To test $Li_{15}Si_4$ formation in coatings requires that a Si-based coating formulation be developed with good cycling performance. To obtain optimal cycling performance, numerous coating formulations were prepared, detailed in Section 2.5, and electrochemically tested. Unpublished work from Wilkes et al. suggests that polyimide (PI) binder exhibits superior performance when implemented into alloy negative electrodes.[78] Therefore, this binder was used when optimizing the Si-based coating formulation. The formulae in this section will always be expressed as Si/SC/Binder in a volumetric ratio. Volumetric ratios are used instead of mass ratios so that a theoretical surface coverage thickness (in nm) of the binder on the active material (Si) and SC can be determined.

Figure 4.3 presents the cycling performance of five formulations where the active material ratio ranges from 70 to 50 volume percent and the amount of SC carbon black was held constant at 20 % by volume. At higher Si ratios (e.g. 70 and 65 %), there was swift capacity fade, possibly because there was not enough binder to sufficiently coat and adhere the active material. The best performing ratios appear to have a 50 to 60 volume percent of active material; however, a slight decrease in capacity was seen when changing from a 55/20/25 to a 50/20/30 coating formulation. This drop may be due to partial electrical isolation of active particles resulting from the thicker binder film, or may be due to weighing error. Ultimately, since bulk Si exhibits large amounts of $Li_{15}Si_4$ formation

56

regardless of formulation, the optimal coating formula was chosen based on cycling performance, and in this case, the 55/20/25 coating was chosen.
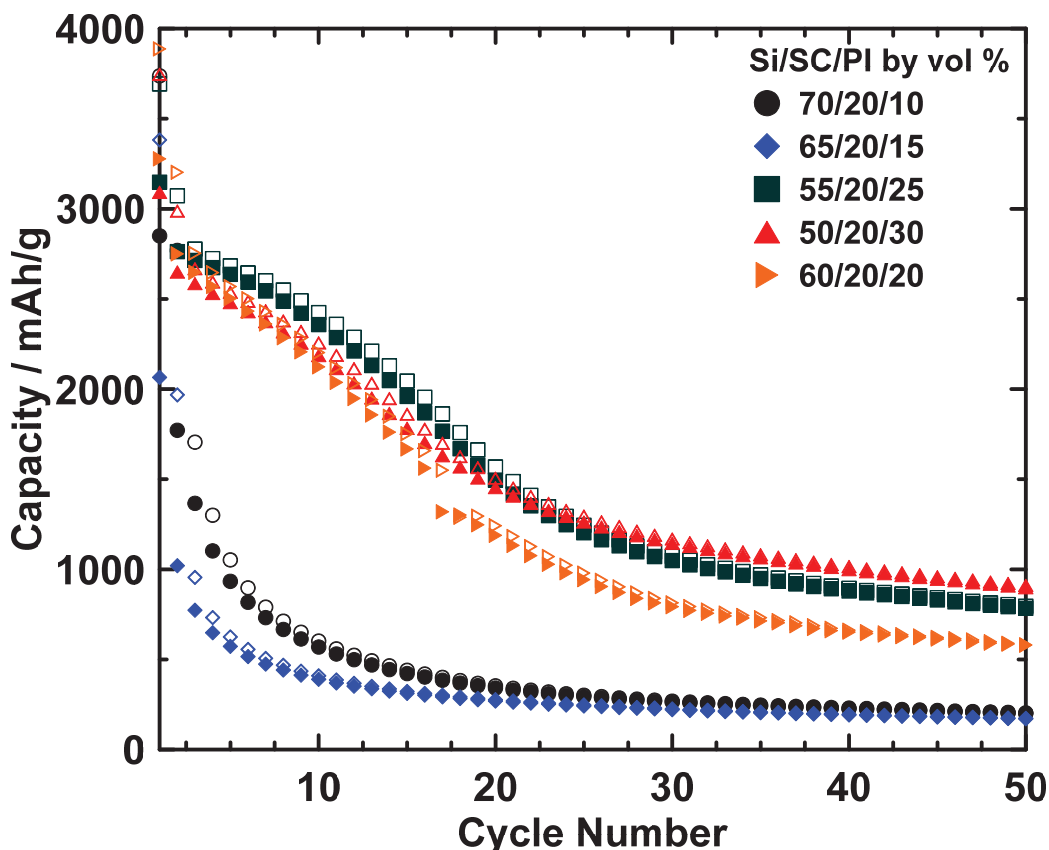
Figure 4.3. Cycling performance of five different Si-based coating formulations using a polyimide binder. Open and closed symbols represent the lithiation and delithiation capacity, respectively.

Using the 55/20/25 formulation, PVDF, and LiPAA containing coatings were also fabricated, as explained in Section 2.5, then electrochemically tested. Figure 4.4 shows the cycling performance and differential capacity plots for each binder. Specifically, Figure 4.4 (a) illustrates the dramatic drop in cyclability between binders that bond with the Si surface and PVDF. Both PI and LiPAA exhibited similar electrochemical performance. The differential capacity plots in (b) through (d) indicated that almost all Si became $Li_{15}Si_4$ during lithiation, and subsequent capacity loss was coupled with a decrease in the $Li_{15}Si_4$ delithiation peak size. The differential capacity plot in Figure 4.4 (d) is uncharacteristic of

Si due to polarization effects. This effect was the result of overly quick cycling due to a significant reduction in capacity during cycling. Future experiments of this sort should utilize a program capable of modifying the C-rate based on the previous cycle capacity.
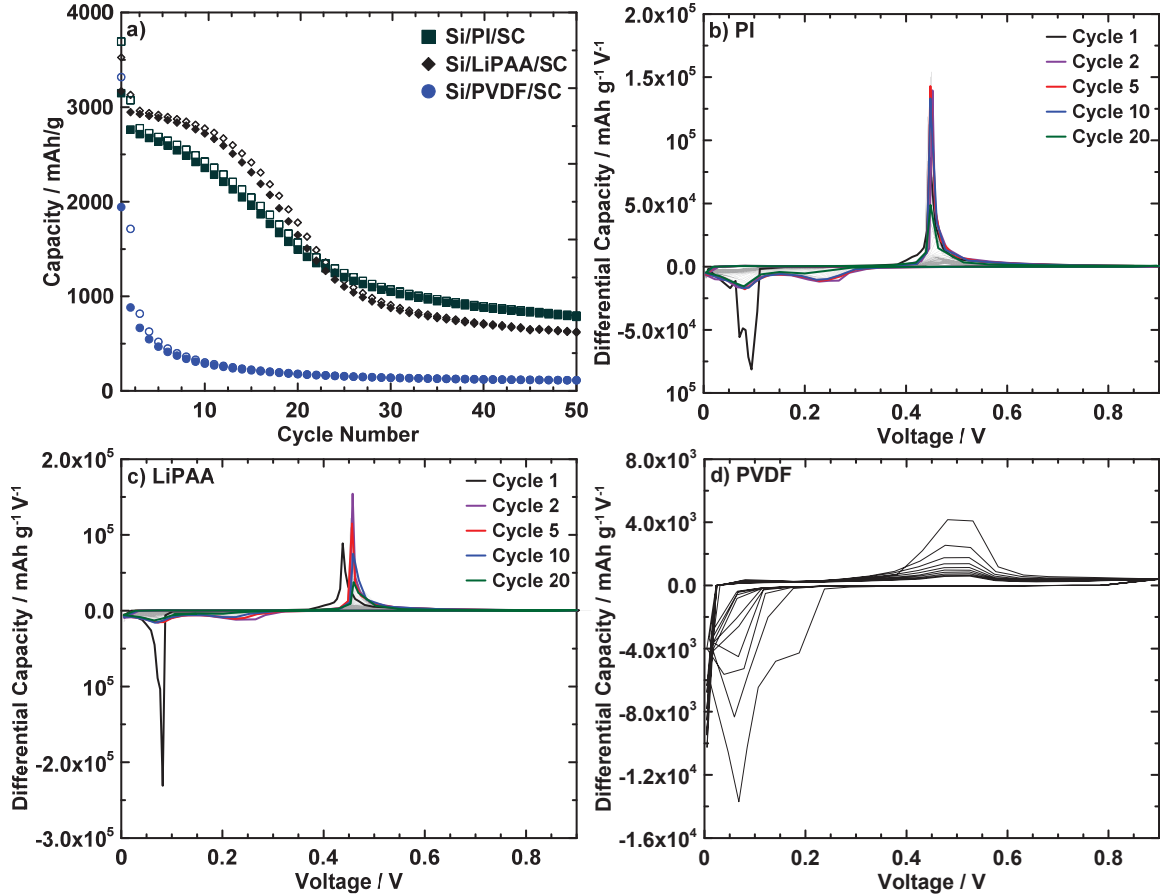
Figure 4.4. Cycling performance in (a) and differential capacity plots of PI, LiPAA, and PVDF containing coatings in a 55/20/25 (Si/SC/Binder) volume ratio in (b), (c), and (d), respectively. Cells were cycled at a C/10 rate with a C/40 trickle on the first cycle, then at a C/4 rate with a C/20 trickle for subsequent cycles.

Overall, all data acquired from bulk (unmilled) Si exhibited constant $Li_{15}Si_4$ formation and capacity fade. When considering the significant capacity fade occurring at all times in these coatings, this formation was certainly expected. Ultimately, this section is valuable as a baseline for the cycling performance of Si containing electrodes.

4.3 Li₁₅Si₄ Formation in *n*-Si Based Coatings

n-Si is an effective material for relating $Li_{15}Si_4$ formation to binder performance since it is known to suppress $Li_{15}Si_4$ when using certain binders and/or C-rates.[55,76,77] Since *n*-Si has a far greater surface area than bulk Si (70-80 m²/g vs. 4.5 m²/g), the amount of binder volume required for an effective coating formulation should differ. In this thesis, a coating formula for *n*-Si based upon a constant binder film thickness (determined from the 55/20/25 bulk-Si/SC/binder volume ratio coating developed in Section 4.2) covering the particles was applied. The equation for determining binder film thickness on the Si and SC particles is:

$$T_B = \frac{\frac{m_B}{\rho_B}}{A_{Si}m_{Si} + A_{SC}m_{SC}} \qquad (4.1)$$

where T_B is the binder film thickness, m_B and ρ_B are the mass and density (ρ_{PI} = 1.43 g/cm³,[73] ρ_{LiPAA} = 1.54 g/cm³ (obtained from 3M), ρ_{PVDF} = 1.77 g/cm³ (from Aldrich)) of the binder used, respectively, A_{Si} and m_{Si} are the surface area and mass of Si, respectively, and A_{SC} (62 m²/g, value from Timcal) and m_{SC} are the surface area and mass of SC carbon black, respectively. Inputting data from a volume ratio of 55/20/25, (Si/SC/binder) the geometric average film thickness, T_B, works out to be ~7.4 nm. Therefore, in order to keep this thickness when switching to *n*-Si, a coating formulation of 27/20/53 by volume must be used.
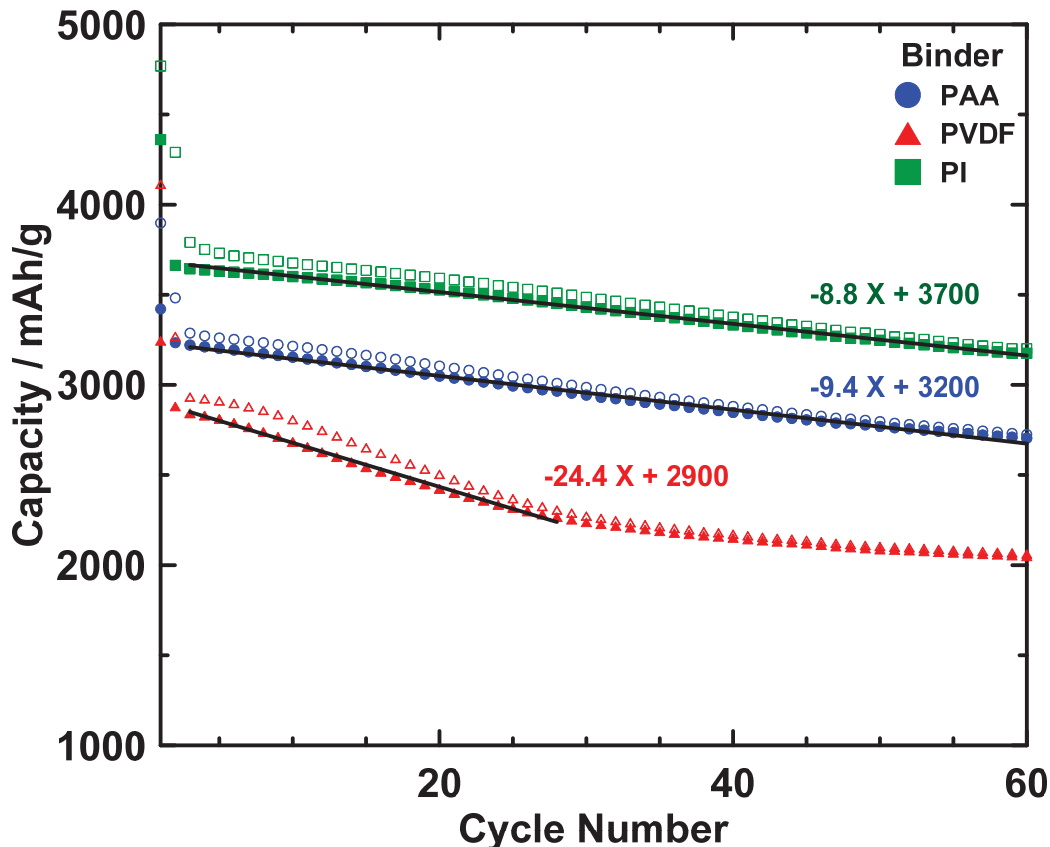
Figure 4.5. Cycling performance of three different electrodes where the formula is 27/20/53 (*n*-Si/SC/Binder) by volume. The plots in blue, red, and green correspond to a PAA, PVDF and PI binder, respectively. Cells were cycled at C/10 rate with a C/40 trickle on the first cycle, then at C/4 rate with a C/20 trickle for subsequent cycles.

The cycling performance of an *n*-Si 27/20/53 (see weight percentages in Table 2.4) coating formulation utilizing various binders is shown in Figure 4.5. There was a steady decrease in capacity in all cases. Similar to Figure 4.3, PAA and PI exhibited similar cycling performance while PVDF initially faded quicker. The delithiation values were linearly fit in each case to further illustrate the difference in fade for each sample. The PAA containing cells appeared to fade slightly quicker than those utilizing PI, as expected from unpublished work from Wilkes et al., [78] but the difference in fade was not significant enough to draw any conclusions. Initial fade seen for the electrode with PVDF, however,

was initially significantly larger than that seen for other binders. This larger fade rate is expected since PVDF does not bond to the surface of Si particles.
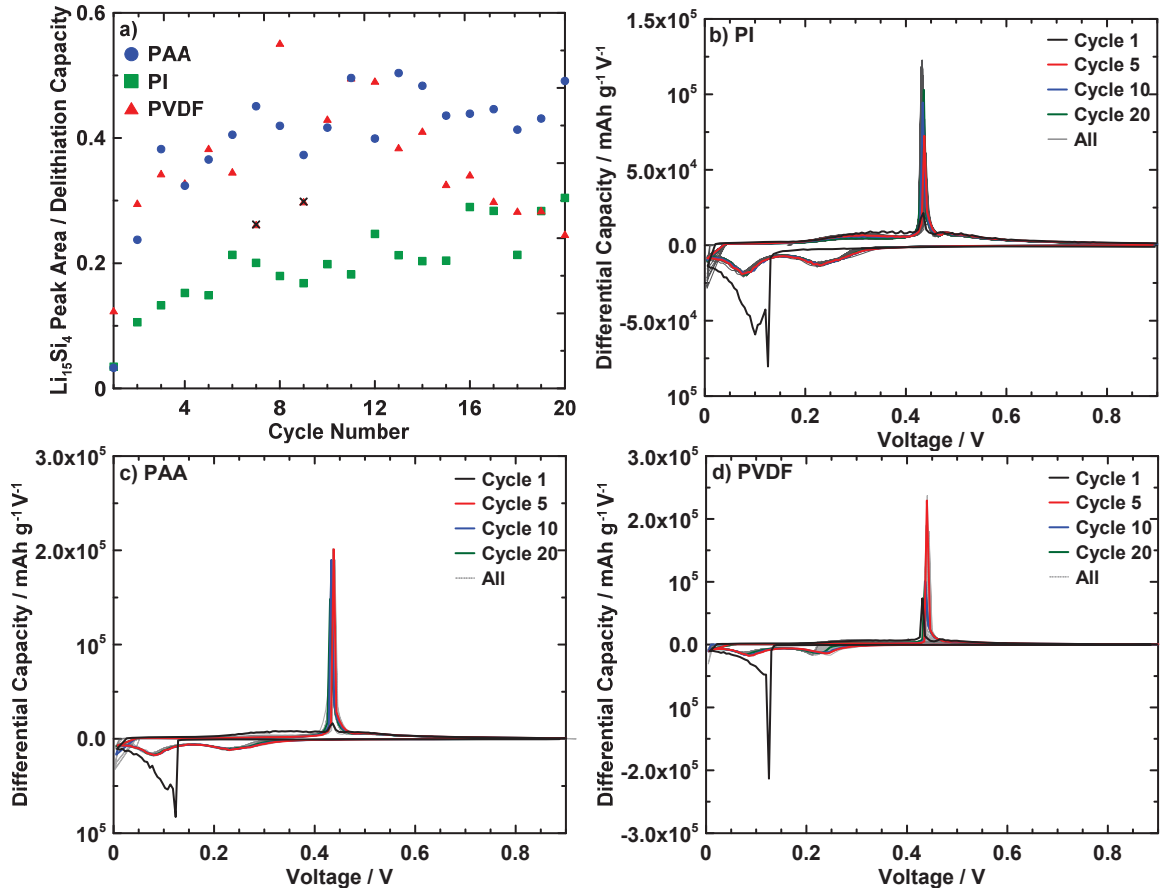

Figure 4.6. $Li_{15}Si_4$ peak area/delithiation capacity in (a) and differential capacity plots of PI, LiPAA, and PVDF containing coatings in a 27/20/53 (*n*-Si/SC/Binder) volume ratio in (b), (c), and (d), respectively. Cells were cycled at C/10 rate with a C/40 trickle on the first cycle, then at C/4 rate with a C/20 trickle for subsequent cycles. $Li_{15}Si_4$ peaks were fit using the method in Section 3.3.1. Two triangles are crossed out in (a) due to power outages during delithiation.

$Li_{15}Si_4$ peak area versus cycle number is shown in Figure 4.6 (a). $Li_{15}Si_4$ formation was most suppressed during cycling for PI binder, followed by PAA and PVDF. PI and PAA suppressed $Li_{15}Si_4$ formation equally during the first cycle. PVDF and PAA exhibited a similar fraction of $Li_{15}Si_4$ formation up until cycle 12. Afterwards, relative $Li_{15}Si_4$ peak area began to decrease for the PVDF binder cell, likely due to loose Si flaking from the electrode, as evidenced by the capacity decrease (shown in Figure 4.5).

61

Lastly, in order to remove any influence of polarization from samples, after the cycling shown in Figure 4.5, cells were subjected to slow rate cycling tests. Specifically, each cell underwent one cycle at C/10, C/20, C/50, and then C/100 rate. Work by Chevrier et al. indicates that when Si in a composite coating is cycled at a slow enough rate, complete $Li_{15}Si_4$ formation will occur at low voltage.[55] Furthermore, work in Chapter 3 (i.e. Figure 3.8) suggests that if Si is under high stress loadings, $Li_{15}Si_4$ should not form regardless of C-rate.
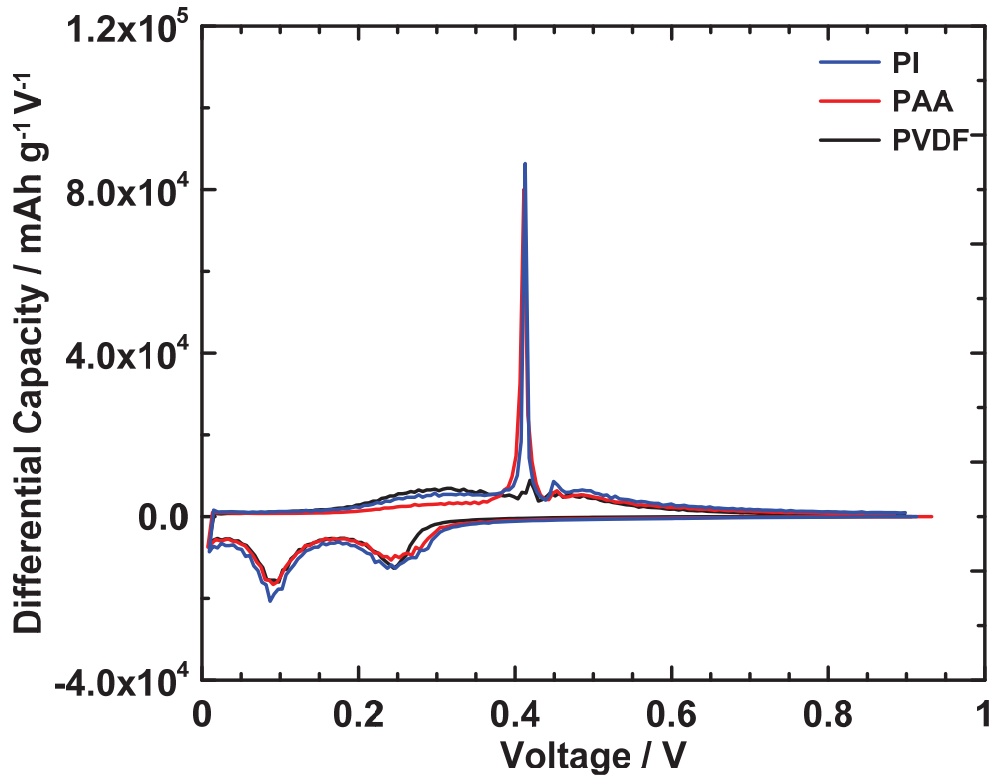
Figure 4.7. Differential capacity curve of the cells in Figure 4.5 cycled at C/100 rate. The PI, PAA, and PVDF containing cells were on cycle 66, 102, and 87, respectively.

Figure 4.7 shows the differential capacity of *n*-Si coatings at C/100 rate with PI, PAA, and PVDF binders. It should be noted that each cell was at a different electrochemical cycle, i.e. PI, PAA, and PVDF containing cells were on cycle 66, 102, and 87, respectively, and that this extensive cycling prior to this slow rate cycle resulted in a large decrease in

$Li_{15}Si_4$ phase formation among cells. This may indicate that larger Si particles have already become disconnected in the coating at this point and that a large portion of the capacity is now coming from very small Si particles that do not form $Li_{15}Si_4$, even under low applied stress. It can be seen from the differential capacity curves that the capacity of the PAA containing coating originated almost entirely from $Li_{15}Si_4$, while the PI coating has capacity that originated from both $Li_{15}Si_4$ and amorphous Li_xSi, as evidenced by the large differential capacity peak area at 0.3 V during delithiation. This difference in $Li_{15}Si_4$ formation could be due to the more extensive cycling experienced in the PAA containing coating. For the PVDF coating, nearly all of the capacity originated from amorphous Li_xSi. Any Si that formed $Li_{15}Si_4$ phase has become disconnected in the PVDF coating. Ultimately, these results show that coatings with PI and PAA binders can maintain electrical contact to Si that forms $Li_{15}Si_4$, while PVDF cannot, which is a significant finding in itself. A more effective investigation for stress effects would involve starting the cells above at the slow rate (e.g. C/100), this way all samples would have similar starting conditions, and no Si that has already become electrically disconnected.

4.4 Conclusions

To summarize, a high performance Si-based composite coating was sought in Section 4.2 using a polyimide binder system. The best formulation was determined to be 55/20/25 by volume Si/SC/binder. To obtain a similar binder film thickness on both the active material and SC carbon black when switching from bulk Si to an *n*-Si based system, a 27/20/53 by volume ratio is required of *n*-Si/SC/binder. $Li_{15}Si_4$ suppression was observed in *n*-Si composite coatings in all systems, but use of a PI binder resulted in the most $Li_{15}Si_4$

63

suppression and least capacity fade, whereas PVDF containing coatings exhibited the most $Li_{15}Si_4$ formation and capacity fade. Upon slow rate testing, PI and PVDF containing coatings exhibited significant $Li_{15}Si_4$ suppression. This is likely the result of very small Si nanoparticles, which suppress $Li_{15}Si_4$ even under low applied stress, making up the majority of the active material. The PAA containing composite coating exhibited extensive $Li_{15}Si_4$ formation, possibly due to its more extensive cycling at the point of the slow rate test. Overall, PI was shown to be able to suppress $Li_{15}Si_4$ formation, in moderate (C/4), and slow (C/100) rate cycling studies. Ultimately, PI and PAA containing coatings were shown to be capable of adhering loosely attached Si, likely due to their capability to form bonds with the Si surface, and maintain capacity resulting from the delithiation of $Li_{15}Si_4$ during cycling.

Chapter 5 Compliant Layers for Si Thin Films

5.1 Compliant Layer: Introduction and Background

Magnetron sputtering, as explained in Section 2.1, is a tool capable of quickly synthesizing wide composition ranges. Combinatorial magnetron sputtering has been used to explore numerous binary Si-M systems (where M is a metal, e.g. M = Cu, Ni, Cr, Fe, Mn, Zn, Sn)[57,67,79,80] and also Si-M_1-M_2 (M_1 and M_2 are two different metals) ternary systems.[81–83] Although magnetron sputtering is not a technique currently used in manufacturing Li-ion electrode materials, it has proved its worth as a high-throughput method for synthesis, and making it possible to test the electrochemical behaviour of many active/inactive or active/active compositions.

In Chapter 3 of this thesis, Si thin films were electrochemically cycled, delaminated, and imaged at different points during cycling. This investigation resulted in the introduction of a Si disconnection model for $Li_{15}Si_4$ formation. Secondly, delamination was linked to an observed shift to higher lithiation, and lower delithiation voltages of Si films during cycling. Previous work by Yang et al. and Sethuraman et al. on the subject of induced stress in Si films during lithiation on a Cu substrate, and on stress-voltage coupling, respectively, showed that observed shifts in the voltage profile of Si films were a result of stress induced by a substrate.[58,60] If stresses induced by a substrate can change the voltage and phase behaviour of thin films, the utility of combinatorial sputtering in modeling alloy systems that will be utilized in a particle-based composite coating is questionable. Considering the utility of combinatorial means to rapidly synthesize and

characterize alloy systems, it would be beneficial if a method could be developed to reduce or eliminate the Si/substrate interaction.

Figure 5.1. Schematic drawing of a lithiated Si thin film (grey) on a Cu substrate (orange) in (a) and on a compliant layer (black) in (b).

This chapter investigates the impact of a compliant layer (CL) between the substrate and Si film on electrochemical behaviour. A schematic of a Si film deposited onto a Cu substrate and onto a compliant layer is presented in Figure 5.1 (a) and (b), respectively. When a Si film is deposited directly onto the substrate (as shown in Figure 5.1(a)), the strong interaction between Si and the substrate results in stress along their interface during charging. To reduce this stress, a layer of a compliant and conducting material was coated onto the substrate prior to sputtering (as shown in Figure 5.1(b)). The compliant layer was made as an uncalendered composite coating, which typically have high surface roughness. During charge, the compliant layer can deform to relieve compressive stress. Furthermore, the rough surface is likely to induce crack formation in the Si thin film where the radius of curvature is high.

In this chapter, the rate of $Li_{15}Si_4$ formation observed for Si films deposited onto compliant layers will be compared to the rates observed in regular Si films, delaminated films in composite coatings, and the optimized n-Si half-cells from Chapter 4. Ultimately, this project aims to combine the versatility and high-throughput capability of magnetron sputtering with an increased accuracy in electrochemical behaviour due to the presence of a stress-eliminating compliant layer.

5.2 Compliant Layer: Experimental Setup

Two types of compliant layers were used in this study. Inactive compliant layers were composed of SC carbon black and binder. The binders PVDF, LiPAA, PI, and FC2179 were used in these coatings. Active compliant layers comprised active material (either graphite or Si alloy) along with binder (either PVDF or LiPAA) and carbon black. As indicated in Table 2.3, some of the active compliant layers were in the form of electrode coatings from commercial battery electrode suppliers (i.e. 3M, Magna, and Moli). The methodology for preparing the inactive and active compliant layer coatings are explained in Section 2.5, and the composition of active and inactive compliant layers are summarized in Table 2.2 and Table 2.3, respectively.

Pre-weighed electrodes, 12 in total, from each compliant layer coating were punched and placed onto an Al covered sputtering table, as shown in Figure 5.2. Additionally, one partially taped Si wafer (for profilometer measurements), six pre-weighed electrolytic Cu discs, and electrolytic Cu foil were attached to the sputtering table using double-sided tape.

Si was sputtered onto inactive compliant layers following procedure #3 from Table 2.1. This procedure was chosen since it was extensively used in Chapter 3. Active compliant layer composite coatings (summarized in Table 2.3) were attached in a similar manner to that shown in Figure 5.2, with a partially taped Si wafer, E-Cu discs, and E-Cu foil. For these coatings, procedure #1 from Table 2.1 was used so that the extra capacity resulting from a thicker coating of Si could be clearly observed. After film deposition, electrodes were incorporated into coin half-cells, as described in Section 2.6. All cells were

cycled at a rate of C/2 with a C/20 trickle at 0.005 mV. Afterwards, $Li_{15}Si_4$ peaks were fit

for the first 20 cycles using the method explained in Section 3.3.1.
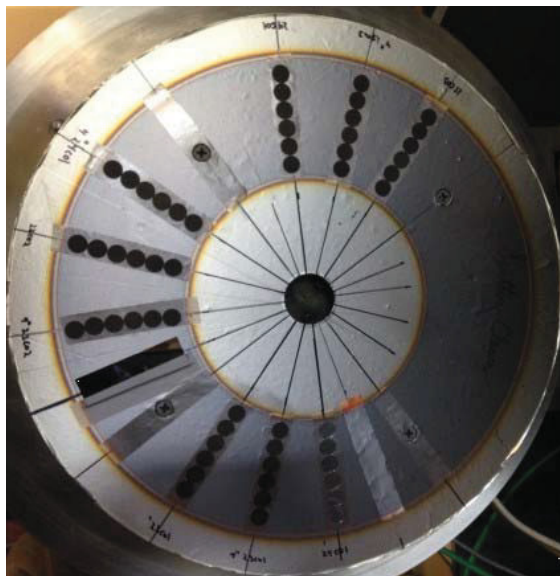
Figure 5.2. Image of the prepared sputtering table used in the inactive compliant layer study after Si sputtering.

5.3 Electrochemical Characterization

5.3.1 Inactive compliant layers for Si thin films

Inactive compliant layers were used to determine if incorporating a compliant layer

could allow sputtered Si to behave more similarly to Si powder in a composite coating.

Multiple binders were tested for inactive compliant layers in order to determine the best

film/compliant layer system, i.e. one with the most similar electrochemical behaviour to *n*-

Si composite coatings. The cycling performance of each compliant layer with Si (Si(CL))

sputtered onto it (according to Table 2.1 pro. #3) is plotted in Figure 5.3. Irreversible and

reversible capacities resulting from the compliant layers were first experimentally

determined (in mAh/g) then subtracted from the observed capacity in graphing Figure 5.3.

These capacities are provided in Table 5.1.

Table 5.1. Characteristics of the inactive compliant layers used in this study. Asterisks (*) indicate that the values were experimentally determined.

Binder	Binder/SC Ratio by mass	Irrev. Cap. / mAh/g*	Rev. Cap. / mAh/g*
PVDF	60/40	210	80
LiPAA	60/40	200	100
FC2179	70/30	320	120
PI	60/40	1800	380
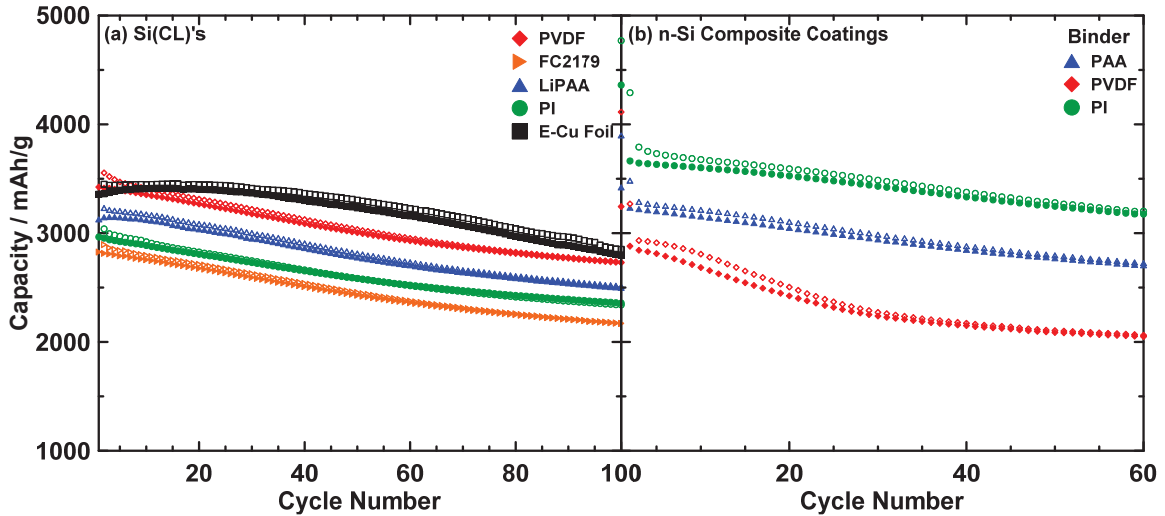
Figure 5.3. Cycling performance of a 275 nm Si film (pro. #3, Table 2.1) sputtered onto different compliant layers and onto E-Cu foil in (a), and of *n*-Si composite coatings using different binders in (b). Open and closed symbols represent the lithiation and delithiation capacity, respectively.

In Figure 5.3 (a), the initial capacities of the various Si(CL)s ranged from under 3000 to over 3500 mAh/g. Although, capacity resulting from the compliant layer was subtracted in producing Figure 5.3 (a), the deposited Si film was thin, therefore error when determining compliant layer mass translated into larger error when predicting theoretical capacities. This was the likely cause behind the observed variation of 500 mAh/g among Si(CL)s. The Si(CL)s experienced a capacity decrease between 600 and 700 mAh/g over 100 electrochemical cycles, which was similar to capacity fade (500 mAh/g over 100 cycles) observed for the same film deposited onto E-Cu. The comparable cycling performance for the Si(CL)s imply that compliant layers are capable of adhering to the dynamic Si film.

In Figure 5.3 (b), it can be seen that the cycling performance of the *n*-Si composite coatings was much more similar to that of the Si(CL)s than the film sputtered onto E-Cu. The *n*-Si composite coatings and Si(CL)s exhibited capacity fade throughout cycling, whereas the film sputtered on E-Cu began to fade near cycle 20. Since fade was shown to be correlated with film detachment in Chapter 3, this result implies that Si(CL)s experience less film/substrate interactions (as evidenced by their constant fade) than films sputtered onto E-Cu.

To understand the electrochemical behaviour of Si sputtered onto compliant layers, $Li_{15}Si_4$ peak area was measured during cycling using the peak fitting method explained in Section 3.3.1. Figure 5.4 shows plots of the $Li_{15}Si_4$ peak area/delithiation capacity and delithiation capacity versus cycle number for the four Si(CL)s that were tested, in (a) through (d). For comparison, the plots in Figure 5.4 (e) and (f) show these results for a 275 nm Si film deposited onto CR-Cu, and *n*-Si composite coatings using different binders. The latter two plots ((e) and (f)) have been previously examined in this thesis. As shown in Chapter 4, and in Figure 5.4 (f), *n*-Si composite coatings formed $Li_{15}Si_4$ on the first cycle, followed by gradual growth in the $Li_{15}Si_4$ phase and capacity fade (shown in Figure 5.3 (b)). The electrochemical behaviour of a Si film sputtered onto CR-Cu, however, was completely different (Figure 5.4 (e)). Capacity fade and $Li_{15}Si_4$ formation did not start until about cycle 15. The fade mechanism in this case is likely governed by the disconnection model (shown in Figure 3.9), whereas in a composite coating, particles are loosely attached to a binder carbon black mixture. Therefore, sputtered Si without a compliant layer is not a good analogue of a composite coating.
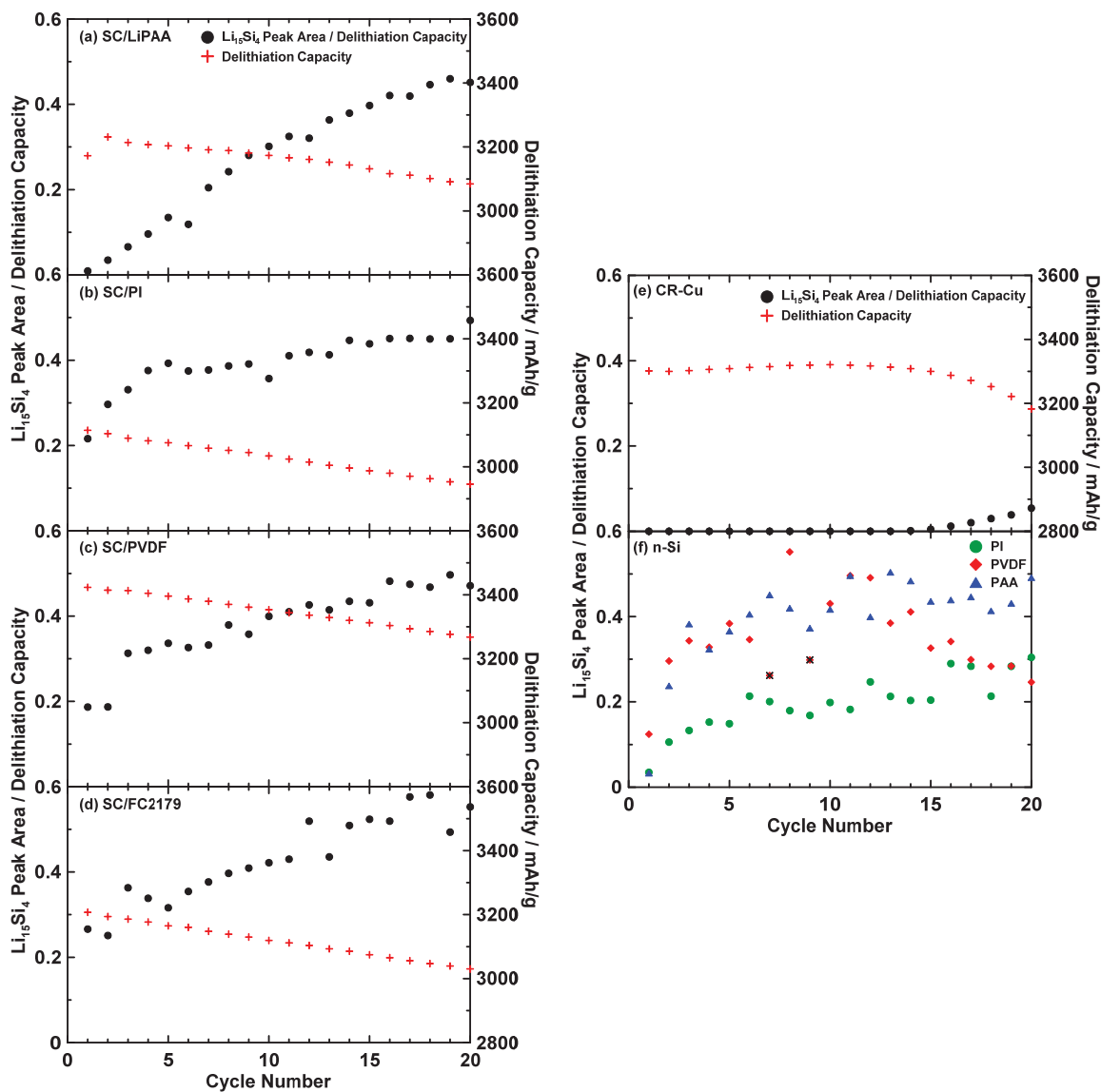
Figure 5.4. Relative $Li_{15}Si_4$ peak area and delithiation capacity versus cycle number for Si films sputtered onto 60/40 by weight SC/binder CL coatings, where the binders in (a), (b), and (c) are LiPAA, PI, and PVDF, respectively. In (d), the CL's composition is 70/30 by weight SC/FC2179. Plots (e), and (f) show these results for a 275 nm film on CR-Cu foil, and *n*-Si composite coatings using PI, PVDF, and PAA binders, respectively.

Unlike films deposited onto a Cu substrate, Si(CL)s exhibited constant capacity fade and $Li_{15}Si_4$ formation from the first cycle and onwards (Figure 5.4 (a) – (d)) similar to that observed in *n*-Si composite coatings. These results mean that Si(CL)s are a much better analogue of Si powder in a composite coating.

5.3.2. Active compliant layers for Si thin films

Active compliant layers were tested to determine if a thin film of Si could increase the capacity of commercial negative electrodes during long term cycling. In Section 5.3.1, substrates described to be inactive compliant layers were used in order to eliminate stresses between the usual metallic current collector and Si thin film, with the hopes of having these films behave more similarly to composite coatings. Seeing the relatively good cycling performance in Figure 5.4, however, prompted the author to fabricate sputtered/composite hybrid electrodes by preparing composite coatings containing an active material like graphite or Si alloy, drying them, then sputtering a film of Si on their surface. The preparation of these coatings is described in Section 2.5. Only coatings obtained from commercial suppliers were calendered before sputtering. The 93.46/0.5/6.04 graphite/SC/PVDF by wt. electrode coating (I, Table 2.3) was prepared by the author, and the other graphite-based coatings (II and III, Table 2.3) were obtained from Magna and Moli Energy, whereas the 91/9 V6 Alloy/LiPAA by wt. coating (IV, Table 2.3) was obtained from 3M. These coatings were then punched into discs, weighed, and positioned along a sputtering table. The sputtering table was prepared similarly to the table shown in Figure 5.4. A thicker Si film (Table 2.1, pro. #1 – about 0.5 mAh/electrode) was sputtered onto these coatings since they have a significant amount of capacity per electrode (>2 mAh). This allowed for the capacity increase resulting from the deposition of a film to be more easily observed.
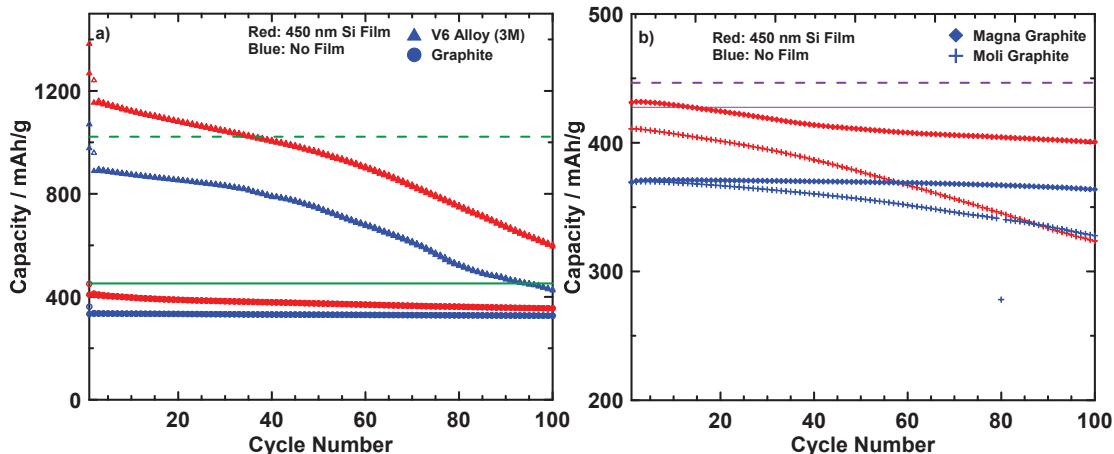
Figure 5.5. Capacity versus cycle number for the coatings listed in Table 2.3 with (in red) and without (in blue) a 400 nm Si thin film sputtered onto them. In (a) a 93.46/0.5/6.04 graphite/SC/PVDF coating fabricated by the author and a 91/9 V6 Alloy/LiPAA coating from 3M are shown, and in (b) cycling performance of commercial graphite coatings from Magna and Moli with and without a 400 nm Si film are shown. The solid and dashed green line in (a) represent the theoretical capacities of the V6 alloy and graphite coating, respectively, with a Si film deposited onto them. The solid and dashed purple line in (b) represent the theoretical capacities of the Moli and Magna graphite coating, respectively, with a Si film deposited onto them. Open and closed symbols represent the lithiation and delithiation capacity, respectively.

In Figure 5.5, the cycling performances for all the coatings in Table 2.3 are plotted with (in red) and without (in blue) a sputtered film of Si. The graphite coating in Figure 5.5 (a) exhibited very little capacity fade without a sputtered film, but with a film deposited, the fade was large enough for the capacity to match that of pure graphite at cycle 100. In the V6 case (Figure 5.5 (a)), capacity fade with and without the Si film was almost identical, indicating that this coating adhered to Si quite well. This is expected since the LiPAA binder used is known to bond to the surface of Si.[84] An unexpected result is that the same amount of film was sputtered onto all the active compliant layers, but in the V6 case, more than double the expected capacity increase was obtained. Reasons for this unprecedented capacity increase could not be determined, but the experiment should be repeated to verify its reproducibility. The graphite-based coating from Moli Energy (in Figure 5.5 (b)) exhibited fade without a Si film and substantial fade with a Si film, whereas the Magna electrodes (in Figure 5.5 (b)) had high capacity retention without a Si film, and

only about 50 mAh/g of capacity fade over 100 cycles with a Si film. Ultimately, these results mean that the Si film disconnects fairly quickly from the graphite coatings, although the slower fade observed with the Magna graphite coating is promising.
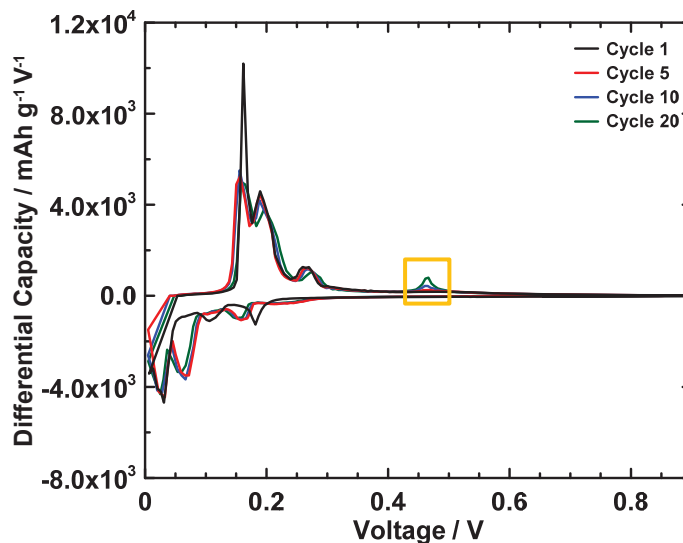
Figure 5.6. Differential capacity curve of Si sputtered (Table 2.1, pro. #1) onto a commercial graphite coating showing cycles 1, 5, 10, and 20. $Li_{15}Si_4$ formation is highlighted using a yellow square.

Figure 5.6 shows the differential capacity versus voltage curve of an electrode consisting of Si sputtered onto a commercial graphite coating (Moli Energy). An incremental increase in $Li_{15}Si_4$ formation is observed during cycling that is quite similar to that seen in Si thin films that are beginning to detach, implying that the coating is not adhering to Si effectively. Since sputtering partially atomizes a target material and deposits it onto a substrate surface, it was anticipated that the atomized Si would thoroughly enter into the porous active coatings. Afterward, these coatings could then be calendered to cover the Si particles in a conductive active coating. Due to the poor cycling performance exhibited in Figure 5.5, however, it was necessary to examine the coatings to determine the penetration depth of Si.

74
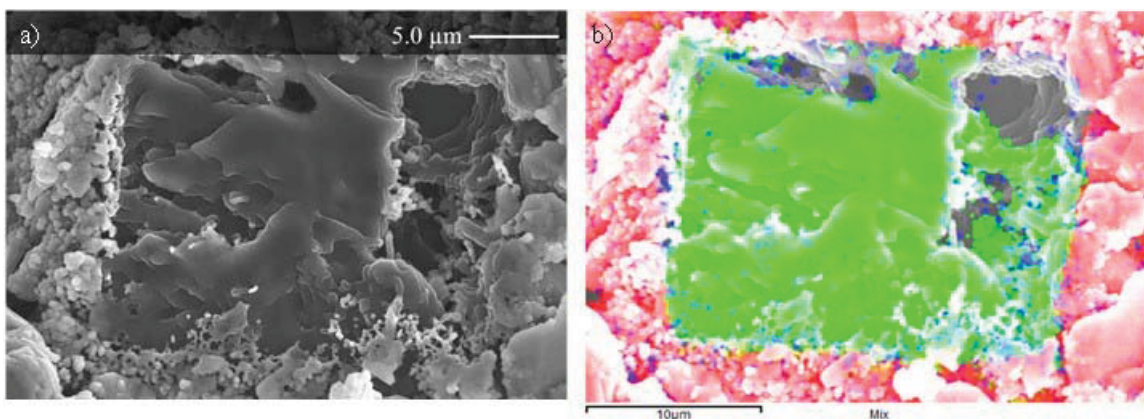
Figure 5.7. An SEM and EDS image at the same location on a 93.46/0.5/6.04 by wt. graphite/SC/PVDF coating (I, Table 2.3) after Si film deposition with a shallow rectangular FIB hole in the center in (a) and (b), respectively. The colors red, green, and blue in image (b) represent Si, C, and Ga, respectively.

FIB ablation was used to create a shallow hole in the uncalendered 93.46/0.5/6.04 by wt. graphite/SC/PVDF coating (I, (Table 2.3)) in order to determine the depth of Si penetration into the material. This coating was originally 100 μm thick, and although the exact hole depth was not known, from tilting the SEM stage during imaging it was determined to be less than 2 μm deep. From Figure 5.7 (b), it can be seen that there was no Si present in the shallow hole. This result means that Si did not penetrate two percent of the coating surface.
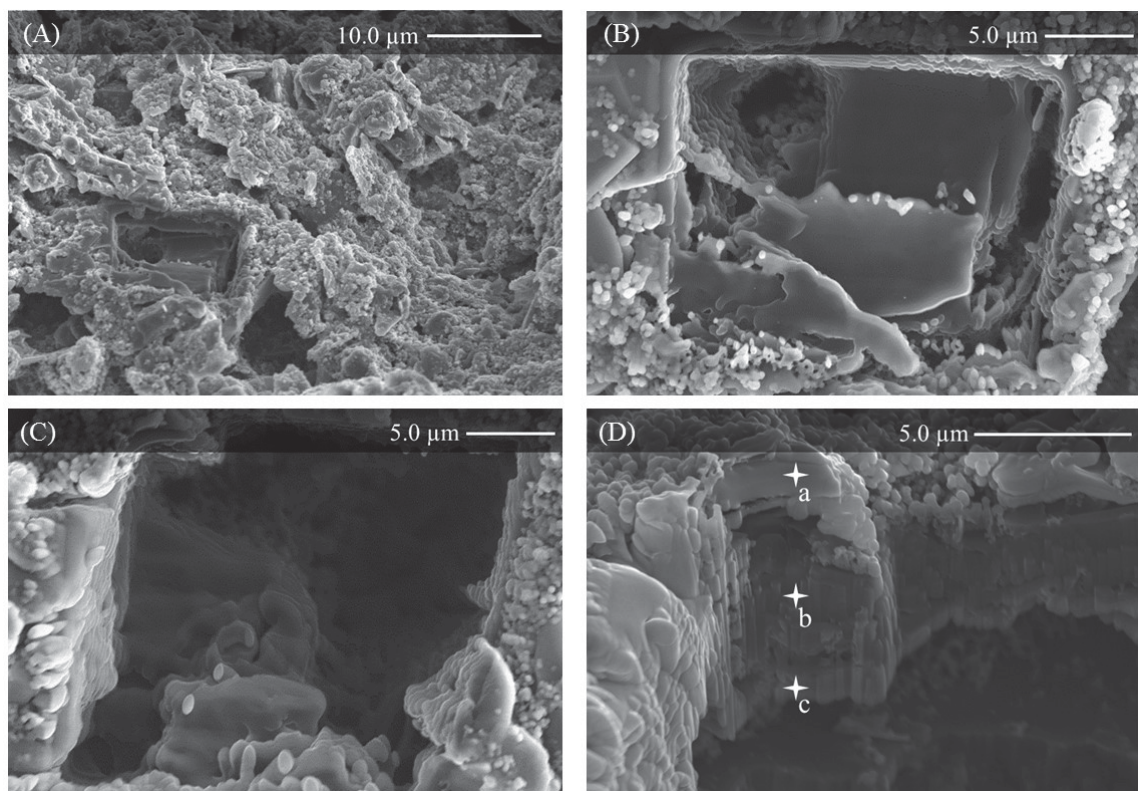
Figure 5.8. SEM images at different angles, positions, and magnifications of the same film-covered coating used in Figure 5.7. Figure 5.8 (A) is a low magnification image of the coating where the sample stage is tilted 45°, in (B) and (C) there are two more FIB cuts ((C) is the deepest) in the coating and the sample stage is not tilted, (D) is a magnified image of the cut in (C) where the sample stage is tilted 45°. Additionally, (a), (b), and (c) in Figure 5.8 IV are points where EDS was used to characterize the point composition.

SEM images shown in Figure 5.8 were used to acquire a deeper understanding of the film/coating morphology. Figure 5.8 (A) is an image taken of the film/coating surface where the sample stage has been tilted 45°. Here the rough, open surface structure can be directly observed. Figure 5.8 (B) and (C) are images of two different cuts into the sample, in (B) there appears to be electrode material beneath the cut, but in the deeper cut, (C), the hole reaches some of the pores inherent in the uncalendered coating. Lastly, Figure 5.8 (D) is a magnified image of the same cut used in (C) where the sample stage is rotated 45°. In this image, the three regions of different brightness were examined using point EDS. The points (a), (b), and (c) were found to be comprised of almost entirely Si, C, and Ga,

respectively, which means that no Si is penetrating the graphite coating interior. Ga was found in the bottom layer since it was the ion used in FIB ablation. Overall, images Figure 5.8 (A), (B), and (C) suggest the coating has a significant amount of porosity; however, Figure 5.8 (D) and Figure 5.7 suggest that no Si enters these pores.

Considering the above results, the capacity fade and $Li_{15}Si_4$ formation in this coating is likely a direct result of the shallow coating penetration of Si, or quite possibly no coating penetration. Overall, since nearly the entire Si film is on the surface of the material, it becomes easily detached and electrically disconnected. Ultimately, magnetron sputter deposition is an ineffective method to fabricate commercial quality film/composite coating hybrid electrodes since the sputtered Si resides entirely on the coating surface. Future work in this area should focus on other insertion methods, e.g. chemical vapour deposition, which may result in improved pore penetration and toward understanding the anomalous capacity increase observed with the V6 coating.

5.3.3 An inactive compliant layer for an Fe-Si thin film

The primary goal for the implementation of inactive compliant layers for Si-based thin films is to eliminate stress between the substrate and film, so that it more resembles particles in a composite coating. Doing so could allow researchers to make better use of the high-throughput sputter-deposition technique to quickly examine unary, binary and ternary films. Therefore, a necessary addition to this chapter is the electrochemical examination of a Si-M composition deposited onto a compliant layer.

The goal of this investigation was to determine if Si-M thin films could behave more like milled specimens when sputtered onto a compliant layer. For this investigation, a $Si_{74}Fe_{26}$ film was sputtered onto both E-Cu foil and a PI/SC (60/40 by weight) compliant

layer (FeSi(CL)). The X-ray diffraction (XRD) patterns of the 300 nm $Fe_{24}Si_{76}$ film and milled $Fe_{25}Si_{75}$ powder (provided by Zhijia Du) is shown in Figure 5.9 (a) and (b), respectively. In this figure, it can be seen that the XRD patterns were significantly different from one another. All peaks were far less pronounced in the film (Figure 5.9 (a)), and background almost entirely takes over the pattern, even though it was taken slowly (0.05° step, 26 second count time). Both patterns, however, were composed of Si and FeSi.
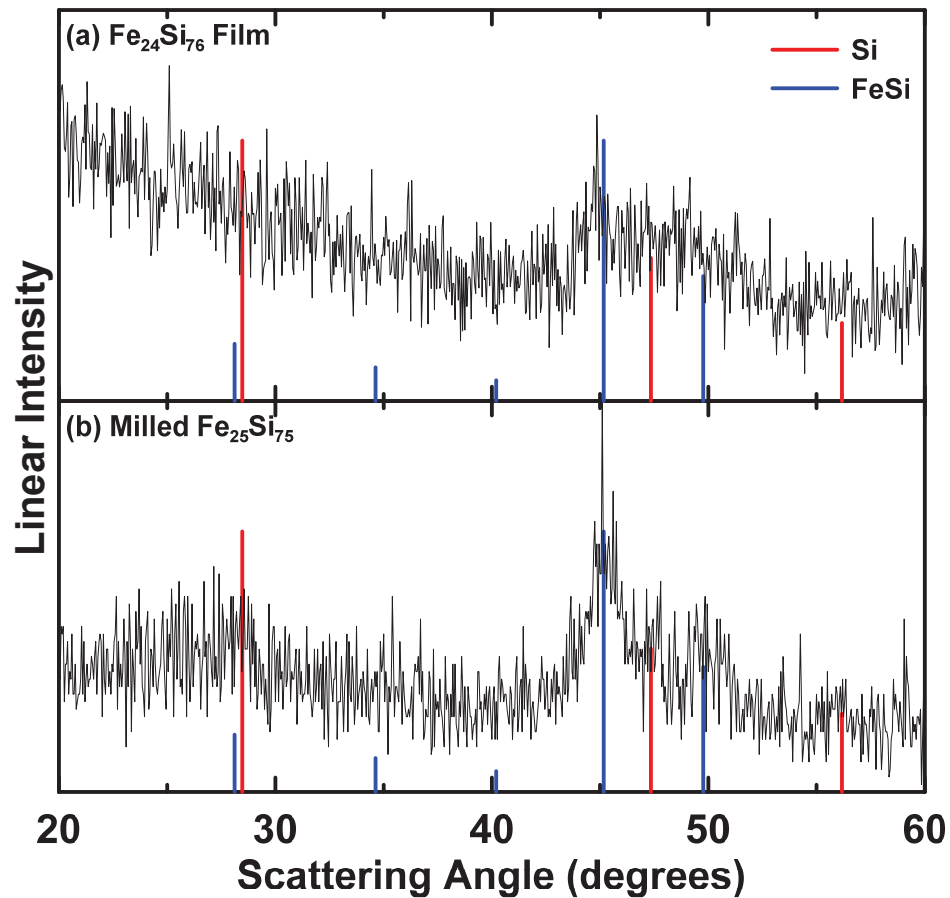
Figure 5.9. X-ray diffraction patterns of the $Fe_{24}Si_{76}$ film (performed by Xiuyun Zhao) on (a) a Si wafer and (b) the milled $Fe_{25}Si_{75}$ powder, prepared and run by Zhijia Du.

The differential capacity curve of cycle 2 for the film on E-Cu, the FeSi(CL), and the milled $Fe_{25}Si_{75}$ in a composite coating is plotted in Figure 5.10. The milled sample clearly obtained less capacity than the electrodes with a sputtered $Fe_{24}Si_{76}$ film. Furthermore, the lithiation profile of the milled sample was quite different from the

FeSi(CL) and film on E-Cu. The higher voltage Si lithiation peak (~0.20 V) was completely absent in this cycle in the milled sample, yet visible in the FeSi(CL) and the film on E-Cu. In the delithiation profiles, no $Li_{15}Si_4$ formation was observed for the FeSi(CL) nor the film on E-Cu, whereas the milled sample seems to have some $Li_{15}Si_4$ formation. Overall, the differential capacity curve of the milled sample was quite different from the prepared films at this point in cycling. This result is likely because of the large difference in microstructure among the samples, as is evident from their very different XRD patterns. In order to estimate how valuable compliant layers could be to sputtering, extended cycling performance, mean lithiation voltage, and mean delithiation voltage is plotted in Figure 5.11.
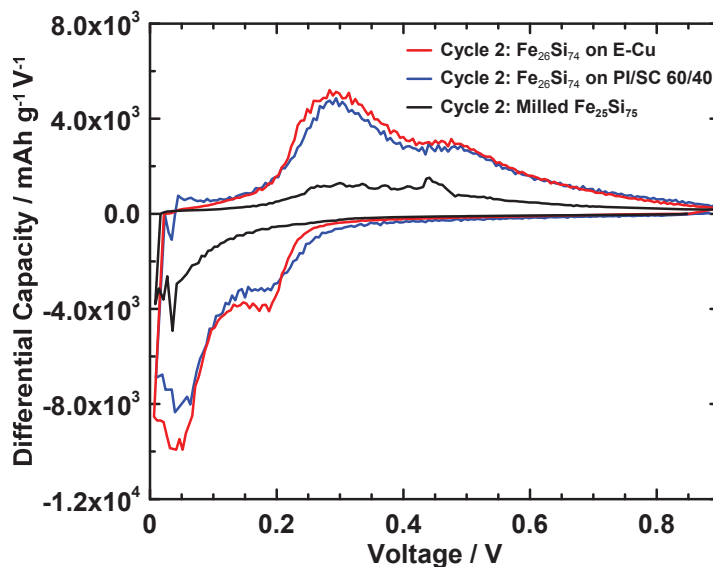
Figure 5.10. Differential capacity versus voltage for an $Fe_{26}Si_{74}$ binary thin film (Table 2.1, pro #4) on Cu foil (in red) and on a PI/SC (60/40 by weight, in blue) compliant layer. Note: differential capacity resulting from the compliant layer was subtracted from the original FeSi(CL) curve.

The cycling performance of the FeSi(CL), Si on E-Cu, and ball-milled $Fe_{25}Si_{75}$ in a composite coating is shown in Figure 5.11 (a). The $Fe_{24}Si_{76}$ films on both a compliant layer and E-Cu exhibited capacities much closer to the theoretical value (56% by wt. Si, 2006 mAh/g), whereas the milled $Fe_{25}Si_{75}$ in a composite coating has a first cycle reversible

79

capacity of about 530 mAh/g. This reduced capacity was likely a result of more inactive FeSi being formed during roller-milling than during sputtering, consuming the active Si. The fade in the FeSi(CL) and film sputtered onto E-Cu was initially high, but after cycle 40 the fade rate of all cells were similar.

The Si sputtered on E-Cu, the FeSi(CL), and the milled $Fe_{25}Si_{75}$ in a composite coating all had significantly different behaviour in their mean delithiation voltage versus cycle number values (as shown in Figure 5.11 (b)). The mean delithiation voltage barely changes during the first 20 cycles, for a Si film sputtered onto E-Cu, then began to increase rapidly, due to the formation of a double peak during delithiation between 0.38 and 0.45 V in the differential capacity curve (as shown in Figure 5.12 (a)). This large change in mean delithiation peak voltage was likely chiefly due to the influence of the substrate, and not from the electrochemistry of the $Fe_{24}Si_{76}$ alloy, as will be explained below. For the FeSi(CL), the mean delithiation voltage slowly decreased during the first 25 cycles and then began to linearly increase due to the formation of a similar double peak in the delithiation differential capacity curve between 0.38 and 0.45 V (as shown in Figure 5.12 (b)). Lastly, for milled $Fe_{25}Si_{75}$ the mean delithiation voltage stayed fairly constant during cycling.
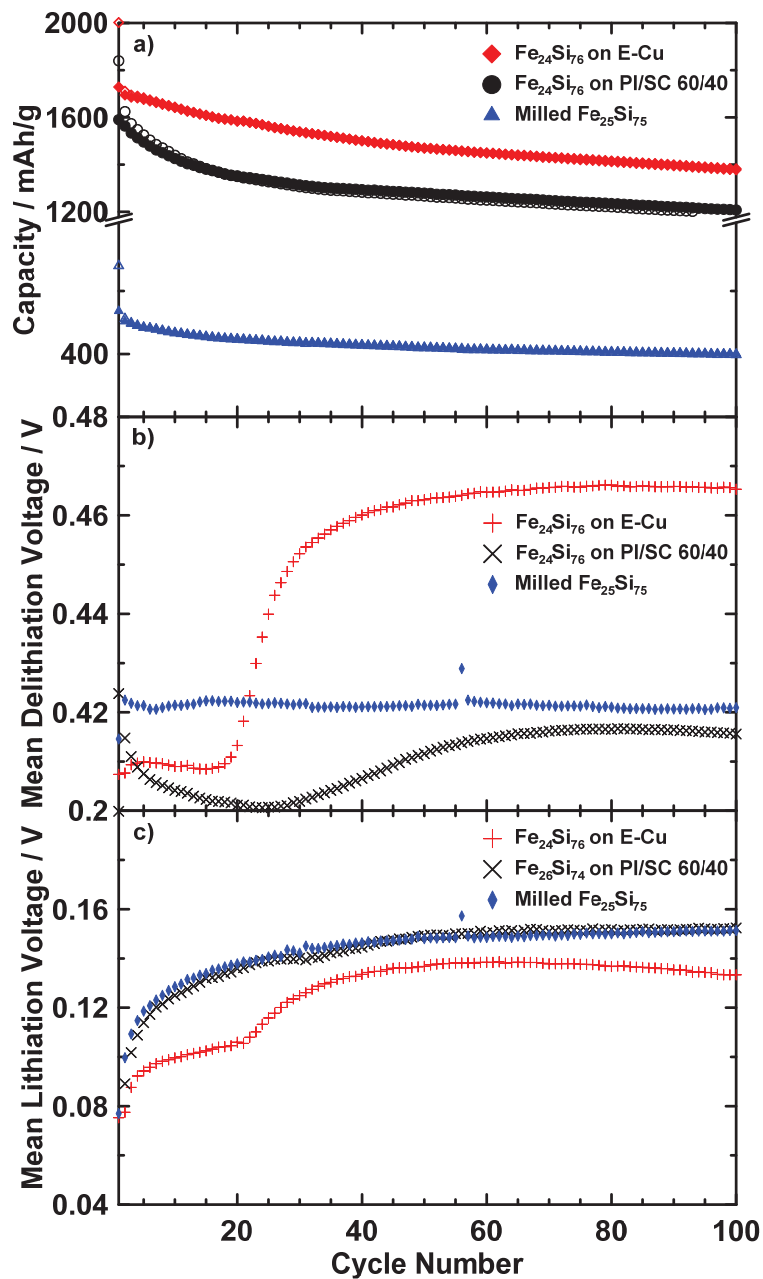
Figure 5.11. Capacity (in (a)), mean delithiation (in (b)), and mean lithiation (in (c)) voltage versus cycle number for the same cells used in Figure 5.10. There is an axis break between 800 and 1200 mAh/g in (a).

The mean lithiation voltages of the three cells, shown in Figure 5.11 (c), were significantly more comparable to one another than their delithiation voltages. Specifically, mean lithiation voltage values for FeSi(CL) were identical to those of the milled sample in a composite coating. In contrast, the mean lithiation voltage of the $Fe_{26}Si_{74}$ film sputtered

onto E-Cu were lower. The two plateaus in the average delithiation voltage for the $Fe_{26}Si_{74}$

film on E-Cu looked very similar to examples of Si detaching from the substrate in Chapter

3. Therefore, this voltage behaviour likely comes from film detachment, not the alloy

electrochemistry. This feature was much less pronounced in the FeSi(CL) film.
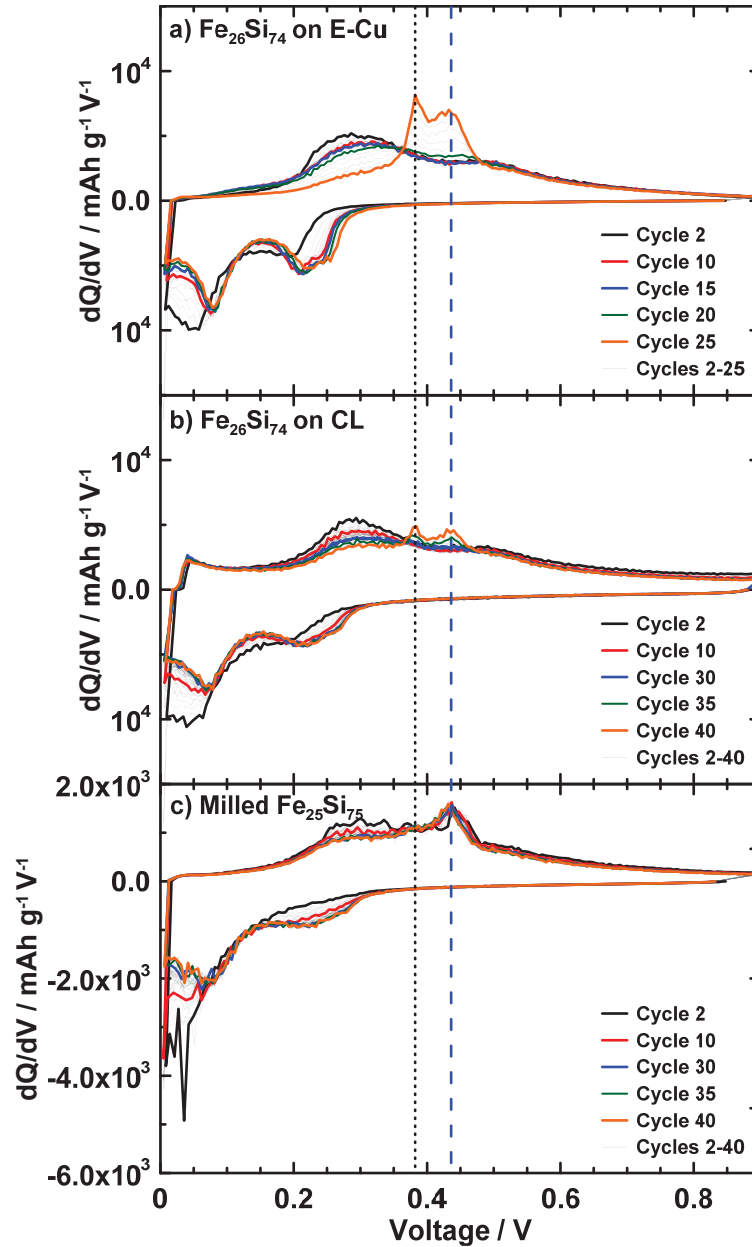
Figure 5.12. Differential capacity versus voltage curve during cycling for $Fe_{24}Si_{76}$ sputtered (Table 2.1, pro #4) onto Cu foil and a compliant layer (PI/SC 60/40 by weight) in (a) and (b), respectively. In c) the differential capacity curve is shown for a roller-milled $Fe_{25}Si_{75}$ sample (work by Zhijia

82

Du, cycling at C/10 with a C/20 trickle). The dotted and dashed lines mark the positions of the emerging 0.38 V and 0.45 V delithiation peaks.

Differential capacity data from a roller-milled sample of the $Fe_{25}Si_{75}$ composite coating, fabricated by Zhijia Du, are graphed in Figure 5.12 (c). Unlike the sputtered Fe-Si alloys that developed peaks at 0.38 V and 0.45 V during cycling, the $Fe_{25}Si_{75}$ composite coating only formed a peak at 0.45 V, consistent with $Li_{15}Si_4$ formation, while a peak at 0.38 V was not observed. Overall, the differential capacity of the FeSi(CL) looked more similar to the ball-milled Si after 40 cycles than the $Fe_{26}Si_{74}$ film on E-Cu. Although the FeSi(CL) film did form a delithiation peak at 0.38 V, it was very small after 40 cycles. In comparison, the $Fe_{26}Si_{74}$ on E-Cu exhibited significantly more $Li_{15}Si_4$ formation and a large peak at 0.38 V was formed after 25 cycles. The origin of the 0.38 V peak is unknown, but it also occurred in ball-milled Si-Fe samples with higher Si content.[85] Ultimately, more compositions sputtered on compliant layers need to be investigated in order to fully understand the value of using a compliant layer.

5.4 Conclusions for the Compliant Layer

To summarize, compliant layers effectively eliminated film/substrate stress and allowed sputtered films to behave more like composite coatings. When Si was sputtered onto inactive compliant layers, $Li_{15}Si_4$ formed during early cycling, unlike those deposited onto a Cu substrate. Additionally, the use of certain CLs resulted in the films having $Li_{15}Si_4$ formation rates during cycling similar to that observed in half-cells made using *n*-Si based composite coatings. Because of the relatively low capacity fade seen in Si(CL)s, Si films were also deposited onto active (Si or graphite-based) coatings, where it was determined

via SEM/FIB/EDS that Si resides entirely on the surface of the electrodes. It is likely that this shallow penetration allows Si to detach easily, resulting in steady capacity fade.

Lastly, a binary $Fe_{26}Si_{74}$ film was sputtered onto both a compliant layer and Cu foil. The electrochemistry, and more specifically the electrochemical cycling performance, of the milled and sputtered films were different because these films have substantially different microstructures. Nevertheless, Fe-Si alloys sputtered onto CLs were found to exhibit electrochemical behaviour more similar to milled Fe-Si samples than to Fe-Si sputtered directly onto Cu foil. Overall, these results suggest that the electrochemical behaviour of sputtered samples becomes more comparable to composite coatings when Si-containing films are sputtered onto a compliant layer. Ultimately, through the use of CLs, the high throughput capability of magnetron sputtering can be combined with more realistic electrochemical measurements, in terms of capacity fade and $Li_{15}Si_4$ formation, when testing Si-based materials.

Chapter 6 Conclusions and Future Work

6.1 Conclusions

$Li_{15}Si_4$ formation in Si thin films was investigated. Si films of varying thicknesses were sputter deposited onto multiple substrates to investigate the implications of and conditions for $Li_{15}Si_4$ formation. It was found that $Li_{15}Si_4$ suppression during cycling of Si thin films was due to stress induced from the presence of the substrate. Furthermore, $Li_{15}Si_4$ formation was found to be coincident with capacity fade and delamination of the Si film from the current collector. Electrochemical cycling studies where $Li_{15}Si_4$ formation was avoided and induced in early cycling confirmed that $Li_{15}Si_4$ formation can have a harmful effect on cycling performance. Overall, these results deepen the understanding of $Li_{15}Si_4$ formation in Si thin films. Moreover, they have profound implications for Si alloys in general, as the presence of $Li_{15}Si_4$ during cycling can be used as a sensitive indicator for weakly bound Si regions.

The performance of Si-based electrode coatings were also studied. Firstly, a high-performing bulk Si-based electrode coating formulation was sought, and then this electrode coating formulation was applied to *n*-Si based coatings. Confirming previous studies,[72,84] the use of binders capable of adhering to the Si surface were shown to exhibit superior cycling performance. PI binder exhibited the most $Li_{15}Si_4$ suppression and least capacity fade. Furthermore, through slow rate studies, PVDF-based coatings were found to lose all capacity resulting from the delithiation of $Li_{15}Si_4$ during cycling, while PI and LiPAA based coatings were found to exhibit $Li_{15}Si_4$ formation after extended cycling. This is

indicative that PI and LiPAA are more capable of adhering to loosely attached Si than PVDF.

The utility of a compliant and conducting layer between the film and substrate also was investigated. Si films were deposited onto active (containing active material) and inactive (not containing active material) compliant layers with the expectation of obtaining electrochemical behaviour similar to Si powder in composite coatings. Si films deposited onto inactive compliant layers exhibited rates of $Li_{15}Si_4$ formation similar to powdered Si in composite coatings, unlike those sputtered directly onto a metallic current collector. Films deposited onto compliant layers also exhibited levels of capacity fade similar to that observed for Si powder in a composite coating. Si films deposited onto active compliant layers exhibited intolerable capacity fade, and SEM/FIB/EDS studies revealed that the film was almost entirely on the surface of the coatings. This was likely the cause behind the observed capacity fade. Lastly, a Si-Fe binary film was deposited onto a PI based inactive compliant layer, and E-Cu foil. Aside from having significantly different capacities, the electrochemical behavior of the film deposited onto a compliant layer was found to be more similar to that of the milled powder in a composite coating compared to that of the film sputtered onto E-Cu.

Overall, $Li_{15}Si_4$ formation was found to be valuable as an indicator for Si under low stress loadings that is effectively poorly connected. This result was proposed and supported (Chapter 3), then directly applied (Chapter 4) to assess electrode quality, then again (Chapter 5) to test the utility of compliant layers. Film/substrate stress was shown to play a significant role in the suppression of $Li_{15}Si_4$. $Li_{15}Si_4$ formation was shown to be harmful to electrochemical cycling performance. The potential of the use of $Li_{15}Si_4$ as a means of

quickly predicting the electrochemical performance of Si containing electrodes was discovered, and $Li_{15}Si_4$ formation in active/inactive alloys can now be related to poorly connected Si that is effectively under a low stress loading. Lastly, compliant layers were shown to allow Si and Si-Fe films to exhibit electrochemical behavior more similar to that of Si powder in a composite coating.

6.2 Future Work

Future work is necessary to understand the specific conditions of $Li_{15}Si_4$ formation in films, as well as composite coatings. Specifically, a rate study should be undertaken using Si films of various thicknesses sputtered onto a substrate. These films could be cycled at rates ranging from 10C to C/100 without a current trickle. Using the resulting data and allowing for extensive cycling performance would be valuable to discern between the effect of polarization and stress on $Li_{15}Si_4$ formation. Additionally, following this procedure, one would be able to determine the threshold C-rate for $Li_{15}Si_4$ formation and relate it to film thickness. Future work in this section could also involve electrochemical testing at various temperatures. Placing this work together, a thermodynamic and electrochemical phase diagram for $Li_{15}Si_4$ formation could be produced, and since $Li_{15}Si_4$ formation has been shown to be detrimental to electrochemical cycling performance, having such a phase diagram could allow future researchers to completely avoid $Li_{15}Si_4$ formation.

$Li_{15}Si_4$ was also found to form when a cell was held at 5 mV for an extended period of time. Therefore, time at low voltage could also influence the degree of $Li_{15}Si_4$ formation. Accordingly, a study in which cells are held at low voltages (ranging from 5 to 50 mV) for

extended periods of time could be undertaken to directly determine the effect of time at low voltage on $Li_{15}Si_4$ formation.

Another project which could be undertaken involves modified cycling procedures using Si thin films. It was evidenced in Chapter 3 that polarization can suppress $Li_{15}Si_4$ formation. Since $Li_{15}Si_4$ formation is harmful to cycling performance, high C-rates during lithiation could be employed to induce polarization and avoid $Li_{15}Si_4$ formation entirely. Afterwards, because $Li_{15}Si_4$ has not been known to form during delithiation, slower C-rates could be used during delithiation. This type of electrochemical cycling procedure could be very advantageous since the majority of cracking and Si disconnection is known to occur during delithiation,[7] therefore it could potentially lower capacity fade. Furthermore, if this idea were incorporated in modern Li-ion batteries (containing Si in the negative electrode), lithiation of the negative electrode is analogous to charging up a Li-ion battery, and fast charging is desirable in commercial rechargeable batteries. Additionally, consumers tend to slowly discharge their batteries, which would also agree with the proposed cycling procedure.

More electrode coating formulations need to be tested for Si containing negative electrodes. In Chapter 4, electrochemical cycling performance was optimized only for bulk Si using PI binder. A more comprehensive and informative study would optimize three different formulations for n-Si containing composite coatings using PVDF, PAA, and PI. After an optimized coating formulation is determined in each case, slow rate cycling studies could be done for early cycling of the n-Si containing composite coatings. Subjecting optimized coatings to slow rates and quantifying $Li_{15}Si_4$ formation during cycling would allow researchers to visualize how well certain binders keep Si under

acceptable stress loadings and well-connected. This investigation would ultimately provide insight into the quality of various binders and coating formulations. Alternatively, since Li-ion batteries do not typically contain negative electrodes that are 20 % by volume, higher volume ratio coatings of active material (e.g. 70/10/20 Si/SC/binder) could be analyzed using $Li_{15}Si_4$ formation during electrochemical cyling as a probe. In this work, the use of more binders (e.g. CMC, FC2179) and binder treatement (i.e. heat treatment) could be used to find an optimal combination that has high capacity retention and minimal $Li_{15}Si_4$ formation.

Since $Li_{15}Si_4$ formation is suppressed under high stress loadings, and since $Li_{15}Si_4$ formation is detrimental to cycling performance and indicative of partial Si detachment, $Li_{15}Si_4$ has the potential to be an early indicator for the quality of Si containing electrode coatings. In order to confirm this conjecture, various coatings incorporating milled Si alloys (e.g. a-Si and FeSi, or a-Si and $NiSi_2$) could be cycled for long periods. Afterwards, the degree of $Li_{15}Si_4$ formation could be compared to the electrochemical cycling performance. If a clear relationship is found between $Li_{15}Si_4$ formation and cycling performance, it would substantiate claims presented in Chapter 3 of this thesis.

Compliant layers were found to allow films to behave more similar to composite coatings; however, no optimal compliant layer formulation for this purpose was found. Therefore, the compliant layer formulation (60/40 SC/binder by wt. largely used in this thesis) should be optimized so that $Li_{15}Si_4$ formation and capacity retention closely matches that observed of optimized n-Si containing composite coatings. This optimization could involve varying the binder identity, mass ratio, coating thickness, heat treatment, and calendering of the compliant layer. A good addition to this work would also be the testing

of compliant layers that do not contain SC carbon black. SC has a high irreversible capacity, making the error in measuring the reversible capacity and coulombic efficiency of Si(CL)s very large. Additionally because SC has a high surface area, electrode coatings using SC in large quantities (e.g. 60 % by weight) tend to be inhomogeneous and spotty. Because of these disadvantages, it may be promising to use a conductive inactive material like TiN instead.

Regarding Si deposited onto active compliant layers, significant variation in the capacity retention was observed. This could potentially be due to the binder identity in the active compliant layer since certain binders (e.g. CMC, and LiPAA) form bonds with the surface of Si.[69] Therefore, active compliant layer coating formulations could be optimized to retain electrical connection to Si. Additionally, anomalously high capacity was observed when Si was sputtered onto a V6 alloy coating from 3M. Future work should first confirm the reproducibility of this phenomenon, then proceed towards understanding the mechanism behind this unexpectedly high capacity. In order to understand this mechanism, a variety of film thicknesses (e.g. 50 to 1000 nm) could be deposited onto the V6 alloy containing electrodes, then cells incorporating these electrodes could be electrochemically characterized. Afterwards, extra capacity (i.e. experimental capacity subtract theoretical capacity) could be plotted against the Si film thickness to determine if there exists a limit for extra capacity as film thickness increases. Furthermore, if the same amount of extra capacity is observed for a 50 nm and 1200 nm Si thin film, the sputtering process could be responsible for the excess capacity. That in itself would be a significant finding.

With an optimized compliant layer, sputtered binary (Si-M where M = Fe, Ni, Cu, B, V, Cr) and ternary Si (Si-M_1-M_2, where M_1 and M_2 are two different transition metals)

systems should be re-examined in search of a coating that suppresses $Li_{15}Si_4$ formation while exhibiting promising capacity retention. This investigation would be a method of rapidly testing numerous Si-M compositions. Futhermore, if an effective Si-M and active compliant layer are determined, a thin layer of Si-M could potentially be deposited onto the active compliant layer to obtain an increased energy density combined with good cycle life.

Overall, more research is necessary to truly understand the conditions for, implications, and utility of $Li_{15}Si_4$ formation during the electrochemical cycling of Si-based negative electrodes. Hopefully, the research presented in this thesis will help guide future researchers toward determining effective Si containing negative electrode formulations for Li-ion batteries.

References

[1]   M.S. Whittingham, F.R. Gamble, The lithiun intercalates of the transition metal dichalcogenides, Materials Research Bulletin 10 (1975) 363–371.

[2]   R.R. Haering, J.A.R. Stiles, K. Brandt, Lithium Molybdenum Disulphide Battery Cathode, U.S. Patent No. 4224390. Washington, DC: Patent and Trademark Office, 1980.

[3]   C. Julien, G.A. Nazri, Solid state batteries: materials design and optimization, Springer Science & Business Media, 2013, 598-600.

[4]   C. Julien, Z. Stoynov, Materials for lithium-ion batteries, Springer Science & Business Media, 2012, 3-5.

[5]   J.W. Fergus, Recent developments in cathode materials for lithium ion batteries, J. Power Sources. 195 (2010) 939–954.

[6]   D. Aurbach, Y. Talyosef, B. Markovsky, E. Markevich, E. Zinigrad, L. Asraf, J.S. Gnanaraj, H. Kim, Design of electrolyte solutions for Li and Li-ion batteries: a review, Electrochim. Acta. 50 (2004) 247–254.

[7]   M.N. Obrovac, V.L. Chevrier, Alloy Negative Electrodes for Li-Ion Batteries, Chem. Rev. 114 (2014) 11444–11502.

[8]   C. Zu, H. Li, Thermodynamic analysis on energy densities of batteries, Energy Environ. Sci. 4 (2011) 2614-2624.

[9]   N. Nitta, F. Wu, J.T. Lee, G. Yushin, Li-ion battery materials: present and future, Mater. Today. 18 (2014) 252–264.

[10]   A.M. Wilson, J.R. Dahn, Lithium Insertion in Carbons Containing Nanodispersed Silicon, J. Electrochem. Soc. 142 (1995) 326–332.

[11]   A. Anani, S. Crouch-Baker, R.A. Huggins, Kinetic and Thermodynamic Parameters of Several Binary Lithium Alloy Negative Electrode Materials at Ambient Temperature, J. Electrochem. Soc. 134 (1987) 3098–3102.

[12]   M.N. Obrovac, L. Christensen, Structural Changes in Silicon Anodes during Lithium Insertion/Extraction, Electrochem. Solid-State Lett. 7 (2004) A93–A96.

[13]   Z. Du, R.A. Dunlap, M.N. Obrovac, High Energy Density Calendered Si Alloy/Graphite Anodes, J. Electrochem. Soc. 161 (2014) A1698–A1705.

[14] D. Linden, T.B. Reddy, Basic Concepts, in: Linden's Handb. Batter., 4th ed., McGraw-Hill Book Companies, New York, 2011: pp. 1.3–1.15.

[15] J.R. Dahn, G.E. Ehrlich, Li Ion Batteries, in: Linden's Handb. Batter., 4th ed., McGraw-Hill Book Companies, New York, 2011: pp. 26.1–26.37.

[16] E. Peled, G. Ardel, Advanced Model for Solid Electrolyte Interphase Electrodes in Liquid and Polymer Electrolytes, J. Electrochem. Soc. 144 (1997) 208–210.

[17] K. Kinoshita, K. Zaghib, Negative Electrodes for Li-Ion Batteries, Berkeley, 2010.

[18] V. Etacheri, R. Marom, R. Elazari, G. Salitra, D. Aurbach, Challenges in the development of advanced Li-ion batteries: a review, Energy Electrochem. Sci. 4 (2011) 3243–3262.

[19] M.N. Obrovac, L. Christensen, D.B. Le, J.R. Dahn, Alloy Design for Lithium-Ion Battery Anodes, J. Electrochem. Soc. 154 (2007) A849–A855.

[20] J.R. Dahn, U. Vonsacken, M.W. Juzkow, H. Al-Janaby, Rechargeable $LiNiO_2$ Carbon Cells, J. Electrochem. Soc. 138 (1991) 2207–2211.

[21] S. Basu, Ambient Temperature Rechargeable Battery, U.S. Patent No. 4423125. Washington, DC: Patent and Trademark Office, 1983.

[22] J.R. Dahn, T. Zheng, Y. Liu, J.S. Xue, Mechanisms for Lithium Insertion in Carbonaceous Materials, Science. 270 (1995) 590–593.

[23] C. Park, S. Yoon, S. Lee, J. Kim, J. Jung, H. Sohn, High-Rate Capability and Enhanced Cyclability of Antimony-Based Composites for Lithium Rechargeable Batteries, J. Electrochem. Soc. 154 (2007) A917–A920.

[24] C. Park, H. Jung, H. Sohn, Electrochemical Behaviors and Reaction Mechanism of Nanosilver with Lithium, Electrochem. Solid-State Lett. 12 (2009) A171–A175.

[25] S. Yoon, C. Park, H. Sohn, Electrochemical Characterizations of Germanium and Carbon-Coated Germanium Composite Anode for Lithium-Ion Batteries, Electrochem. Solid-State Lett. 11 (2008) A42–A45.

[26] M.D. Fleischauer, M.N. Obrovac, J.D. McGraw, R. A. Dunlap, J.M. Topple, J.R. Dahn, Al-M (M=Cr, Fe, Mn, Ni) Thin-Film Negative Electrode Materials, J. Electrochem. Soc. 153 (2006) A484–A491.

[27] H. Kim, B. Park, H.J. Sohn, T. Kang, Electrochemical characteristics of Mg-Ni alloys as anode materials for secondary Li batteries, J. Power Sources. 90 (2000) 59–63.

[28] C.M. Park, Y.U. Kim, H. Kim, H.J. Sohn, Enhancement of the rate capability and cyclability of an Mg-C composite electrode for Li secondary batteries, J. Power Sources. 158 (2006) 1451–1455.

[29] J. Dahn, Short-range Sn ordering and crystal structure of $Li_{4.4}Sn$ prepared by ambient temperature electrochemical methods, Solid State Ionics. 111 (1998) 289–294.

[30] Sony, Sony's New Nexelion Hybrid Lithium Ion Batteries to Have Thirty-Percent More Capacity, (2005). http://www.sony.net/SonyInfo/News/Press/200502/05-006E/ (accessed July 27, 2015)

[31] Amprius Inc., Amprius Raises $30M to Accelerate Commercialization, (2014). http://www.amprius.com/news/news_amprius_20140106.htm (accessed July 03, 2015).

[32] J. Newman, Amprius Begins Shipping a Better Smartphone Battery, (2013). http://techland.time.com/2013/05/23/amprius-begins-shipping-a-better-smartphone-battery/ (accessed July 03, 2015).

[33] Graphite One Resources, Graphite 101, (2012). http://graphiteoneresources.com/investors/graphite_101/ (accessed July 23, 2015).

[34] Metal Prices, Silicon, (2015). http://www.metalprices.com/p/SiliconFreeChart (accessed July 23, 2015).

[35] Metal Prices, Tin, (2015). http://www.metalprices.com/p/TinFreeChart (accessed July 23, 2015).

[36] A. Anani, S. Crouch-Baker, R.A. Huggins, Kinetic and Thermodynamic Paramenters of Several Binary Lithium Alloy Negative Electrode Materials at Ambient Temperature, J. Electrochem. Soc. 134 (1987) 820–821.

[37] J. Li, J.R. Dahn, An In Situ X-Ray Diffraction Study of the Reaction of Li with Crystalline Si, J. Electrochem. Soc. 154 (2007) A156.

[38] J. Li, A. Smith, R.J. Sanderson, T.D. Hatchard, R. A. Dunlap, J.R. Dahn, In Situ [119]Sn Mössbauer Effect Study of the Reaction of Lithium with Si Using a Sn Probe, J. Electrochem. Soc. 156 (2009) A283.

[39] Hauzer Techno Coating, Magnetron Sputtering. http://www.hauzertechnocoating.com/en/plasma-coating-explained/magnetron-sputtering/ (accessed July 24, 2015).

[40] P.J. Kelly, R.D. Arnell, Magnetron sputtering: a review of recent developments and applications, Vacuum. 56 (2000) 159–172.

[41] J.R. Dahn, S. Trussler, T.D. Hatchard, A. Bonakdarpour, K.C. Hewitt, M. Fleischauer, Economical Sputtering System To Produce Large-Size Composition-Spread Libraries Having Linear and Orthogonal Stoichiometry Variations, Chem. Mater. 14 (2002) 3519–3523.

[42] J. Goldstein, Practical scanning electron microscopy: electron and ion microprobe analysis, Springer Science & Business Media, 2012, 64-69.

[43] B. Hafner, Energy Dispersive Spectroscopy on the SEM: A Primer. http://www.charfac.umn.edu/instruments/eds_on_sem_primer.pdf (accessed July 24, 2015).

[44] Institute for Research in Materials, FIB. http://sem-fib.instituteforresearchinmaterials.dal.ca/fib.htm (accessed July 24, 2015).

[45] D.B. Wittry, Electron Probe Microanalyzer, U.S. Patent No. 2916621. Washington, DC: U.S. Patent and Trademark Office 1959.

[46] K. Rhodes, N. Dudney, E. Lara-Curzio, C. Daniel, Understanding the Degradation of Silicon Electrodes for Lithium-Ion Batteries Using Acoustic Emission, J. Electrochem. Soc. 157 (2010) A1354.

[47] X.H. Liu, L. Zhong, S. Huang, S.X. Mao, T. Zhu, J.Y. Huang, Size-Dependent Fracture of Silicon Nanoparticles During Lithiation, ACS Nano. 6 (2012) 1522–1531.

[48] M.T. McDowell, I. Ryu, S.W. Lee, C. Wang, W.D. Nix, Y. Cui, Studying the kinetics of crystalline silicon nanoparticle lithiation with in situ transmission electron microscopy., Adv. Mater. 24 (2012) 6034–41.

[49] L. Cui, R. Ruffo, C.K. Chan, H. Peng, Y. Cui, Crystalline-amorphous core-shell silicon nanowires for high capacity and high current battery electrodes., Nano Lett. 9 (2009) 491–5.

[50] B. Laïk, L. Eude, J.-P. Pereira-Ramos, C.S. Cojocaru, D. Pribat, E. Rouvière, Silicon nanowires as negative electrode for lithium-ion microbatteries, Electrochim. Acta. 53 (2008) 5528–5532.

[51] S.W. Lee, M.T. McDowell, J.W. Choi, Y. Cui, Anomalous Shape Changes of Silicon Nanopillars by Electrochemical Lithiation, Nano Lett. (2011).

[52] M. Green, E. Fielder, B. Scrosati, M. Wachtler, J.S. Moreno, Structured Silicon Anodes for Lithium Battery Applications, Electrochem. Solid-State Lett. 6 (2003) A75.

[53] J.P. Maranchi, A.F. Hepp, A.G. Evans, N.T. Nuhfer, P.N. Kumta, Interfacial Properties of the a-Si/Cu:Active–Inactive Thin-Film Anode System for Lithium-Ion Batteries, J. Electrochem. Soc. 153 (2006) A1246.

[54] J.P. Maranchi, A.F. Hepp, P.N. Kumta, High Capacity, Reversible Silicon Thin-Film Anodes for Lithium-Ion Batteries, Electrochem. Solid-State Lett. 6 (2003) A198.

[55] V.L. Chevrier, L. Liu, D.B. Le, J. Lund, B. Molla, K. Reimer, et al., Evaluating Si-Based Materials for Li-Ion Batteries in Commercially Relevant Negative Electrodes, J. Electrochem. Soc. 161 (2014) A783–A791.

[56] I. Ryu, J.W. Choi, Y. Cui, W.D. Nix, Size-dependent fracture of Si nanowire battery anodes, J. Mech. Phys. Solids. 59 (2011) 1717–1730.

[57] T.D. Hatchard, J.R. Dahn, Study of the Electrochemical Performance of Sputtered $Si_{1-x}Sn_x$ Films, J. Electrochem. Soc. 151 (2004) A1628.

[58] V.A. Sethuraman, V. Srinivasan, A.F. Bower, P.R. Guduru, In Situ Measurements of Stress-Potential Coupling in Lithiated Silicon, J. Electrochem. Soc. 157 (2010) A1253.

[59] V.A. Sethuraman, M.J. Chon, M. Shimshak, V. Srinivasan, P.R. Guduru, In situ measurements of stress evolution in silicon thin films during electrochemical lithiation and delithiation, J. Power Sources. 195 (2010) 5062–5066.

[60] B. Yang, Y.-P. He, J. Irsa, C. a. Lundgren, J.B. Ratchford, Y.-P. Zhao, Effects of composition-dependent modulus, finite concentration and boundary constraint on Li-ion diffusion and stresses in a bilayer Cu-coated Si nano-anode, J. Power Sources. 204 (2012) 168–176.

[61] L.Y. Beaulieu, T.D. Hatchard, a. Bonakdarpour, M.D. Fleischauer, J.R. Dahn, Reaction of Li with Alloy Thin Films Studied by In Situ AFM, J. Electrochem. Soc. 150 (2003) A1457.

[62] Y. Luo, Comprehensive handbook of chemical bond energies, CRC Press, 2007.

[63] K. Kholostov, L. Serenelli, M. Izzi, M. Tucci, M. Balucani, Electroplated contacts and porous silicon for silicon based solar cells applications, Mater. Sci. Eng. B. 194 (2015) 78–85.

[64] J. Kanungo, C. Pramanik, S. Bandopadhyay, U. Gangopadhyay, L. Das, H. Saha, et al., Improved contacts on a porous silicon layer by electroless nickel plating and copper thickening, Semicond. Sci. Technol. 21 (2006) 964–970.

[65] L.Y. Beaulieu, K.W. Eberman, R.L. Turner, L.J. Krause, J.R. Dahn, Colossal Reversible Volume Changes in Lithium Alloys, Electrochem. Solid-State Lett. 4 (2001) A137.

[66] I.A. Courtney, R.A. Dunlap, J.R. Dahn, In-situ [119]Sn Mössbauer effect studies of the reaction of lithium with SnO and SnO:0.25 B_2O_3:0.25 P_2O_5 glass, Electrochim. Acta. 45 (1999) 51–58.

[67] Z. Du, T.D. Hatchard, R.A. Dunlap, M.N. Obrovac, Combinatorial Investigations of Ni-Si Negative Electrode Materials for Li-Ion Batteries, J. Electrochem. Soc. 162 (2015) A1858–A1863.

[68] J. Li, L. Christensen, M.N. Obrovac, K.C. Hewitt, J.R. Dahn, Effect of Heat Treatment on Si Electrodes Using Polyvinylidene Fluoride Binder, J. Electrochem. Soc. 155 (2008) A234.

[69] S. Komaba, K. Shimomura, N. Yabuuchi, T. Ozeki, H. Yui, K. Konno, Study on polymer binders for high-capacity SiO negative electrode of Li-Ion batteries, J. Phys. Chem. C. 115 (2011) 13487–13495.

[70] N.S. Hochgatterer, M.R. Schweiger, S. Koller, P.R. Raimann, T. Wöhrle, C. Wurm, M. Winter, Silicon/Graphite Composite Electrodes for High-Capacity Anodes: Influence of Binder Chemistry on Cycling Stability, Electrochem. Solid-State Lett. 11 (2008) A76.

[71] M. Wachtler, M.R. Wagner, M. Schmied, M. Winter, The effect of the binder morphology on the cycling stability of Li – alloy composite electrodes, J. Electroanal. Chem. 510 (2001) 12–19.

[72] J. Li, D.B. Le, P.P. Ferguson, J.R. Dahn, Lithium polyacrylate as a binder for tin-cobalt-carbon negative electrodes in lithium-ion batteries, Electrochim. Acta. 55 (2010) 2991–2995.

[73] Dupont Chemicals. http://www.dupont.com/content/dam/assets/products-and-services/membranes-films/assets/DEC-Kapton-summary-of-properties.pdf (accessed July 27, 2015)

[74] J. Yang, C. Gong, F. Shi, X. Xie, High Strength of Physical Hydrogels Based on Poly(acrylic acid) poly(ethylene glycol) Methyl Ether: Role of Chain Architecture on Hydrogel Properties, J. Phys. Chem. 116 (2012) 12038–12047.

[75] The Engineering ToolBox. http://www.engineeringtoolbox.com/physical-properties-thermoplastics-d_808.html (accessed July 24, 2015).

[76] F. Wang, L. Wu, B. Key, X.Q. Yang, C.P. Grey, Electrochemical Reaction of Lithium with Nanostructured Silicon Anodes: A Study by In-Situ Synchotron X-

Ray Diffraction and Electron Energy-Loss Spectroscopy, Adv. Mater. 3 (2013) 1324–1331.

[77]   C. Erk, T. Brezesinski, H. Sommer, R. Schneider, Toward Silicon Anodes for Next-Generation Lithium Ion Batteries: A Comparative Performance Study of Various Polymer Binders and Silicon Nanopowders, ACS Appl. Mater. Interfaces. 5 (2013) 7299–7307.

[78]   B. Wilkes, Z. Brown, M.N. Obrovac, Unpublished Work (2015).

[79]   M.D. Fleischauer, J.M. Topple, J.R. Dahn, Combinatorial Investigations of Si-M (M = Cr + Ni, Fe, Mn) Thin Film Negative Electrode Materials, Electrochem. Solid-State Lett. 8 (2005) A137.

[80]   L.Y. Beaulieu, K.C. Hewitt, R.L. Turner, A. Bonakdarpour, A.A. Abdo, L. Christensen, et al., The Electrochemical Reaction of Li with Amorphous Si-Sn Alloys, J. Electrochem. Soc. 150 (2003) A149.

[81]   M.D. Fleischauer, J.R. Dahn, Combinatorial Investigations of the Si-Al-Mn System for Li-Ion Battery Applications, J. Electrochem. Soc. 151 (2004) A1216.

[82]   L. MacEachern, R.A. Dunlap, M.N. Obrovac, A Combinatorial Investigation of Fe-Si-Zn Thin Film Negative Electrodes for Li-Ion Batteries, J. Electrochem. Soc. 162 (2014) A229–A234.

[83]   T.D. Hatchard, J.R. Dahn, S. Trussler, M. Fleischauer, A. Bonakdarpour, J.R. Mueller-Neuhaus, et al., The amorphous range in sputtered Si–Al–Sn films, Thin Solid Films. 443 (2003) 144–150.

[84]   S. Komaba, N. Yabuuchi, T. Ozeki, Z. Han, K. Shimomura, H. Yui, et al., Comparative Study of Sodium Polyacrylate and Poly-(vinylidene fluoride) as Binders for High Capacity Si-Graphite Composite Negative Electrodes in Li-Ion Batteries, J. Phys. Chem. 116 (2011) 1380–1389.

[85]   Z. Du, R.A. Dunlap, M.N. Obrovac, Unpublished Work (2015).

Appendix

Request for Permission to Reproduce or Re-Publish ECS Material

Please fax this form to: The Electrochemical Society (ECS), Attn: Permissions Requests, 1.609.730.0629. You may also e-mail your request to: copyright@electrochem.org. Include all the information as required on this form. Please allow 3-7 days for your request to be processed.

I am preparing a (choose one): ☐ paper ☐ chapter ☐ book ☒ thesis

entitled: Li15Si4 Formation in Si-based Negative Electrodes for Li-ion Batteries

to be published by: Douglas Iaboni

in an upcoming publication entitled: No publication associated.

I request permission to use the following material in the publication noted above, and request nonexclusive rights for all subsequent editions and in all foreign language translations for distribution throughout the world.

Description of material to be used—Indicate what material you wish to use (figures, tables, text, etc.) and give the full bibliographic reference for the source publication. You may attach a separate list, organized by ECS title.

✓ Figure 9 from "A.M. Wilson, J.R. Dahn, Lithium Insertion in Carbons Containing Nanodispersed Silicon, J. Electrochem. Soc. 142 (1995) 326–332."

✓ Figure 8 from "J. Li, J.R. Dahn, An In Situ X-Ray Diffraction Study of the Reaction of Li with Crystalline Si, J. Electrochem. Soc. 154 (2007) A156."

✓ Figure 3 from "J. Li, A. Smith, R.J. Sanderson, T.D. Hatchard, R. A. Dunlap, J.R. Dahn, In Situ 119Sn Mössbauer Effect Study of the Reaction of Lithium with Si Using a Sn Probe, J. Electrochem. Soc. 156 (2009) A283."

Signature: **Douglas Iaboni** Digitally signed by Douglas Iaboni DN: cn=Douglas Iaboni, o=Dalhousie University, ou=Chemistry, email=Douglas.Iaboni@dal.ca, c=CA Date: 2015.08.17 13:22:22 -03'00' Date: August 17th 2015

Name: Douglas Iaboni

Address: 6299 South Street

Halifax, NS

B3H 4R2

Telephone: (902) 494-2211 Fax: (902) 895-5529

E-mail: Douglas.Iaboni@dal.ca

Permission is granted to reproduce the above-referenced material. Please acknowledge the author(s) and publication data of the original material, and include the words: "Reproduced by permission of The Electrochemical Society."

Aug. 18, 2015
Date

Blanked

Ann F. Goedkoop, Publications Production Director

Request for Permission to Reproduce or Re-Publish ECS Material

Please fax this form to: The Electrochemical Society (ECS), Attn: Permissions Requests, 1.609.730.0629. You may also e-mail your request to: copyright@electrochem.org. Include all the information as required on this form. Please allow 3-7 days for your request to be processed.

I am preparing a (choose one): ☐ paper ☐ chapter ☐ book ☒ thesis

entitled: Li15Si4 Formation in Si-based Negative Electrodes for Li-ion Batteries

to be published by: Douglas Iaboni

in an upcoming publication entitled: No publication associated.

I request permission to use the following material in the publication noted above, and request nonexclusive rights for all subsequent editions and in all foreign language translations for distribution throughout the world.

Description of material to be used—Indicate what material you wish to use (figures, tables, text, etc.) and give the full bibliographic reference for the source publication. You may attach a separate list, organized by ECS title.

Figure 4 from "V.A. Sethuraman, V. Srinivasan, A.F. Bower, P.R. Guduru, In Situ Measurements of Stress-Potential Coupling in Lithiated Silicon, J. Electrochem. Soc. 157 (2010) A1253."

Signature: Douglas Iaboni
Digitally signed by Douglas Iaboni
DN: cn=Douglas Iaboni, o=Dalhousie University,
ou=Chemistry, email=Douglas.Iaboni@dal.ca, c=CA
Date: 2015.08.17 13:22:22 -03'00'
Date: August 18th 2015

Name: Douglas Iaboni

Address: 6299 South Street

Halifax, NS

B3H 4R2

Telephone: (902) 494-2211   Fax: (902) 895-5529

E-mail: Douglas.Iaboni@dal.ca

Permission is granted to reproduce the above-referenced material. Please acknowledge the author(s) and publication data of the original material, and include the words: "Reproduced by permission of The Electrochemical Society."

Aug. 18, 2015
Date

Blanked

Ann F. Goedkoop, Publications Production Director

Permissions from ACS and Elsevier have been acquired, but are not required from either journal in a thesis or dissertation (as can be found online).

100